Spatial Nonlocality and Its Effects on the Scattering Characteristics of Wave-Bearing Media

by

Nathan Geib

A dissertation submitted in partial fulfillment
of the requirements for the degree of
Doctor of Philosophy
(Mechanical Engineering)
in The University of Michigan
2022

Doctoral Committee:

Professor Karl Grosh, Co-Chair
Assistant Professor Bogdan-Ioan Popa, Co-Chair
Professor Dennis Bernstein
Associate Professor Xiaoming Mao

Nathan Geib

geib@umich.edu

ORCID iD: 0000-0003-3360-775X

For Jeremy

ACKNOWLEDGEMENTS

I would like to sincerely thank my advisor, Dr. Karl Grosh, and my co-advisor, Dr. Bogdan Popa. Karl, thank you for taking a chance on me and graciously offering me a position in your research group. Your excitement and passion for this work were contagious and the wisdom you've imparted has been invaluable. Bogdan, I could not have completed this work without your deep understanding of this field of research. Witnessing your journey as a new professor, and following your lead in service to the profession opened doors for me I could not have opened myself. I would also like to thank my committee members, Dr. Dennis Bernstein and Dr. Xiaoming Mao, for their support in this work. Thank you both for taking the time to serve on my committee and for your thoughtful contributions to my research.

I would like to acknowledge my colleagues in the Grosh Research Group, especially Dr. Alison Hake and Dr. Aritra Sasmal, for their support and friendship. Alison, you always understood my struggles and helped me celebrate my successes. Ari, your mathematical prowess and quick wit made working with you a true joy. Thank you both for all of your help. I also want to thank my colleagues in the Popa Research Group, Dr. YeonJoon Cheong, Hyung-Suk Kwon, and Yuxin Zhai. Your kindness and friendship made coming into the office always a pleasure.

I want to thank my father, Dan, step-mother, Deb, mother, Margaret, and brother, Jeremy, for their endless love and support throughout my time in graduate school. Dad, Deb, you've helped and supported me in more ways than I could ever express in words, and I truly could not have done this without you. Mom, our weekly phone calls were something

I always looked forward to. You understand me like no one else can. Jeremy, you're the strongest person I know. You've shown me what it means to never give up, and I'm proud to call you my brother.

Finally, I want to thank the friends that became family in Ann Arbor, Tim Wilkins, Peter Lussier, Trey Helwig, James Kelly, and Meghan Cleary. Tim, our road trips south were always exactly what I needed in the coldest winter months. Pete, you reignited my passion for teaching and love of nature. Trey, your one-of-a-kind sense of humor never failed to lighten my mood. James and Meg, you've both seen me through so much in the years we've known each other. I would have been lost without you and I am forever grateful for your love and support.

TABLE OF CONTENTS

LIST OF FIGURES

Figure

LIST OF TABLES

Table

ABSTRACT

Reciprocity is the principle in the study of wave propagation that states that given a source and a receiver in a linear domain, switching their locations will not affect the received signal. Systems that break reciprocity have received substantial attention over the last few decades for their potential applications in noise and vibration control, cloaking, and diagnostic imaging. Presented here is an investigation of how action at a distance affects the scattering characteristics of wave-bearing systems. We focus in particular on how such a nonlocal coupling, imposed by transmitting a disturbance sensed by a probe at one location through a controller to an actuator at a separate location, can be used to strongly break reciprocity in linear acoustic and elastodynamic systems. Because their separation distances are subwavelength, each probe-actuator pair can be treated as a single unit cell of a larger metamaterial. First, we present results of a single unit cell in an acoustic waveguide, highlighting its remarkable ability to break reciprocity over large frequency ranges, and explain how the behavior can be tuned by adjusting only its controlling electronics. We discuss the mechanisms by which reciprocity is broken and the conditions required for the system to be stable. We show how conclusions regarding the characteristics of an ideal plane wave acoustic model of our system must be adapted when accounting for the controlling electronics and loudspeaker dynamics used in experimental testing. Next, we discuss how the open loop feedforward control strategy employed by each acoustic unit cell creates a strong coupling between neighboring unit cells, and the implications that such coupling has on both system performance and stability. Then, we show how a similar control strategy can be used to impose nonlocal coupling in an elastodynamic system using an elastic beam outfitted

with arrays of piezoelectric patches, a commonly studied structure in active metamaterial research. We show how the coupling of neighboring piezoelectric patches results in the highly nonreciprocal transmission of flexural waves. We show how a modified Bernoulli–Euler beam theory effectively models system behavior, providing a powerful design tool for further study. Finally, we discuss future directions of this work, which includes constructing larger one-dimensional arrays of unit cells as well as expanding the concept of action at a distance into higher dimensions.

CHAPTER I

Introduction

1.1 Background

A metamaterial is any engineered material that exhibits properties not seen in naturally occurring media. In wave-bearing systems, such novel properties cause waves to propagate in unique ways. Passive metamaterials typically rely on arrays of subwavelength resonant structures that behave as materials with novel constitutive parameters, most commonly, negative or near-zero mass density [2–11], negative or near-zero bulk modulus [12–15], or both negative or near-zero density and bulk modulus [16–23]. Such characteristics allow for breaking the mass-density law, super-resolution imaging, systems with negative refractive indices, and certain types of three-dimensional metamaterial cloaks [24]. While these engineered materials may achieve remarkable in-band frequency response design goals, their response is limited by Kramers-Kronig type of constraints and typically require resonances to produce the prescribed functionality [25]. Active elements (i.e., sensors and sources) added to the metamaterial can in principle correct the scattering characteristics of the passive structure and remove the constraints of passivity by injecting energy into the impinging wave. However, the complex near-field interactions between the active elements and the geometrical features of the metamaterial may create conditions such that it is difficult to achieve a stable system without exquisite control of the geometry and active control parameters. In many scenarios this may lead to a drastic reduction in useful bandwidth [26]. This work intro-

duces a metamaterial architecture in which the effective acoustic properties are determined entirely by active elements and in which geometrical features play no role in setting the acoustic behavior. We illustrate the concept by studying a nonlocal, active metamaterial whose critical dimensions are subwavelength, and highlight the ability of action at a distance to break acoustic reciprocity.

Interest in nonreciprocal wave propagation has grown substantially in recent years due to their potential applications in the biomedical, noise control, and communication industries [27–30]. Acoustic reciprocity is a fundamental property of passive linear wave-bearing media, requiring that a signal transmitted from a source to a receiver will be unaffected by switching the source and receiver locations [31]. This trait is remarkably robust, holding in systems with a variety of material properties and configurations (e.g., lossy viscoelastic media [32], the presence of scatterers, or fluid-structure interaction [33–35]). However, acoustic metamaterials have proven capable of breaking reciprocity using a variety of mechanisms through the careful design of subwavelength structural and dynamical properties. For instance, combinations of nonlinearities, biasing of the background media, and phononic bandgap materials [26, 36–41] have been used to elicit directionally dependent wave propagation in passive metamaterials. Active metamaterials have been developed with the aim of achieving exceptional control over wave propagation, particularly in the subwavelength regime. These strategies include, but are not restricted to, spatio-temporal modulation of material properties [42–49], Willis coupling [50–53] and real-time boundary impedance control using a distributed network of sensors and electrodynamical transducers [54].

Most of these methods suffer from one or more of the following limitations: the introduction of unwanted harmonic tones that require subsequent demodulation, narrow-band functionality (meaning reciprocity is broken over a very limited range of frequencies), or the disruption of mean flow in fluid systems. The new approach we introduce here overcomes these limitations and breaks reciprocity by relying on the spatial separation of sensors and transducers to create a nonlocal active metamaterial (NAM) system. We demonstrate ex-

perimentally how a NAM system is capable of generating large, broadband, subwavelength nonreciprocity in both acoustic and elastodynamic systems that outperforms existing techniques, even in systems with a single NAM unit cell. We show how the frequencies at which this behavior is centered can be selected by appropriate tuning of the controlling electronics, providing a flexibility in performance design not seen in other acoustic metamaterials.

1.2 The Physics of Metamaterials

Perhaps the simplest system to consider in understanding how engineered effective material parameters can be used to manipulate sound is a one-dimensional (1D) air domain, where the acoustic pressure, p, is assumed to be harmonic in time. If the acoustic pressure is of the form $p(x,t) = P(x)e^{j\omega t}$, the time-invariant pressure, P, at any location, x, is governed by the Helmholtz equation,

$$\frac{d^2P(x)}{dx^2} + k^2P(x) = 0, \tag{1.1}$$

with the wavenumber, $k = \omega/c$, where ω is the angular frequency, and c is the speed of sound in air. The speed of sound depends on the density, ρ, and bulk modulus, B, of air. Solutions to Eq. 1.1 represent plane waves that propagate in the x-direction, and take the form

$$P(x) = Ae^{\mp jkx}, \tag{1.2}$$

where A is an arbitrary complex coefficient to be determined by applying boundary conditions to the domain and $j = \sqrt{-1}$. The sign in the exponent indicates the direction of travel of the wave, negative for waves traveling in the positive-x direction and vice versa. Both ρ and B are constant and positive in air and hence so is k and thus pressure waves propagate in a lossless and nondispersive way. Given the ability to select ρ and B such that they became frequency dependent or negative over a given frequency range, such a material

would be dispersive and feature band gaps (frequencies over which waves are evanescent and do not propagate) [27]. Such a level of control is provided by acoustic metamaterials.

Typically, metamaterials are not homogeneous media, but rather consist of networks of carefully designed subwavelength unit cells which together act like a bulk material with novel constitutive properties. As an example, the metamaterial shown in Fig. 1.1(a) consists of an array of Helmholtz resonators, each of which serves as a single unit cell of the structure [12]. Waves with wavelengths that are large compared to these resonator dimensions and separation distances propagated through the system in the same way as they would through a homogeneous fluid with an elastic modulus that followed the profile shown in Fig. 1.1(b), where it can be seen that near 33 kHz, $\mathrm{Re}(E) = 0$ and $\mathrm{Im}(E) < 0$, leading to a band gap in the dispersion relation of the system.

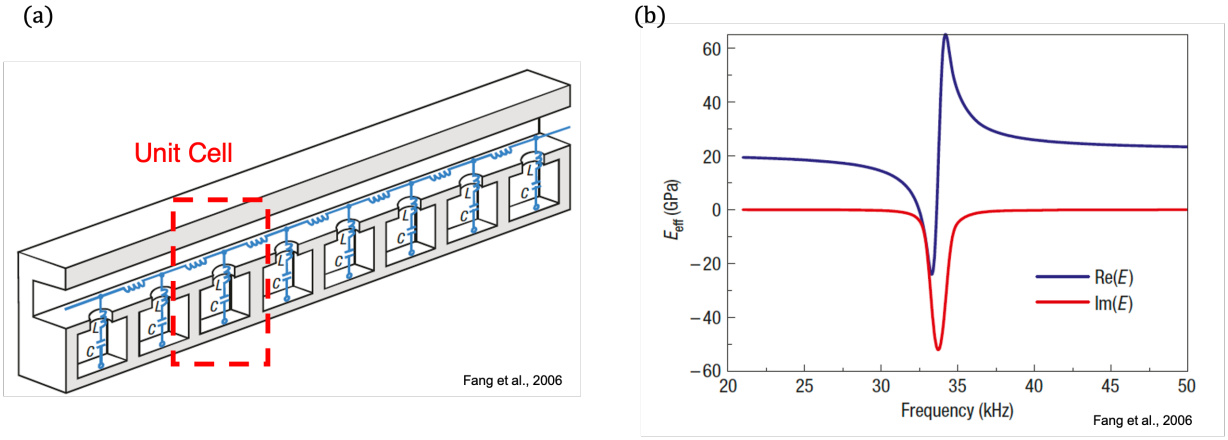

Figure 1.1: A negative bulk modulus metamaterial with each unit cell consisting of a Helmholtz resonator. The array of unit cells (a) effectively created a system with the bulk modulus profile shown in (b). Near 33 kHz, $\mathrm{Re}(E) = 0$ and $\mathrm{Im}(E) < 0$, leading to a band gap in the dispersion relation of the system.

Considering metamaterials in terms of their effective properties can be computationally more efficient, simplifying the analysis of large arrays of complex unit cells, and can provide physical insights that might otherwise be obscured by the structural complexity of the system. Further, while many metamaterials can be classified in terms of how they affect properties of air-like fluids, i.e., ρ and B, many metamaterials behave in ways that cannot

be replicated with any combination of ρ and B. One such system is the subject of this research, and is introduced in the following section.

1.3 A Nonlocal Active Metamaterial

The conceptual framework for the metamaterial presented is introduced as a variation of the 1D air domain governed by Eq. 1.1 discussed in the previous section, where now the pressure at any location x depends upon the pressure at some distance δx away, scaled by a factor of G (see Fig. 1.2(a)). Such behavior can be modelled by adding a non-local inhomogeneous term to Eq. 1.1, giving

$$\frac{d^2P(x)}{dx^2} + k^2P(x) = GP(x - \delta x). \tag{1.3}$$

Substituting wave solutions of the form $P(x) = Ae^{j\zeta x}$ into Eq. 1.3, the relationship between wavenumber and wave frequency (known as the dispersion relation) can be expressed as

$$\zeta^2 + k^2 = Ge^{-j\zeta\delta x}, \tag{1.4}$$

where ζ is the wavenumber. Due to the exponential term on the right-hand side of Eq. 1.4, there are an infinite number of complex root loci and the equation is not even in ζ, leading to unusual dispersion characteristics of the system. The real and imaginary parts of the first two root loci for two nonzero values of G are plotted in Fig. 1.2(b) and Fig. 1.2(c). The root loci associated with right-traveling and left-traveling waves are shown in blue and red, respectively. Plotted for reference in black are the root loci for $G = 0$, which represent the nondispersive and purely real wavenumber loci $\zeta_{-/+} = \pm k = \pm\omega/c$. The arrows on each plot indicate the direction of increasing G. For both root loci with $G \neq 0$, the allowed waves are purely evanescent at low frequencies and asymmetric about the ordinate, indicating a directional dependence that violates the fundamental principle of acoustic reci-

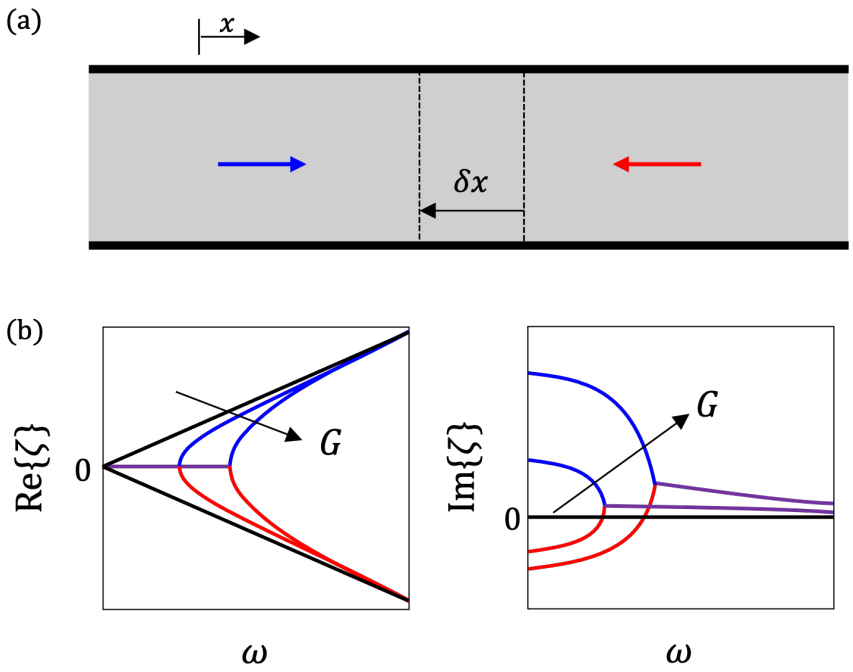

Figure 1.2: Behavior of a nonlocal active metamaterial (NAM) system. (a) Example configuration of the NAM concept applied to an airborne acoustic medium. The pressure at any location x depends upon the pressure a distance δx away, scaled by a factor of G. (b) The real part and (c) imaginary part of the first two root loci of the complex wavenumber solutions to Eq. 1.4 indicate that the NAM system is dispersive with band gaps at low frequencies as well as nonreciprocal, with waves travelling to the right (blue) propagating differently than waves travelling to the the left (red). Black lines corresponding to the case where $G = 0$ are included for reference.

procity. The loci for both choices of nonzero gains exhibit a bifurcation point in frequency beyond which both root loci exhibit decay in the positive-x direction and growth in the negative-x direction. Increasing G changes the asymmetry of the evanescent component of the wavenumber, increases the frequency where the bifurcation point occurs, and eventually results in instability.

To determine whether the dispersion behavior of the NAM system could be realized in practice, the structure shown Fig. 1.3 was considered. The structure is composed of an array of unit cells each consisting of an acoustic source driven by a controller that applied a gain G to signals from an acoustic probe, with each source separated from its respective probe

by a distance δx. This discrete system can be modeled with

$$\frac{d^2P(x)}{dx^2} + k^2P(x) = \sum_{i=1}^{n} GP(x_i^p)\delta(x - x_i^s), \tag{1.5}$$

where n is the number of cells, and x_i^p and x_i^s are the locations of the probe and source of the i^{th} unit cell, respectively. In anticipation of fabricating a larger probe-source array, the

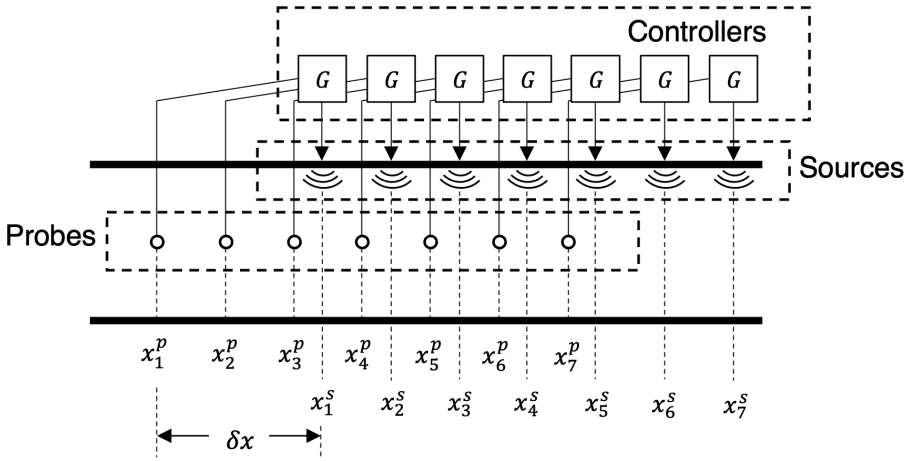

Figure 1.3: Physical implementation of nonlocal media using a nonlocal active metamaterial (NAM) system with n unit cells, where x_i^p and x_i^s are the locations of the probe and source of the i^{th} unit cell, respectively.

characteristics of a single unit cell will be first considered in the following chapter.

1.4 Overview and Outline

The work presented in this dissertation serves to bolster action at a distance as a general concept and as a means of breaking reciprocity in wave-bearing systems. Chapter II introduces the constitutive unit cell for a nonlocal active metamaterial (NAM) system. First, the behavior of an ideal unit cell is analyzed and discussed. Next, we expand the ideal model and show how a fully coupled acoustic model can adequately predict the performance and stability of both full-wave simulations and experimental data.

In Chapter III, the single cell system is expanded to include a second cell. The complex interactions between adjacent cells and their implications on performance and stability are

discussed for the ideal case, first with an analysis of the effects of changing the individual controller gains, then with an analysis of the effects of adjusting the relative cell spacing. Then, as in the case of a single cell, we show how the ideal system behavior qualitatively matches that of a system with real acoustic sources and present experimental results showing the significant improvement in performance in systems with multiple unit cells.

In Chapter IV, we discuss how action at a distance in dispersive systems gives rise to highly nonreciprocal flexural wave transmission. We show how an elastic beam outfitted with piezoelectric patches, a commonly studied structure in metamaterial research, can be employed to impose action at a distance in an elastic domain. We detail the approach used to model the elastic beam and piezoelectric patches used in experiments and show how the model predicts real data to a high degree of precision.

Finally, in Chapter V, the work presented is summarized and its key contributions listed, followed by a brief discussion of possible directions for future work.

CHAPTER II

The NAM Unit Cell

2.1 Introduction

The NAM unit cell is the fundamental building block of the NAM system introduced in the previous section. A diagram of an ideal unit cell is shown in Fig. 2.1. The unit cell consists of an ideal acoustic point source acting at x_s, driven by a controller that applies a gain G to a signal from an acoustic probe measuring pressure $p(x_p, t)$ a distance δx away from the source. For simplicity, here we assume the ideal point source can exactly reproduce the pressure measured at x_p at all frequencies. Later, this model will be expanded to include the dynamics of more realistic acoustic sources. For pressures in the domain of the form

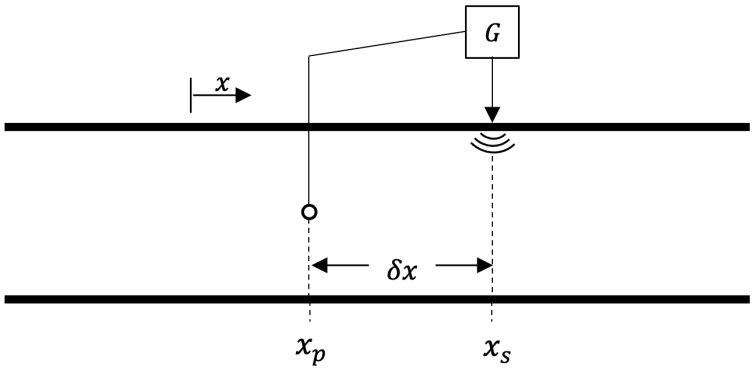

Figure 2.1: The ideal unit cell of a larger NAM system consisting of an acoustic source located at x_s, driven by a controller that applies a gain G to a signal from an acoustic probe a distance δx away from the source located at x_p.

$p(x,t) = P(x)e^{j\omega t}$, this system can be modeled by the following modified Helmholtz equation,

$$\frac{d^2P(x)}{dx^2} + k^2P(x) = GP(x_p)\delta(x - x_s), \tag{2.1}$$

where $k = \omega/c$, ω is the radian frequency, and c is the speed of sound in air. Using standard arguments, a proof that the ideal unit cell governed by Eq. 2.1 is nonreciprocal is presented in the following section.

2.2 Proof of Nonreciprocity

We consider the ideal unit cell shown again in Fig. 2.2. Reciprocity of this system can be analyzed using the following standard arguments [31]. By adding a source and a receiver to the system in the two different configurations shown in Fig. 2.2, we have

$$\frac{d^2P^I(x)}{dx^2} + k^2P^I(x) = GP^I(x_p)\delta(x - x_s) + Q^I\delta(x - x_1) \tag{2.2}$$

$$\frac{d^2P^{II}(x)}{dx^2} + k^2P^{II}(x) = GP^{II}(x_p)\delta(x - x_s) + Q^{II}\delta(x - x_2), \tag{2.3}$$

where $P^i(x)$ is the pressure field resulting from the source Q^i, $i = I, II$. Multiplication of Eq. 2.2 by $P^{II}(x)$ and Eq. 2.3 by $P^I(x)$ yields

$$P^{II}(x)\frac{d^2P^I(x)}{dx^2} + k^2P^{II}(x)P^I(x) = GP^{II}(x)P^I(x_p)\delta(x - x_s) + P^{II}(x)Q^I\delta(x - x_1), \tag{2.4}$$

$$P^I(x)\frac{d^2P^{II}(x)}{dx^2} + k^2P^I(x)P^{II}(x) = GP^I(x)P^{II}(x_p)\delta(x - x_s) + P^I(x)Q^{II}\delta(x - x_2). \tag{2.5}$$

Subtracting Eq. 2.5 from Eq. 2.4 and integrating from $(-\infty, \infty)$ results in

$$\int_{-\infty}^{\infty} P^{II}(x)\frac{d^2P^I(x)}{dx^2}dx - \int_{-\infty}^{\infty} P^I(x)\frac{d^2P^{II}(x)}{dx^2}dx = G\int_{-\infty}^{\infty} P^{II}(x)P^I(x_p)\delta(x-x_s)dx$$
$$-G\int_{-\infty}^{\infty} P^I(x)P^{II}(x_p)\delta(x-x_s)dx + \int_{-\infty}^{\infty}\left[P^{II}(x)Q^I\delta(x-x_1) - P^I(x)Q^{II}\delta(x-x_2)\right]dx. \tag{2.6}$$

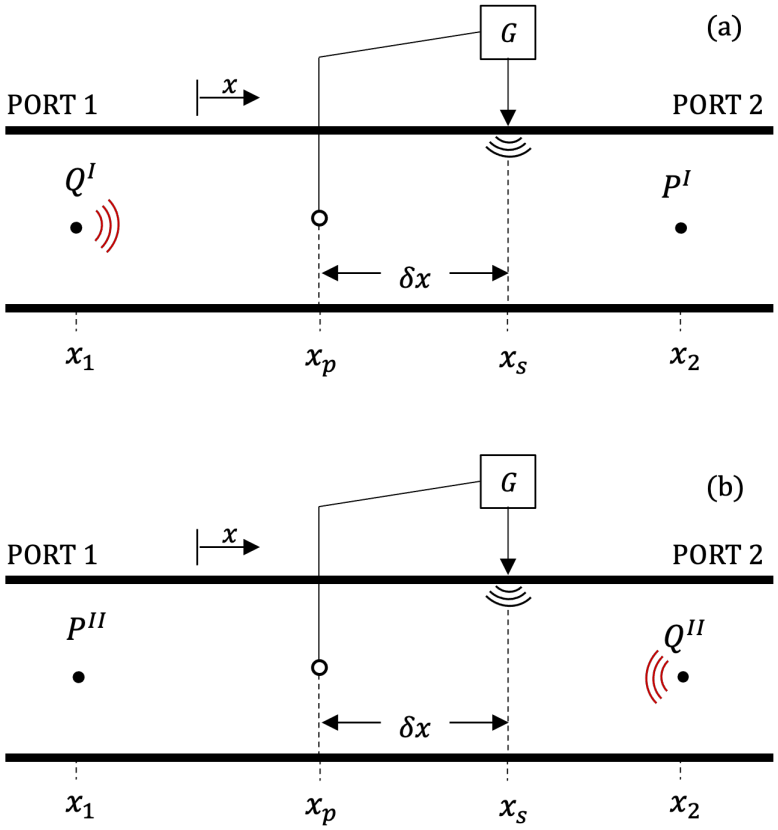

Figure 2.2: One-dimensional acoustic domain with pressure source at location x_s equal to the pressure at location a distance δx away from the source (x_p) multiplied by a gain G. (a) A source Q^I is placed at x_1 and the pressure P^I is measured at x_2. (b) A source Q^{II} is placed at x_2 and the pressure P^{II} is measured at x_1. Reciprocity of the system dictates that the transfer function $P^I(x_2)/Q^I$ in (a) is equal to the transfer function $P^{II}(x_1)/Q^{II}$ in (b).

Applying Green's theorem, Eq. 2.6 can be rewritten as

$$P^{II}(x)\frac{dP^{I}(x)}{dx}\bigg|_{-\infty}^{\infty} - \int_{-\infty}^{\infty}\frac{dP^{II}(x)}{dx}\frac{dP^{I}(x)}{dx}dx - P^{I}(x)\frac{dP^{II}(x)}{dx}\bigg|_{-\infty}^{\infty} + \int_{-\infty}^{\infty}\frac{dP^{I}(x)}{dx}\frac{dP^{II}(x)}{dx}dx = G\left[P^{II}(x_s)P^{I}(x_p) - P^{I}(x_s)P^{II}(x_p)\right] + P^{II}(x_1)Q^{I} - P^{I}(x_2)Q^{II}. \tag{2.7}$$

The left hand side of Eq. 2.7 vanishes by applying the Sommerfeld radiation boundary condition [55, 56]. Eq. 2.7 simplifies to

$$-G\left[P^{II}(x_s)P^{I}(x_p) - P^{I}(x_s)P^{II}(x_p)\right] = P^{II}(x_1)Q^{I} - P^{I}(x_2)Q^{II}. \tag{2.8}$$

Eq. 2.8 shows that the system is acoustically reciprocal (i.e. $P^{II}(x_1)Q^{I} = P^{I}(x_2)Q^{II}$) only when $P^{II}(x_s)P^{I}(x_p) = P^{I}(x_s)P^{II}(x_p)$, which happens at discrete frequencies discussed in the next section. At all other frequencies, the system is nonreciprocal.

2.3 Behavior of the Ideal System

2.3.1 Scattering Behavior

To study the behavior of the ideal unit cell, we consider solutions to Eq. 2.1 expressed in terms of the system's scattering matrix [57], denoted by $\widetilde{\boldsymbol{S}}$, which relates the left-going and right-going waves before and after the unit cell, and can be expressed as

$$\widetilde{\boldsymbol{S}} = \begin{bmatrix} S_{11} & S_{12} \\ S_{21} & S_{22} \end{bmatrix} = \frac{1}{\widetilde{\Delta}}\begin{bmatrix} -\widetilde{G}\frac{e^{jk\delta x}}{2jk\delta x} & 1 \\ \left(1 - \widetilde{G}\,\mathrm{sinc}\,k\delta x\right) & -\widetilde{G}\frac{e^{-jk\delta x}}{2jk\delta x} \end{bmatrix}, \tag{2.9}$$

where

$$\widetilde{\Delta} = 1 + \widetilde{G}\frac{e^{-jk\delta x}}{2jk\delta x}. \tag{2.10}$$

Expressions for the scattering matrix are grouped in terms of a dimensionless frequency, $k\delta x$, and dimensionless gain, $\widetilde{G} = G\delta x$, where G is the controller gain and δx is the distance between the source and probe. A detailed derivation of $\widetilde{\boldsymbol{S}}$ can be found in Appendix A.1. The diagonal terms of the scattering matrix, S_{11} and S_{22}, represent the reflection coefficients for waves incident from either direction, whereas the off-diagonal terms, S_{12} and S_{21} represent the transmission coefficients. For $\widetilde{G}$ set to $\pi/2$, the transmission and reflection coefficients for waves incident in either direction across the unit cell are plotted in Fig. 2.3(a) and Fig. 2.3(b), respectively, over a dimensionless frequency range from zero to π, which corresponds to separation distances that are half the incident wavelength, λ, or less. While the reflection coefficient magnitudes are the same in either direction, the transmission coefficients are dramatically different over nearly the entire frequency range, converging only at the special frequencies where the system is reciprocal (i.e., when $S_{21} = S_{12}$). These frequencies occur when $k\delta x = n\pi$ ($n \in \mathbb{Z}^+$). At these frequencies, δx is an integer multiple of $\lambda/2$ and $\mathrm{sinc}(k\delta x) = 0$. At high frequencies ($k\delta x >> \pi$), the system largely reverts to a passive waveguide, where $S_{11} = S_{22} = 0$ and $S_{12} = S_{21} = 1$. The most dramatic difference in transmission occurs when $S_{21} = 0$, where a wave incident from the left is exactly cancelled by the pressure emitted from the source. We quantify the level of nonreciprocity by defining an isolation level $\mathcal{I}$ as the ratio of the magnitudes $|S_{12}|$ and $|S_{21}|$ in the decibel scale as

$$\mathcal{I} = 20\log_{10}\left(\left|\frac{1}{1-\widetilde{G}\,\mathrm{sinc}\,k\delta x}\right|\right). \tag{2.11}$$

The maximum $\mathcal{I}$ occurs when $1 - \widetilde{G}\,\mathrm{sinc}\,k\delta x = 0$ (a relationship solved graphically in Fig. 2.3(d)) which is the same condition for which $S_{21} = 0$ (Eq. 2.9). As shown in the middle curve in Fig. 2.3(c), when $\widetilde{G} = 0.5\pi$, the peak $\mathcal{I}$ occurs when $\delta x = 0.25\lambda$. The adjacent curves in Fig. 2.3(c) show how the peak frequency, f_{pk}, for constant $\widetilde{G}$ increases with $\widetilde{G}$. When $\widetilde{G}$ is increased to 0.7π, f_{pk} increases ($\delta x \approx 0.3\lambda$), while when $\widetilde{G}$ is decreased to 0.4π, f_{pk} decreases ($\delta x \approx 0.2\lambda$), a 50% change in frequency. These changes in $\widetilde{G}$ can be

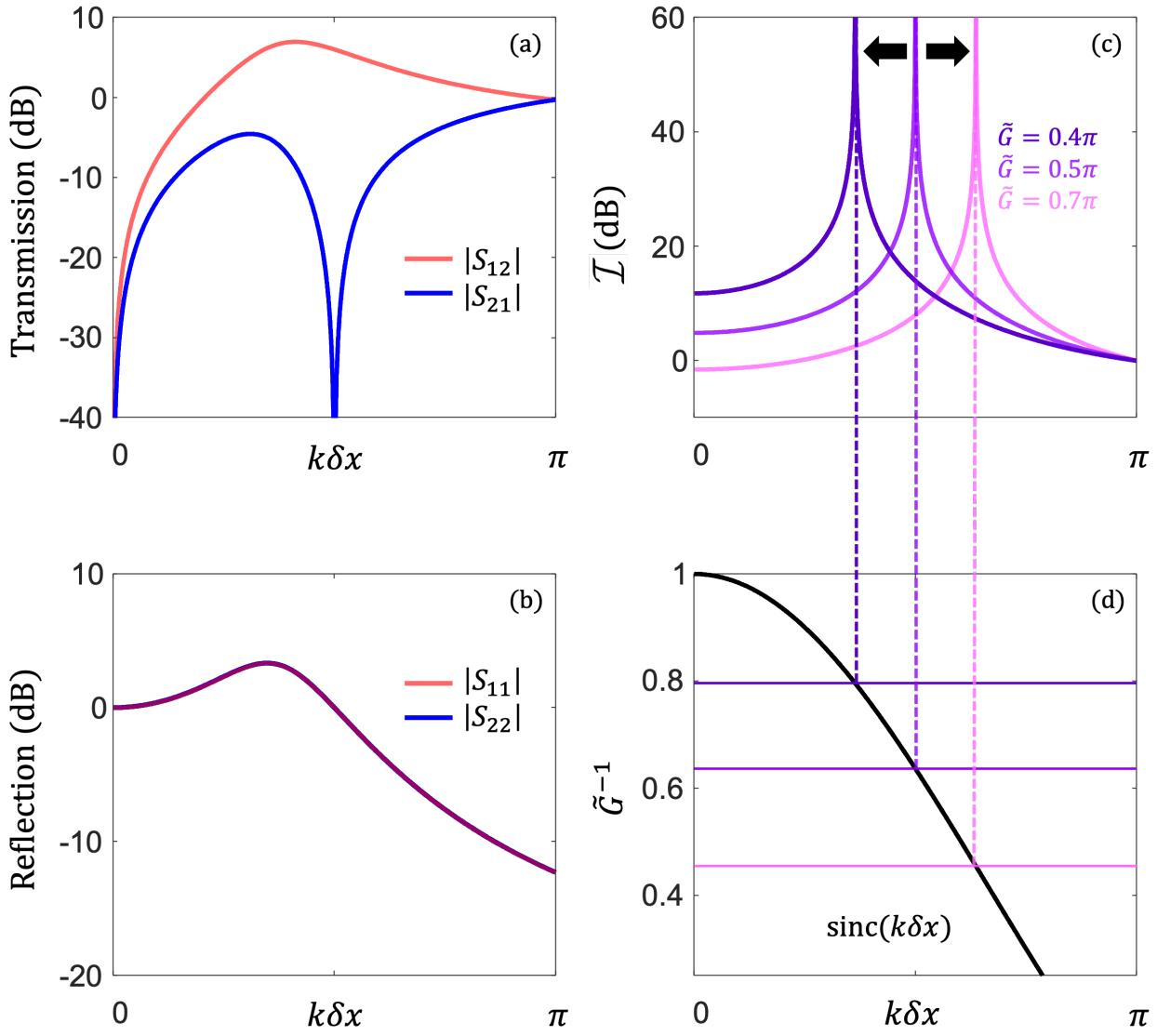

Figure 2.3: Transmission and reflection behavior of the NAM unit cell. (a) Directional transmission coefficients across the NAM unit cell for $\widetilde{G} = 0.5\pi$ demonstrate the highly nonreciprocal nature of the system, greatest at the null in left-to-right transmission. (b) Reflection coefficient magnitudes for $\widetilde{G} = 0.5\pi$ show bidirectional symmetry in the reflection coefficient ($|S_{11}| = |S_{22}|$). (c) Isolation factors for $\widetilde{G} = 0.5\pi$, $\widetilde{G} = 0.4\pi$, and $\widetilde{G} = 0.7\pi$ demonstrate the flexibility of the NAM technique in positioning the $\mathcal{I}$ peak, i.e., where there is a null in $|S_{21}|$. (d) Graphical solutions for the frequencies where peaks in $\mathcal{I}$ occur (where $\widetilde{G}^{-1}$ intersects the sinc($k\delta x$) curve), which can be shifted by modulating only the electronics of the NAM controller.

imposed by either modifying the probe-source separation distance δx, which is fixed once the NAM unit cell is fabricated, or by varying G, the controller transfer function. The latter

approach is advantageous because we have the ability to artificially resize our unit cell just through the controlling electronics of the system. Note that for $\widetilde{G} \leq 1$, perfect cancellation cannot be achieved and $\mathcal{I}$ becomes far less dramatic, hence defining a lower bound for the dimensionless gain. The upper bound of $\widetilde{G}$ is dictated by system stability.

2.3.2 Stability Conditions

As is typical in active systems, the ideal unit cell has the potential to introduce instabilities into the system. It is therefore necessary to understand the conditions necessary for system stability. In this section, we discuss two techniques to determine stability conditions for the ideal unit cell.

2.3.2.1 The Lambert W function

Recall that each of the scattering matrix elements in Eq. 2.9 were divided by $\widetilde{\Delta}$, which, replacing $j\omega$ by the Laplace variable, s, can be expressed as

$$\widetilde{\Delta}(s) = 1 + \widetilde{G}\frac{e^{-s\delta x/c}}{2s\delta x/c}. \tag{2.12}$$

The poles of the ideal unit cell, which must lie in the left-hand side of the Laplace domain, where $\mathrm{Re}\{s\} < 0$, can be located by finding the roots of Eq. 2.12, which can be expressed in closed form as

$$s = \frac{c}{\delta x} W\left(-\frac{\widetilde{G}}{2}\right), \tag{2.13}$$

where $W(x)$ is the Lambert W function [58–60], which yields solutions y to the expression $y = xe^x$. Though $W(x)$ is a multivalued function, limits on $\widetilde{G}$ can be determined from the principal branch of the function, which is plotted in red in Fig. 2.4. For $0 \leq \widetilde{G} < \pi$, the real part of s is positive, indicating that the poles of the NAM unit cell are located in the left-hand side of the s-plane, and thus the system is stable. Additional branches are plotted

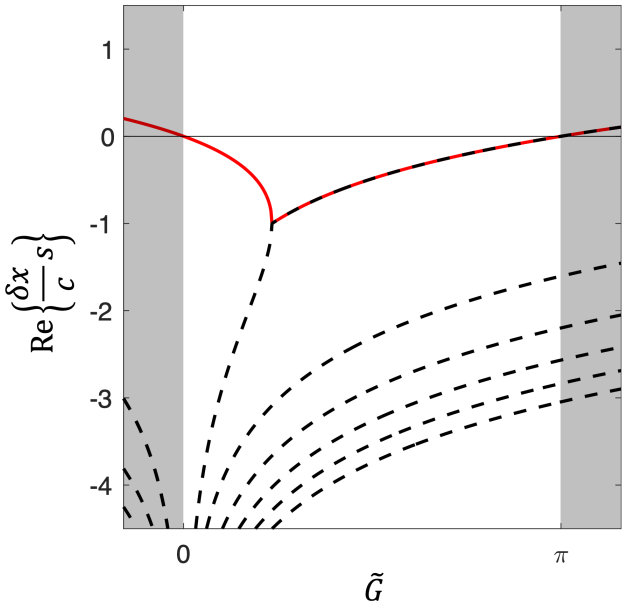

Figure 2.4: Branches of the Lambert W function. The principal branch (plotted in red) show that for $0 \leq \widetilde{G} < \pi$, the real part of s, made dimensionless using δx and c, is less than zero, indicating that the poles of the NAM unit cell remain in the left-hand side of the s-plane, resulting in a stable system. Additional branches are plotted as dashed lines for reference.

as dashed lines in Fig. 2.4 for reference. Considering the lower bound $\widetilde{G}$ established at the end of Section 2.3.1, our total operating range for $\widetilde{G}$ is

$$1 \leq \widetilde{G} < \pi \tag{2.14}$$

The Lambert W function is a useful tool in evaluating the stability of an ideal NAM unit cell. However, it will be seen that when we expand our model to predict the behavior of less ideal and more realistic systems, expressions for their transfer functions are not of the form in which the Lambert W function is useful. Therefore, in the following section, we show how the stability bounds found using the Lambert W function can also be found using the Nyquist Stability Criterion.

2.3.2.2 Nyquist Stability Criterion

Nelson and Elliot [1] present a concise explanation of how the Nyquist stability criterion provides a means of determining the stability of a closed loop system through an evaluation of its open loop transfer function. Their argument is summarized as follows. The poles of a closed loop system with a transfer function, $T(s)$, of the form

$$T(s) = \frac{1}{1 + L(s)} \tag{2.15}$$

where $s = \sigma + j\omega$ is the Laplace variable, σ and ω are real numbers, and $L(s)$ is the open loop transfer function of the system, can be located by finding the zeros of its denominator,

$$F(s) = 1 + L(s). \tag{2.16}$$

If $F(s)$ is analytic for all but a finite number of points, is single valued, and maps every point in the s-plane to one and only one point in the $F(s)$ plane (except for singular points), then a closed contour in the s-plane which does not pass through any singularities of $F(s)$ will map to a contour in the $F(s)$ plane that encircles the origin N number of times according to

$$N = Z - P, \tag{2.17}$$

where Z and P are the numbers of zeros and poles, respectively, of $F(s)$ enclosed by the the contour in the s-plane. If it is assumed that $L(s)$ is stable in the region enclosed by the contour, $F(s)$ will have no poles, and $P = 0$. For the closed loop system to be stable, it must have no poles in the right half of the s-plane. Therefore, mapping a contour which encloses the right half of the s-plane, known as the Nyquist contour, to the $F(s)$ plane, generates a plot, known as the Nyquist plot, which encircles the origin only if the closed loop system is unstable (again assuming $L(s)$ is stable in the region enclosed by the Nyquist contour). The Nyquist contour is shown in Fig. 2.5. It can be seen that the Nyquist contour encloses the

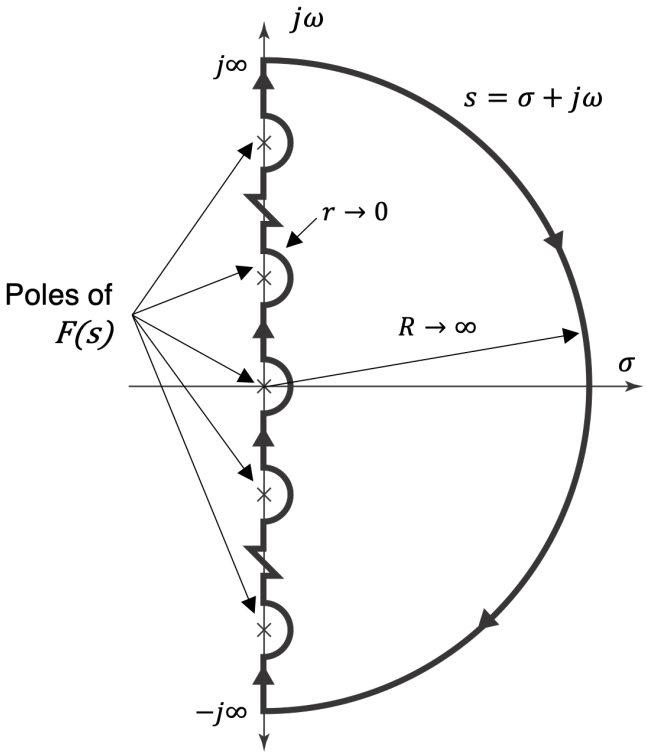

Figure 2.5: The Nyquist contour [1] encloses the right half of the s-plane as $R \to \infty$ and $r \to 0$, where r is the radius of semicircles included to avoid singularities of $F(s)$ on the $j\omega$-axis

right half of the s-plane as $R \to \infty$ and $r \to 0$, where r is the radius of semicircles included to avoid singularities of $F(s)$ on the $j\omega$-axis. Usually, the Nyquist plots are generated by mapping the Nyquist contour onto the $L(s)$ plane, rather than the $F(s)$ plane, and therefore, since $F(s) = 1 + L(s)$, Nyquist plots of the open loop transfer function must not encircle the point $(-1, j0)$ for the closed loop system to be stable.

To illustrate how the Nyquist stability criterion can be used to evaluate the stability of NAM systems with transfer functions that cannot be expressed in terms of the Lambert W function, it is first used to confirm the stability limits of the ideal unit cell, which were found in the previous section using the Lambert W function. The open loop transfer function for the ideal NAM cell, $\widetilde{L}(s)$ can be determined from Eq. 2.12 as

$$\widetilde{L}(s) = \widetilde{\Delta}(s) - 1 = \widetilde{G}\frac{e^{-s\delta x/c}}{2s\delta x/c}. \tag{2.18}$$

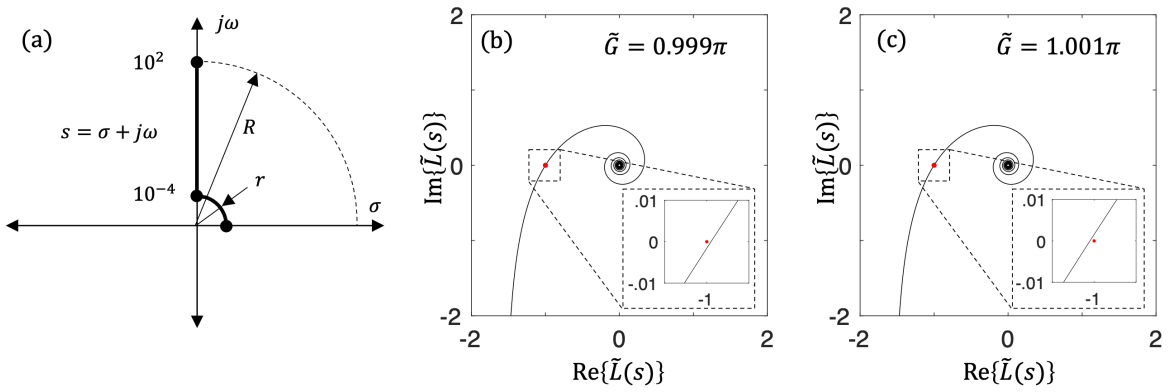

Figure 2.6: Nyquist stability criterion applied to the ideal unit cell. (a) The Nyquist contour used to generate Nyquist plots for $\widetilde{L}(s)$ with $\widetilde{G} = 0.999\pi$ (b) and $\widetilde{G} = 1.001\pi$ (c). The Nyquist plot for $\widetilde{G} = 0.999\pi$ does not encircle the point $(-1, j0)$, shown as a red dot, indicating the system is stable. For $\widetilde{G} = 1.001\pi$, the Nyquist plot does encircle the point $(-1, j0)$, indicating an unstable system. These results are consistent with the upper stability limit found using the Lambert W function.

The Nyquist contour used to generate the Nyquist plot for $\widetilde{L}(s)$ is shown in Fig. 2.6(a). Since $\widetilde{L}(s)$ has a pole at the origin, a semicircle of radius $r = 10^{-4}$ around $s = 0$ is included in the contour. For linear time invariant systems, like the ideal NAM unit cell, the Nyquist plot of $\widetilde{L}(s)$ for portions of the contour where $s = j\omega < 0$ is a mirror image about the σ-axis of the contour where $s = j\omega > 0$, and is thus omitted. As $s = j\omega \to \infty$, $\widetilde{L}(s) \to 0$, and so the Nyquist contour at $s = j\omega = \infty$ maps to the origin, and it was determined that $R = 100$ was sufficiently large to generate a useful Nyquist plot. The Nyquist plot for $\widetilde{L}(s)$ with $\widetilde{G} = 0.999\pi$ and $\widetilde{G} = 1.001\pi$ are shown in Fig. 2.6(b) and Fig. 2.6(c), respectively. The Nyquist plot for $\widetilde{G} = 0.999\pi$ does not encircle the point $(-1, j0)$, shown as a red dot, indicating the system is stable. For $\widetilde{G} = 1.001\pi$, the Nyquist plot does encircle the point $(-1, j0)$, indicating an unstable system. These results are consistent with the upper stability limit found using the Lambert W function, and hence will be relied upon throughout this work to evaluate system stability.

2.3.3 Ideal Scattering Behavior: A Physical Interpretation

To understand physically what is happening at the critical frequency where $\mathcal{I}$ is maximized (i.e., where $|S_{21}| = 0$), it can be helpful to look at the steady state response of the system shown in Fig. 2.7, which illustrates how incident waves (shown in blue) interact with waves generated by the source (shown in red) to form the total transmitted and reflected fields (shown in black). For waves incident in either direction with magnitude 1, the source generates waves also with magnitude 1, so in either direction, the wave from the source forms

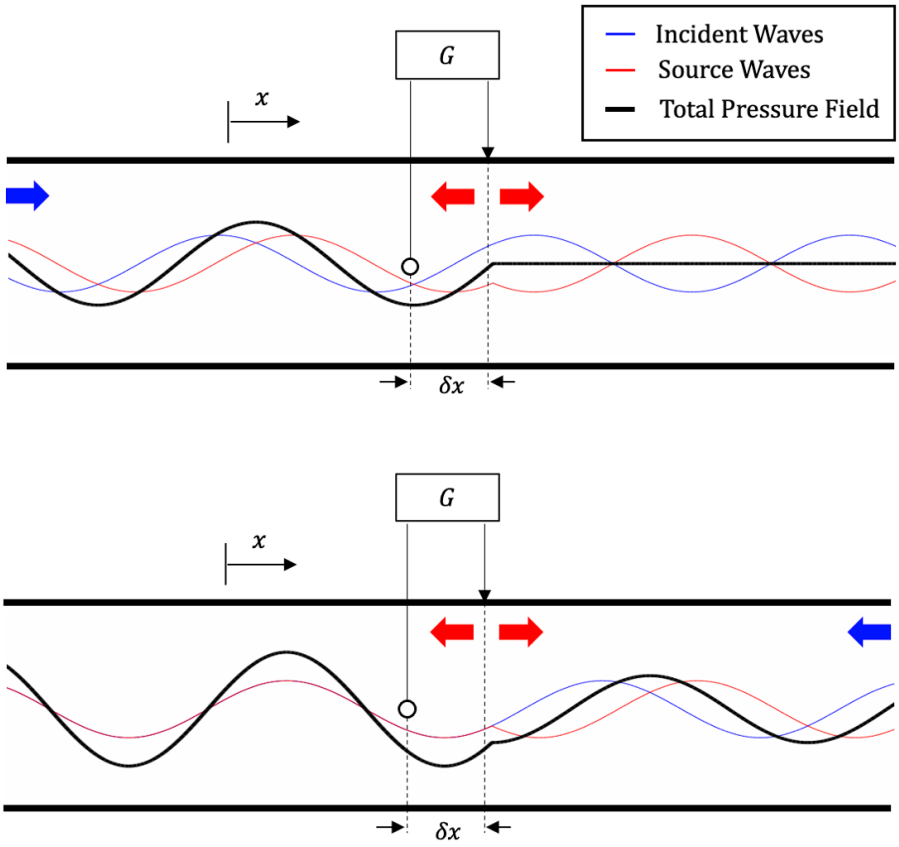

Figure 2.7: Incident waves (blue) interact with waves generated by the source (red) to form the total transmitted and reflected fields (black). For waves incident in either direction with magnitude 1, the source generates waves also with magnitude 1, so in either direction, the wave from the source forms standing waves of magnitude 2 with the incident waves upstream from the source. Downstream however, for waves incident from the left, pressure from the source perfectly cancels the incident wave resulting in zero transmission. In the opposite direction, the downstream waves interfere constructively, resulting in a transmitted wave of magnitude 2.

a standing wave of magnitude 2 with the incident waves upstream from the source. Downstream however, for waves incident from the left, pressure from the source perfectly cancels the incident wave resulting in zero transmission. In the opposite direction, the downstream waves interfere constructively, resulting in a transmitted wave of magnitude 2.

This physical representation also demonstrates nicely why perfect cancellation cannot occur for waves incident from the right, because if S_{12} could be zero, this would imply that the pressure at the probe ($P(x_p)$) would also be zero. Since the source strength is proportional to $P(x_p)$, it is then impossible for the active source with amplitude zero to cancel the incoming wave from the right.

Though initially we set out to construct a nonlocal metamaterial consisting of large arrays of cells, the attractive qualities of the ideal unit cell discussed in this section (i.e., subwavelength, tunable nonreciprocity) suggested that significant breaks in reciprocity could be achieved with a single unit cell. Therefore, we sought to build and test a real unit cell.

2.4 Behavior of the Experimental System

2.4.1 Expanded One-Dimensional Model

To determine whether the appealing behavior of the ideal unit cell could be realized physically, we first expanded our ideal system model, which relied on the assumption of perfect control of both the controlling electronics and the sound source. To predict and analyze the behavior of the real unit cell, our ideal mathematical model was expanded to include the dynamics and fluid-structure interaction associated with a real acoustic source. Expressions for the scattering matrix, $\bar{\boldsymbol{S}}$, associated with this expanded model are shown in Eq. 2.20. A schematic of the expanded coupled electromechanical-acoustic system model for the real unit cell is shown in Fig. 2.8. The mechanical components of the model are the speaker cone which is represented as a rigid disk with cross sectional area S_d, centered at x_s, with mass M_m, compliance C_m, damping R_m, and a velocity U. The rigid disk moves

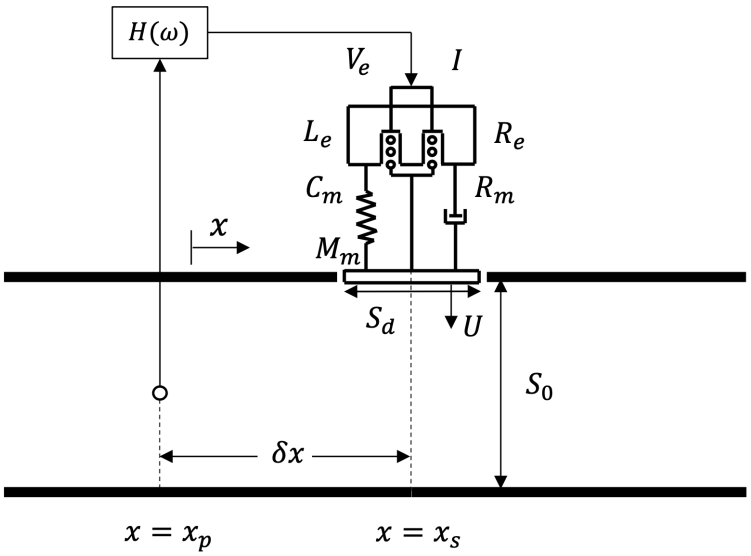

Figure 2.8: Coupled electromechanical-acoustic system schematic for the simplified one-dimensional model used to forward predict experimental measurements. The mechanical components of the model are the speaker cone which is represented as a rigid disk with cross sectional area S_d, centered at x_s, with mass M_m, compliance C_m, damping R_m, and a velocity U. The rigid disk moves with the voice coil of the loudspeaker, which has an electrical resistance and inductance, R_e and L_e, respectively. The electromechanical system is driven by the voltage V_e, equal to the controller transfer function $H(\omega)$ applied to the signal from the microphone located at x_p (Eq. 2.22). V_e induces a current I through the voice coil, generating a force on the voice coil proportional to the product of its magnetic field, B, voice coil wire length, l, and the current I. The density of air is given by ρ_0 and its sound speed by c. The cross sectional area of the waveguide is S_0

with the voice coil of the loudspeaker, which has an electrical resistance and inductance, R_e and L_e, respectively. The electromechanical system is driven by the voltage V_e, equal to the controller transfer function $H(\omega)$ applied to the signal from the microphone located at x_p (Eq. 2.22). V_e induces a current I through the voice coil, generating a force on the voice coil proportional to the product of its magnetic field, B, voice coil wire length, l, and the current I. The density of air is given by ρ_0 and its sound speed by c. The cross sectional area of the waveguide is S_0. The resulting coupled structural–acoustic equations for the expanded 1D

model are:

$$\begin{aligned} Z_e I &= -BlU + V_e, \\ Z_m U &= BlI - P(x_s)S_d, \\ \frac{d^2P}{dx^2} + k^2 P &= \frac{-j\omega\rho_0 U S_d}{S_0}\delta(x - x_s), \end{aligned} \tag{2.19}$$

where the loudspeaker electrical impedance is $Z_e = j\omega L_e + R_e$ and mechanical impedance is $Z_m = j\omega M_m + R_m + 1/j\omega C_m$. The electromechanhical parameters of the loudspeaker (R_e, L_e, B, l, S_d, C_m, M_m, and R_m) were determined experimentally from loudspeaker impedance measurements using techniques that will be detailed in Section 2.4.3. Implicit in Eq. 2.19 are the assumptions that only plane waves propagate in the x-direction, that wavelengths are sufficiently large compared to the source dimensions (so that the loudspeaker can be modeled as a rigid disk acting as a point source), and that δx is large enough to neglect near-field effects from the loudspeaker. To study the validity of these assumptions, we developed comparison full-wave (FW) simulations using a three-dimensional finite element model created in COMSOL Multiphysics®, enabling exploration of the importance of dimensionality and evanescent wave contributions.

As in the ideal case, the scattering matrix for the expanded 1D structural acoustic model, $\bar{\boldsymbol{S}}$, can be determined analytically. Solving Eq. 2.19 we find

$$\bar{\boldsymbol{S}} = \frac{1}{\bar{\Delta}} \begin{bmatrix} -\left(\bar{G}\frac{e^{jk\delta x}}{2jk\delta x} + \kappa\right) & 1 \\ \left(1 - \bar{G}\,\mathrm{sinc}\,k\delta x\right) & -\left(\bar{G}\frac{e^{-jk\delta x}}{2jk\delta x} + \kappa\right) \end{bmatrix} \quad , \tag{2.20}$$

where

$$\begin{aligned} \bar{G} &= -j\frac{\rho_0 c S_d BlH(\omega)k\delta x}{S_0(Z_m Z_e + (Bl)^2)}, \\ \kappa &= \frac{\rho_0 c S_d^2 Z_e}{2S_0(Z_m Z_e + (Bl)^2)}, \\ \bar{\Delta} &= 1 + \kappa + \bar{G}\frac{e^{-jk\delta x}}{2jk\delta x} \quad . \end{aligned} \tag{2.21}$$

Comparing the scattering matrix from the ideal case, $\widetilde{\boldsymbol{S}}$, from Eq. 2.9, with that from the coupled system, $\bar{\boldsymbol{S}}$, from Eq. 2.20, we note a remarkable similarity with two key differences. The first difference is the appearance of κ in the diagonal elements of $\bar{\boldsymbol{S}}$ and in $\bar{\Delta}$. The term κ is associated with the fluid-structure interaction between the speaker cone and air in the waveguide. For the system we implemented, we found that κ was small and had minimal contribution to the behavior of the system as predicted by $\bar{\boldsymbol{S}}$. Second, and more significantly, $\bar{G}$ is more elaborate than $\widetilde{G}$ as $\bar{G}$ includes the frequency dependent electromechanical dynamics of the loudspeaker itself as well as the effects of an analog single-pole low-pass filter used to mitigate effects from higher order modes not accounted for in our 1D model (Eq. 2.22). Despite these differences, we will show that the desired features observed in the ideal model (large, subwavelength, tunable nonreciprocity) are recapitulated in the real system.

To implement action at a distance, the signal from the microphone is amplified and filtered so that the output voltage applied to the loudspeaker, V_e, is given by

$$V_e = H(\omega)P(x_p) = \underbrace{\frac{H_g}{1 + jf/f_{lp}}}_{H(\omega)} P(x_p) \quad , \tag{2.22}$$

where H_g is the gain supplied by an audio amplifier, f_{lp} is the corner frequency of a first order analog low-pass filter, implemented using discrete circuit components on a breadboard, and $P(x_p)$ is the pressure sensed by the microphone at $x = x_p$. Following the development and verification of this expanded system model, we proceeded with building and testing an experimental unit cell.

2.4.2 Experimental Unit Cell and Test Setup

Shown in Fig. 2.9 is an experimental NAM unit cell consisting of a 3D printed section of a waveguide 15 cm long with an inner cross sectional area of 5 cm x 5 cm, for which the cut-off frequency is 3376 Hz (Fig. 2.9(a)), which held our probe, an ADMP401 MEMS microphone

on a SparkFun Electronics breakout board (Fig. 2.9(c)), and our source, a 4 Ohm Dayton Audio 1-1/4 inch mini speaker, Model CE30P-4 (Fig. 2.9(b)), with a separation distance of 10 cm. We fabricated two unit cells, one composed of Polylactic Acid (PLA), shown in Fig. 2.9(a), and one composed of Acrylonitrile Butadiene Styrene (ABS) plastic, which appears with the full experimental setup in Fig. 2.10(a). The two unit cells were the same in geometry and in function, except the PLA section contained additional slots to allow for additional MEMS microphone locations to be used in future testing. These slots were sealed with un-powered MEMS breakeout boards. The type of material did not have an influence on system performance, and the unit cells could be used interchangeably.

Experimental testing was performed using the system shown in Fig. 2.10(a). The signal from the MEMS microphone was sent through an Onkyo audio amplifier (Fig. 2.10(b)), which centered the signal about 0 V and applied a variable proportional gain. The signal was also transmitted through one of three single-pole low-pass filters, each with different corner frequencies (see Table 4.4). For each different filter, a slightly different proportional

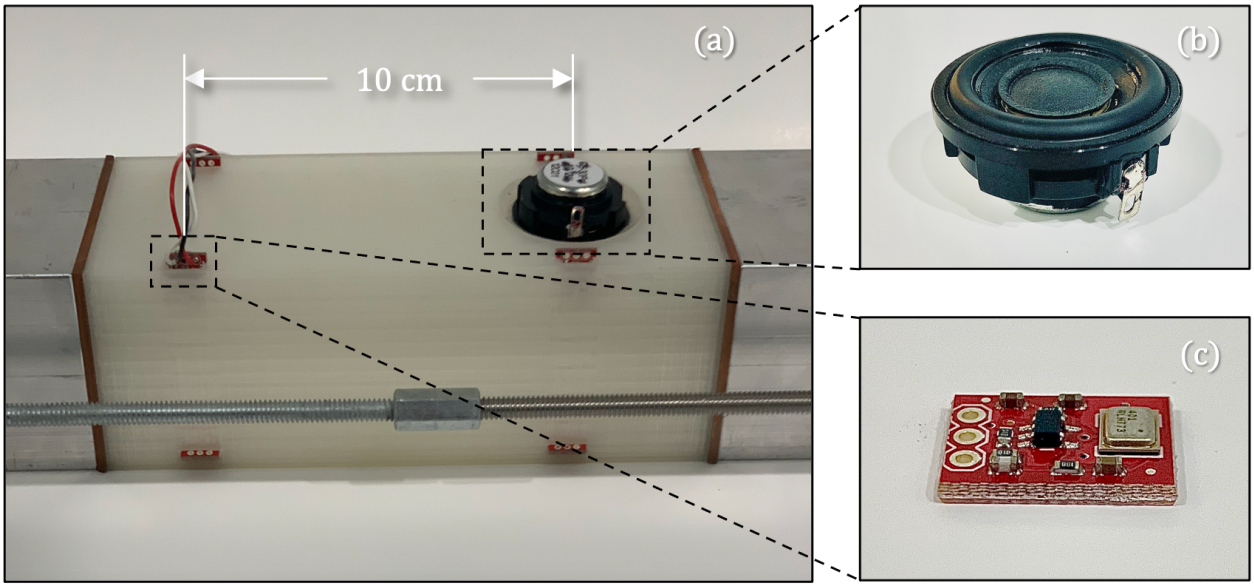

Figure 2.9: Experimental Unit Cell. (a) Unit cell fabricated for experimental testing containing a loudspeaker source (b) actuated with signals measured from a MEMS microphone probe (c) separated by 10 cm from the source. Signals from the probe were filtered and sent to an audio amplifier to apply the desired gain and phase shift of the signal.

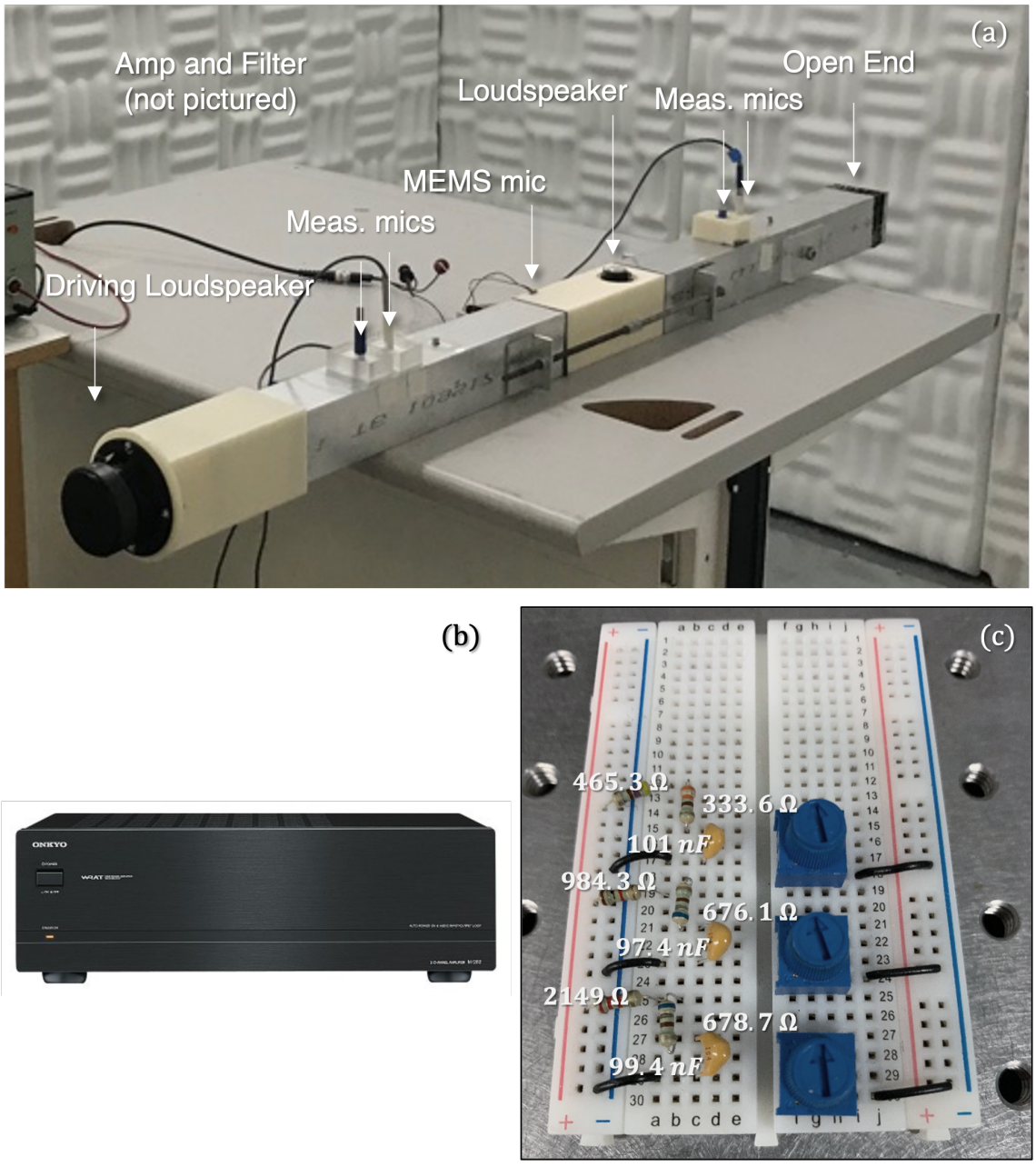

Figure 2.10: Experimental Setup. (a) The experimental waveguide with NAM unit cell holding the MEMS microphone probe and mini loudspeaker source between two aluminum waveguide sections, each with two slots for measurement microphones. The driving loudspeaker could be placed on either end to create disturbances from either direction. (b) The Onkyo audio amplifier used to supply the proportional gain to the MEMS microphone signals. The gain level was fine-tuned by potentiometers on a breadboard since each low-pass filter required a slightly different proportional gain to achieve the high nonreciprocity seen in the data (c). This allowed for repeat experiments of different conditions to be conducted without making any adjustments to the Onkyo amplifier.

gain was required to achieve the desired large nonreciprocity. 10 kOhm potentiometers were placed in series with the audio amplifier and low-pass filters to fine-tune the proportional gain before the signal was transmitted to the loudspeaker source (Fig. 2.10(c)).

Secured on either side of the 3D printed unit cell were two 47 cm long aluminum waveguide sections with cross sectional areas equal to the NAM unit cell. Each section featured two holes to position Larson Davis Model 2520 1/4 inch free-field microphones at a total of four locations. The system was driven by an 8 Ohm Dayton Audio 3 inch loudspeaker (Model DS90-8). This end speaker could be switched to the other end of the waveguide to perform tests in either direction, however it was found that reorienting the active section of our waveguide was simplest. Pressure measurements at four locations along the waveguide were used to measure the transmission across the NAM unit cell. By employing a standard technique [61–63], transmission measurements independent of the waveguide end conditions were obtained.

2.4.3 System Characterization

2.4.3.1 The Loudspeaker Source

Extensive system characterization efforts were needed to obtain the parameters used in the expanded model discussed in Section 2.4.1 to accurately predict experimental results. The electrical and mechanical parameters of source loudspeakers [64–67] were determined through impedance measurements obtained using an Agilent E4980A Precision LCR Meter. To determine M_m and C_m, impedance measurements were collected with the loudspeaker in a vacuum jar to remove any acoustic mass loading on the speaker cone (Fig. 2.11(a)). Proof masses composed of LOCTITE® mounting putty were weighed (Fig. 2.11(b)) and secured to the loudspeaker diaphragm as shown in Fig. 2.11(c). The putty was tacky and required no additional adhesive to remain secured to the loudspeaker. From the shift in resonance frequency resulting from the addition of the putty (along with the known putty mass), M_m and C_m were estimated. the quality factor of the resonance peak and the high

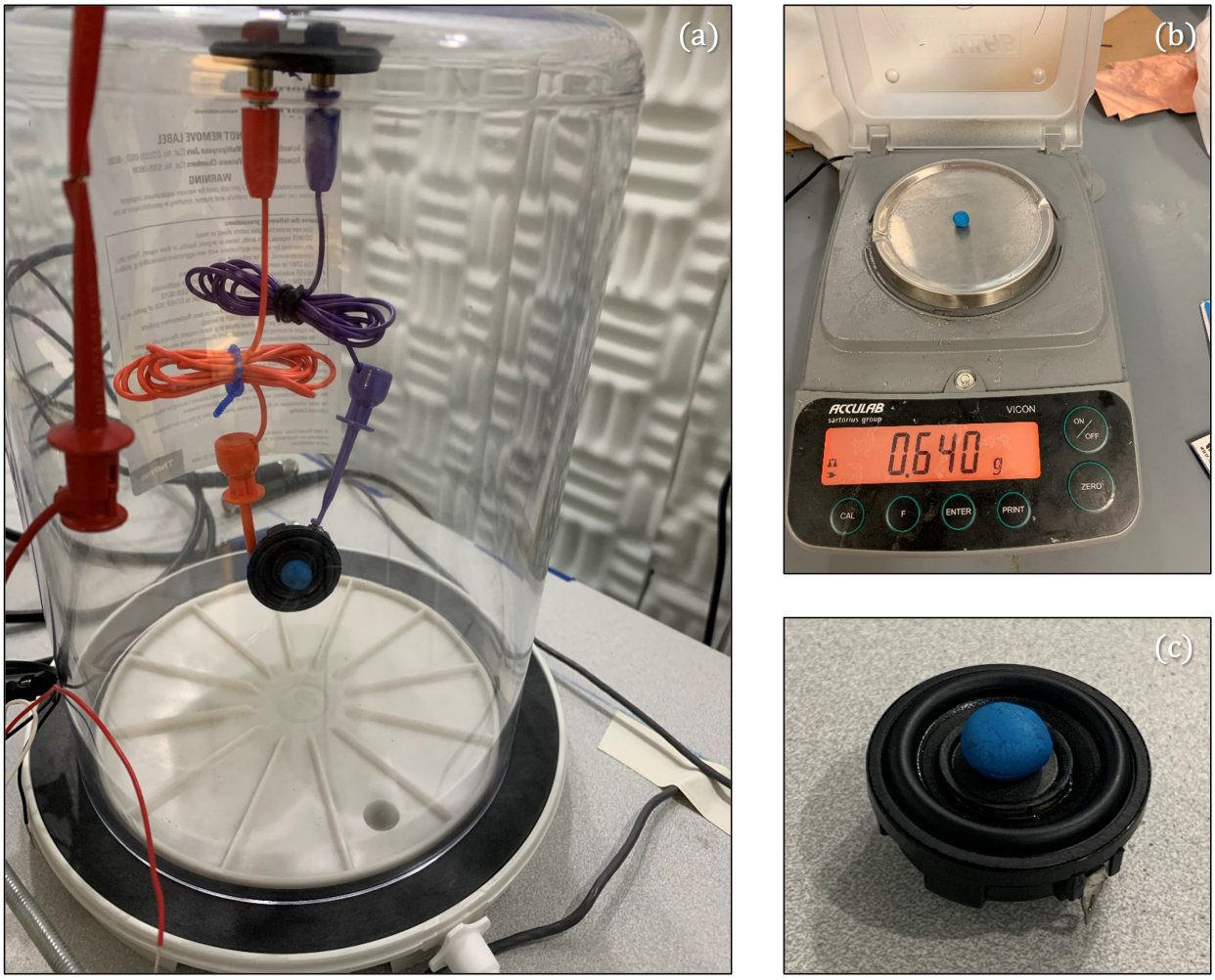

Figure 2.11: Speaker impedance measurement setup. (a) Impedance measurements were collected with the loudspeaker in a vacuum jar to remove effects of acoustic mass loading from the outside air. (b) Proof masses made from mounting putty were weighed before being attached to the speaker diaphragm (c) to shift the resonant peak down in the impedance measurements.

and low frequency asymptotic behavior of the real and imaginary parts of the impedance measurements were used to estimate the remaining parameters.

The real and imaginary parts of one of those measurements are plotted as light dots in Fig. 2.12. Overlaying the data are predictions (solid lines) from the following analytical model [68]:

$$Z_e^{tot} = R_e + \frac{(Bl)^2 R_m}{R_m^2 + (\omega M_m - 1/(\omega C_m))^2} + j\left(\omega L_e - \frac{(Bl)^2(\omega M_m - 1/(\omega C_m))}{R_m^2 + (\omega M_m - 1/(\omega C_m))^2}\right). \quad (2.23)$$

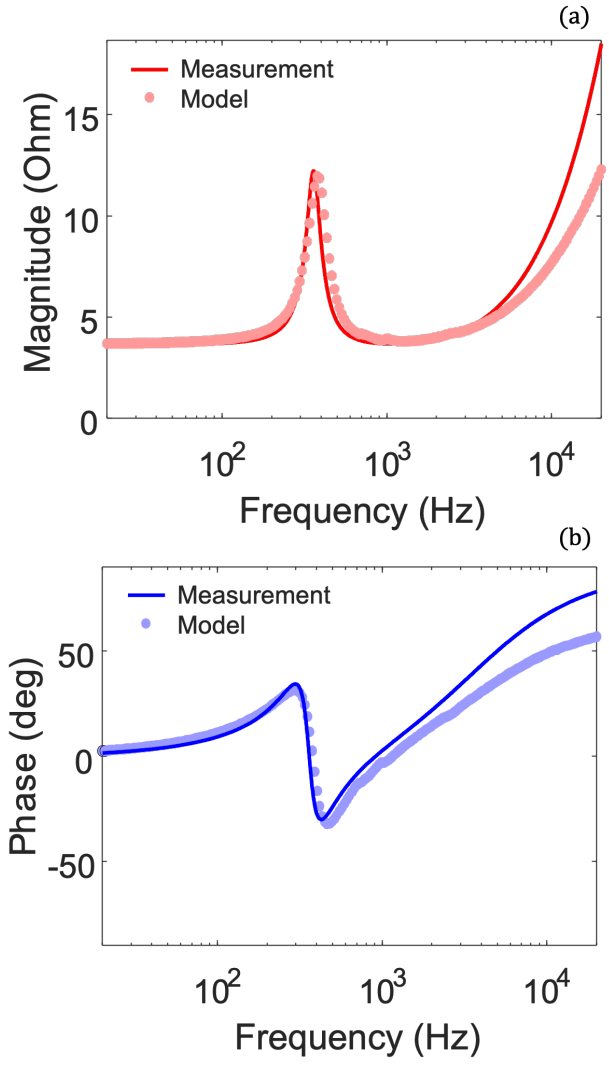

Figure 2.12: Speaker impedance measurement data. The real (imaginary) parts of the impedance measurements are plotted as light red (blue) dots, while the model predictions from Eq. 2.23 overlay the data as solid red (blue) lines. Parameter values used in model predictions are listed in Table 2.1.

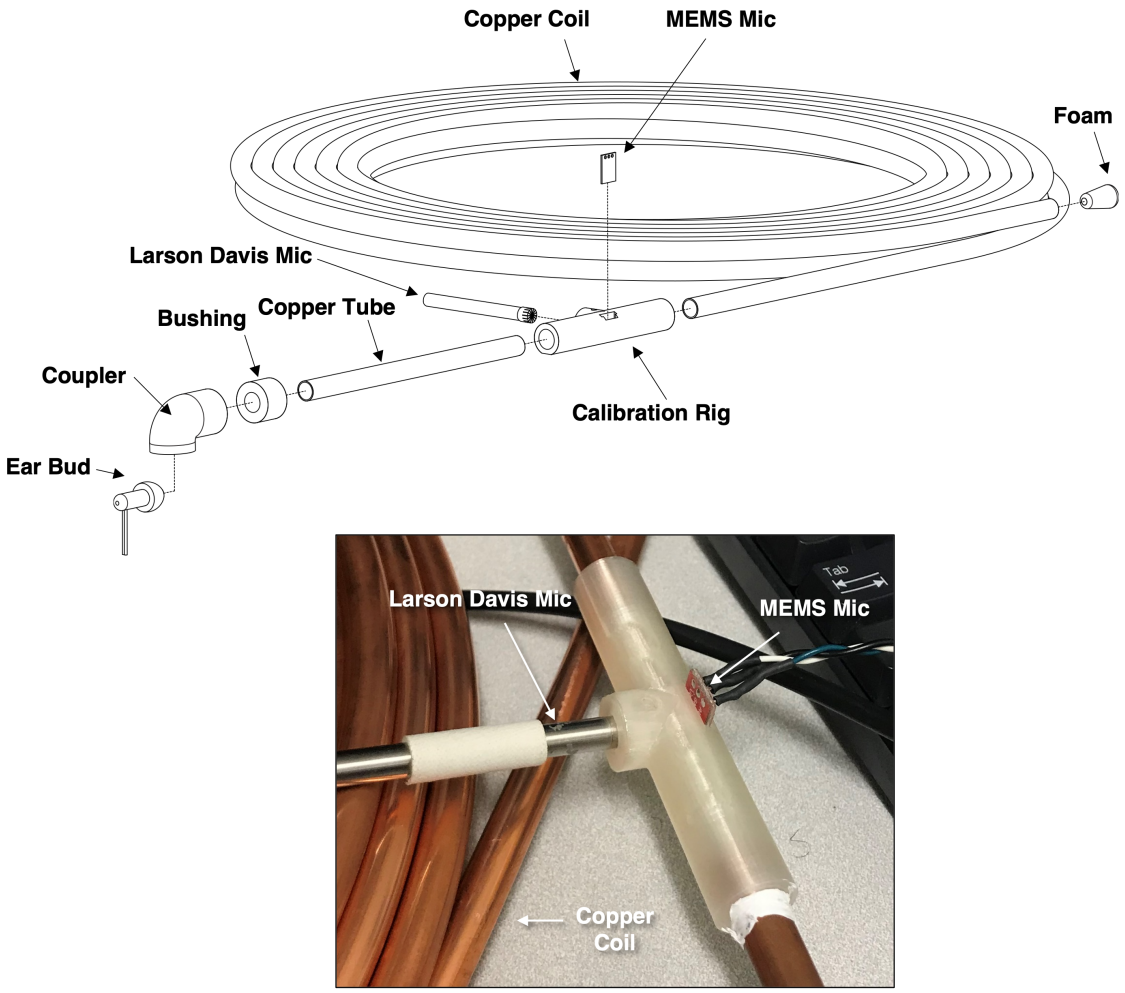

Figure 2.13: MEMS microphone sensitivity measurement rig. MEMS mic sensitivity values were determined using a rig that secured the MEMS mic across from a Larson Davis measurement microphone with known sensitivity. Both microphones faced an interior duct with one port connected to a small earbud used to drive the system and the other connected to a long copper coil to mitigate reflections downstream from the fixture.

2.4.3.2 The MEMS Microphone Probe

The MEMS microphone sensitivity was measured using the custom-built test rig shown in Fig. 2.13. The rig positioned our MEMS microphone across from a well calibrated Larson Davis microphone. The system was driven by an earbud connected to an open port of the rig and the other port was terminated using a long coil of copper tubing to minimize reflections. The driving earbud was incapable of driving the microphones below 400 Hz and the measurements were rejected below this frequency. The MEMS microphone breakout

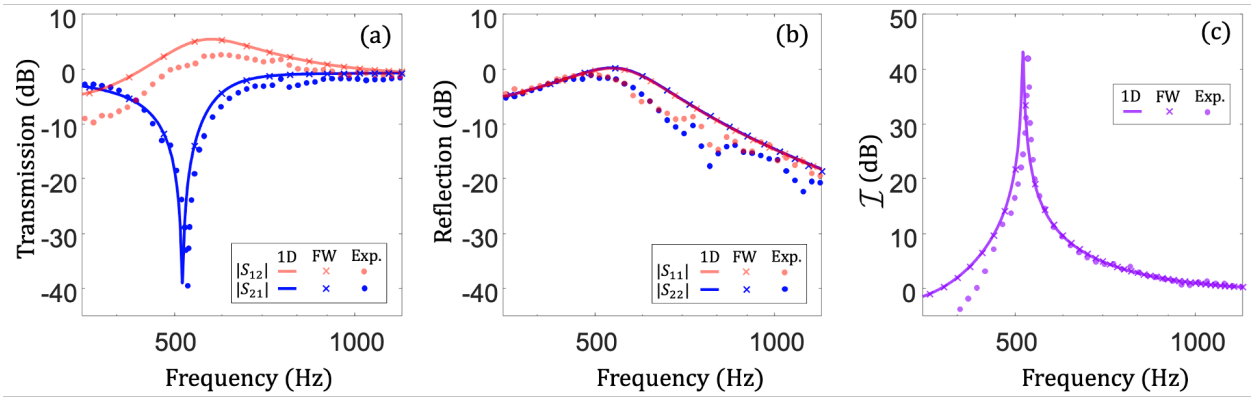

Figure 2.14: Experimental results for the single NAM unit cell. (a) Transmission coefficients measured across our experimental unit cell (dots) show the nonreciprocal nature of the NAM unit cell, which acts as a gain media for waves incident from the right (red) and as a loss media for waves incident from the left (blue), effectively opaque near 525 Hz. (b) Measured reflection coefficients show a bidirectional symmetry in the fully coupled system. (c) The isolation factor peaked at over 40 dB near 525 Hz ($\delta x \approx 0.15\lambda$), with isolation above 10 dB over a third of an octave. There is good agreement between the experimental data, expanded 1D model (solid lines), and FW simulations (x's) with deviations primarily due to loudspeaker impedance measurement variations used to determine the electromechanical characteristics of the loudspeaker source.

board included an inverting amplifier circuit to condition the microphone signal that resulted in a delay which was accounted for in transfer function $H(\omega)$ with a phase shift.

2.4.4 Experimental Results

Experimental results for the NAM unit cell with $H_g = 0.143$ V/Pa and $f_{lp} = 830$ Hz are plotted in Fig. 2.14. The measured transmission coefficients (dots) in Fig. 2.14(a) show a highly nonreciprocal nature similar to that observed in the ideal NAM model (Eq. 2.1). The coupled electromechanical-acoustic response of the NAM unit cell is well represented by both the expanded 1D model (solid lines) and FW models (x's). This demonstrates that the effects of three-dimensionality and the loading of evanescent modes on the source speaker are not dominant. Hence, the 1D structural acoustic model of Eq. 2.19 can be used to select design parameters in a computationally inexpensive way. For waves travelling to the right, the NAM behaves primarily as a loss medium, effectively opaque near 525 Hz ($\delta x \approx 0.15\lambda$), resulting in a remarkable $\mathcal{I}$ peak of over 40 dB (Fig. 2.14(c)). The bidirectional symmetry

of the amplitudes of the reflection coefficients predicted by the ideal NAM model is nearly preserved by experimental data in Fig. 2.14(b). The nonreciprocity of the experimental system is broadband, with $\mathcal{I}$ magnitudes above 10 dB across a third of an octave (from 470 Hz to 600 Hz). Furthermore, the ability to electronically shift the frequencies at which the $\mathcal{I}$ peaks occur was demonstrated experimentally. Fig. 2.15(a) shows isolation factors for the experimental setup with $H_g^+ = 0.140$ V/Pa and $f_{lp}^+ = 1676$ Hz, shifting f_{pk} up to 586 Hz ($\delta x \approx 0.17\lambda$), and with $H_g^- = 0.152$ V/Pa and $f_{lp}^- = 548$ Hz, shifting f_{pk} down to 460 Hz ($\delta x \approx 0.13\lambda$). For both additional peaks, the NAM unit cell remained subwavelength, and the ≈ 40 dB $\mathcal{I}$ magnitudes and relative bandwidths were maintained.

A careful analysis of $\bar{\boldsymbol{S}}$ reveals that real system behavior is strongly linked to both the controller characteristics (H_g and f_{lp}) and the electromechanical characteristics of the loudspeaker. Hence, accurate characterization of the real loudspeaker source is required to select appropriate controller parameters. The relationship between f_{lp} and H_g is shown in Fig. 2.15(b). The value of H_g required to achieve $\mathcal{I}$ peaks exceeding 40 dB for a given f_{lp} is plotted. The relationship between f_{lp} and f_{pk} is shown in Fig. 2.15(c). The frequency at which the $\mathcal{I}$ peak occurs (f_{pk}) for a given f_{lp} is plotted (solid line). Also in Fig. 2.15(c) are the the upper and lower frequencies (dashed lines) between which the $\mathcal{I}$ exceeds 10 dB. For values of f_{lp} bellow 1000 Hz, there is an inverse relationship between H_g and f_{lp}, and H_g is more sensitive to changes in f_{lp} than for values of f_{lp} above 1000 Hz, where H_g begins to increase monotonically with f_{lp}. For all values of f_{lp} shown, the large relative bandwidths are maintained. While we demonstrated experimentally three different frequencies at which the NAM system can generate large, broadband, subwavelength nonreciprocity in Fig. 2.15(a), Fig. 2.15(b) and Fig. 2.15(c) suggest that these frequencies could be chosen arbitrarily over a range of 100 Hz or more.

The remarkable match between model predictions and experimental data shown in this section is a direct result of the extensive system characterization efforts detailed in Section 2.4.3. Included in these parameter measurements were estimates of measurement variation.

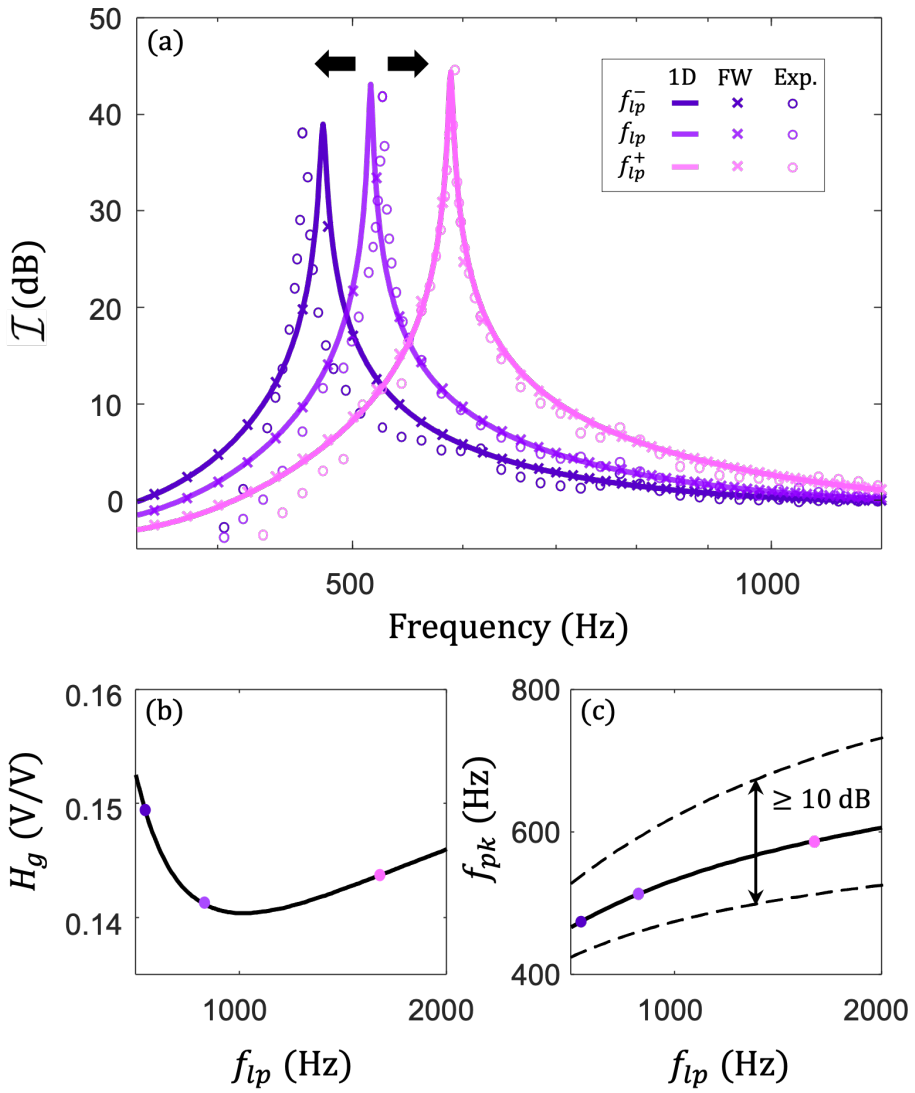

Figure 2.15: Electronic tunability of the NAM system. (a) The remarkable tunable nature predicted by the ideal NAM system could be reproduced experimentally (circles). The peak isolation frequency was shifted up to 586 Hz ($\delta x \approx 0.17\lambda$) by setting $H_g^+ = 0.140$ V/Pa and $f_{lp}^+ = 1676$ Hz, and down to 460 Hz ($\delta x \approx 0.13\lambda$) by setting $H_g^- = 0.152$ V/Pa and $f_{lp}^- = 548$ Hz. Again, there is good agreement between the experimental data (circles), expanded 1D model (solid lines), and FW simulations (x's). (b) Relationship between f_{lp} and H_g. For a given f_{lp}, the value of H_g required to generate a peak above 40 dB is plotted. (c) Relationship between f_{lp} and f_{pk}. For a given f_{lp}, the frequency where the peak occurs, f_{pk}, is plotted (solid line). The upper and lower frequencies (dashed curves) between which $\mathcal{I}$ exceeds 10 dB are also shown. The colored dots in (b) and (c) indicate the values of f_{lp}, H_g, and f_{pk} for their respective colored curves in (a).

We used optimization tools to vary each parameter within their respective ranges to find parameter values that minimized the deviations of model predictions with experiments as

Property	Description	Value
M_m (g)	Diaphragm mass	0.65
C_m (mm/N)	Suspension compliance	0.29
R_m (Nm/s)	Suspension mechanical resistance	0.32
L_e (mH)	Voice coil inductance	0.23
R_e (Ω)	Voice coil DC resistance	3.75
Bl (Tm)	Magnetic field x voice coil length	1.70
S_d (cm^2)	Diaphragm projected area	2.05

Table 2.1: Loudspeaker parameter values. Each parameter in Eq. 2.23 is listed with a description and a value determined by an optimization routine to be the best fit with impedance measurements (Fig. 2.12), controller parameter measurements (Fig. 2.16), and the experimental results shown in this section.

Property	Description	Value
H_g (V/Pa)	Gain for peak at 525 Hz	0.142
f_{lp} (Hz)	Corner freq. for peak at 525 Hz	830
H_g^+ (V/Pa)	Gain for peak at 592 Hz	0.145
f_{lp}^+ (Hz)	Corner freq. for peak at 592 Hz	1660
H_g^- (V/Pa)	Gain for peak at 460 Hz	0.147
f_{lp}^- (Hz)	Corner freq. for peak at 460 Hz	558

Table 2.2: Controller parameter values. Each parameter is listed with a description and a value determined by an optimization routine to be the best fit with impedance measurements, controller parameter measurements, and experimental results. Gains include both the MEMS mic sensitivity and audio amplifier gain. Plots using these values (red) are compared with measurement data (black) in Fig. 2.16.

well as deviations of estimated parameter values from measurements obtained from system characterization testing. The resulting parameter values used in model predictions are listed in Table 2.1 and Table 2.2.

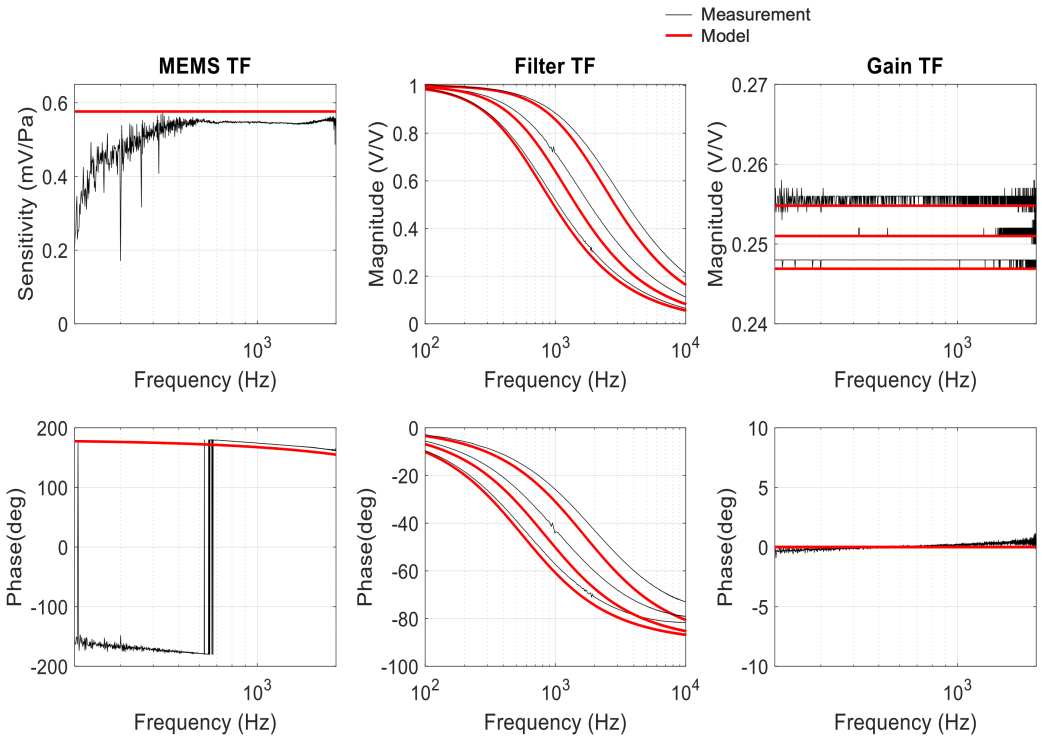

Figure 2.16: Controller parameters measurements. The magnitude and phase of MEMS microphone sensitivity measurements and the gains as measured across the audio amplifier and each potentiometer (together forming the proportional gains H_g, H_g^+, H_g^-) are shown in the first and third columns. The corner frequencies (f_{lp}, f_{lp}^+, f_{lp}^-), were determined from measurements across each low-pass filter (shown in the middle column). Experiemental measurements are shown in thin black lines along with model predictions (thicker red lines) using parameters determined by our optimization routine to be the best fit with impedance measurements (Fig. 2.12), controller parameter measurements (Fig. 2.16), and the experimental results shown in this section. The large deviation in the MEMS measurement magnitudes is due the inability of the earbud used to drive the system below 400 Hz (see Section 2.4.3.2).

2.5 Conclusion

We have experimentally demonstrated large, tunable, broadband nonreciprocity for a subwavelength device using our NAM strategy. We showed that a simple one-dimensional coupled acoustic model can adequately predict the performance and stability of both full-wave simulations and experimental data. In the next chapter, we discuss ways that performance can be further improved in systems with multiple unit cells.

CHAPTER III

Multiple NAM Unit Cells

3.1 Introduction

Following the success in implementing a single NAM unit cell, this chapter discusses the design and construction of NAM systems composed of multiple NAM unit cells. First, the ideal model was extended to include two unit cells, which revealed a complex interaction between individual unit cells, with trade-offs in performance enhancements and stability limitations dictated by individual controller gains and relative cell spacing. Then, as in the previous chapter, we extend the ideal model to include real speaker dynamics and fluid-structure interactions, discussing efforts to optimize the parameters of a real system and considering the extent to which simplifying assumptions in the model, like excluding loudspeaker near-field effects, are valid. Finally, we exhibit the attractive characteristics predicted by our models with experimental data.

3.2 The Two-Cell Ideal System

In moving toward the construction of physical systems with multiple real NAM unit cells, the single ideal NAM unit cell model was extended to include a second cell as shown in Fig. 3.1, with probes and sources located at x_1^p and x_1^s for the first cell and x_2^p and x_2^s for the second cell, respectively. The probe for the second cell is adjacent to the source for the

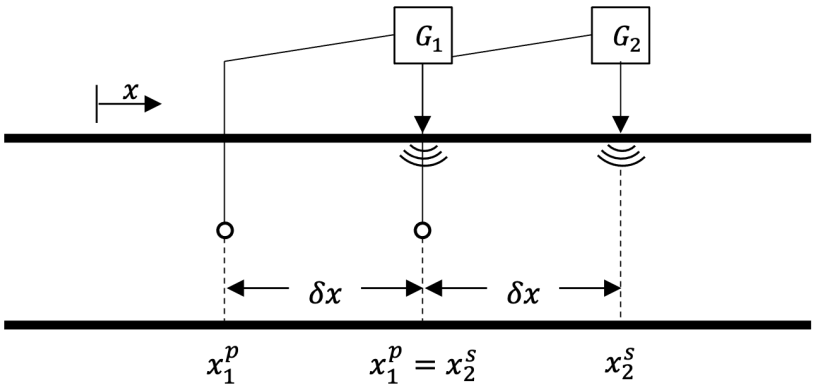

Figure 3.1: Ideal NAM system with two unit cells. The first cell applies a gain G_1 to the signal from the probe at x_1^p and the second cell applies a gain G_2 to the signal the probe at x_2^p. The probe for the second cell is located at the same axial position as the source for the first cell, i.e., $x_1^s = x_2^p$.

first cell (i.e., $x_1^s = x_2^p$). The controllers for the first and second cells apply gains G_1, and G_2, respectively.

3.2.1 The Two-Cell Ideal System With Matching Gains

Using the same method described in Chapter II, the scattering matrix for a system with two ideal cells with identical gains, i.e., $\widetilde{G}_1 = \widetilde{G}_2 = \widetilde{G}$, $\widetilde{G}_i = G_i \delta x$, $i = 1, 2$, denoted by $\boldsymbol{S^{II}}$, is

$$\boldsymbol{S^{II}} = \frac{1}{\widetilde{\Delta}} \begin{bmatrix} -\frac{\widetilde{G}}{jk\delta x}\cos k\delta x & 1 \\ \left(\widetilde{G}\,\mathrm{sinc}\, k\delta x - 1\right)^2 & -\frac{\widetilde{G}}{jk\delta x}\cos k\delta x \end{bmatrix}, \tag{3.1}$$

where

$$\widetilde{\Delta} = 1 + \widetilde{G}\frac{e^{-jk\delta x}}{jk\delta x}, \tag{3.2}$$

By comparing Eq. 3.2 with Eq. 2.10, it can be seen that the stability limit of adjacent cells with equal gains is exactly half the limit for a single cell, i.e., $0 \leq \widetilde{G} < \pi/2$. For $\widetilde{G} = 0.4\pi$, Fig. 3.2 shows the reflection, transmission, and isolation characteristics of a two-cell system (plotted as darker, thicker lines) compared with a one-cell system (plotted as lighter,

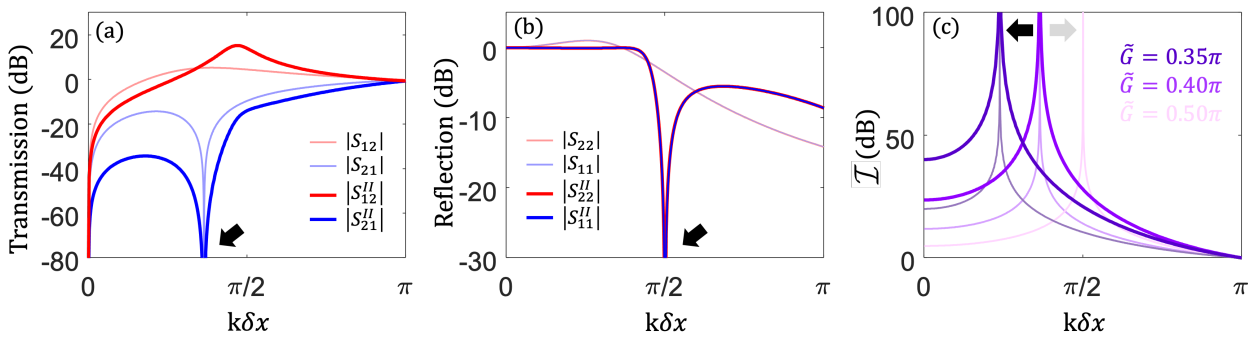

Figure 3.2: Transmission and reflection behavior of the two-cell NAM system (darker, thicker lines) with equal gains for each cell ($\widetilde{G}_1 = \widetilde{G}_2 = 0.4\pi$) compared with a single NAM cell with $\widetilde{G} = 0.4\pi$ (lighter, thinner lines). (a) Directional transmission coefficients show that both systems are highly nonreciprocal, with transmission differences maximized at nulls in transmission of waves propagating to the right. (b) Both systems feature directionally independent reflection coefficients, but for the two-cell system, there exists a null at $k\delta x = \pi/2$. (c) Both systems feature the ability to shift isolation peaks, which occur at the same frequency for a given $\widetilde{G}$. Isolation for the two-cell system is significantly more broadband. However, due to stability limits, isolation levels for $\widetilde{G} = 0.5\pi$ cannot be compared, since $\widetilde{G} = 0.5\pi$ is not stable for the two-cell system.

thinner lines). Directional transmission coefficients (Fig. 3.2(a)) show qualitative similarities between a one-cell and two-cell NAM system, in particular their highly nonreciprocal nature maximized at the null in transmission of waves propagating to the right. Similar to the one-cell system, reflection magnitudes for the two-cell system are directionally independent. However, the reflection coefficients (Fig. 3.2 (b)) for the two-cell system feature a null at $k\delta x = \pi/2$ that represents a frequency where the system is transparent. The diagonal elements of the matrix in Eq. 3.1 show clearly that the system is in fact transparent for any $k\delta x = (2n+1)\pi/2$ ($n \in \mathbb{Z}^+$). While peaks in isolation (Fig. 3.2(c)) for each system occur at the same frequency for a given $\widetilde{G}$, it can be seen that isolation for a two-cell system is significantly more broadband than for a one-cell system, while also preserving the tunable nature of the one-cell system. Limitations include the fact that, due to stability limits, the isolation peak for a two-cell system cannot be shifted as far up in frequency as the one-cell system (Fig. 3.2(c)). Also, the two-cell system is less compact at twice the length of a single cell. Limitations aside, the results shown in Fig. 3.2 illustrate the significant advantages of

a two-cell system over a one-cell system. For a given controller gain, the two-cell system greatly increases the isolation bandwidth while preserving tunability.

3.2.2 The Two-Cell Ideal System With Differing Gains

Further enhancements to the improved performance of a two-cell system with matching gains can be achieved with a slightly more general two-cell system, one in which the condition of identical gains is relaxed. The scattering matrix for a two-cell NAM system with differing gains is

$$\bar{\boldsymbol{S}}^{\boldsymbol{II}} = \frac{1}{\bar{\Delta}} \begin{bmatrix} -\widetilde{G}_1 \frac{e^{jk\delta x}}{2jk\delta x} - \widetilde{G}_2 \frac{e^{-jk\delta x}}{2jk\delta x} & 1 \\ \left(\widetilde{G}_1 \operatorname{sinc} k\delta x - 1\right) \left(\widetilde{G}_2 \operatorname{sinc} k\delta x - 1\right) & -\widetilde{G}_1 \frac{e^{-jk\delta x}}{2jk\delta x} - \widetilde{G}_2 \frac{e^{jk\delta x}}{2jk\delta x} \end{bmatrix}, \tag{3.3}$$

where

$$\bar{\Delta} = 1 + \left(\widetilde{G}_1 + \widetilde{G}_2\right) \frac{e^{-jk\delta x}}{jk\delta x}. \tag{3.4}$$

Fig. 3.3 compares a two-cell system with identical gains $\widetilde{G} = 0.4\pi$ (thinner, lighter lines) with a two-cell system with $\widetilde{G}_1 = 0.4\pi$ and $\widetilde{G}_2 = 0.35\pi$ (thicker, darker lines). While the transmissions of waves propagating to the left, shown in Fig. 3.3(a), are nearly the same for the two systems, the system with differing gains yields an additional null in the transmission to the right, resulting in an additional peak in isolation shown in Fig. 3.3(c). Along with this additional peak comes an even wider isolation bandwidth. Both systems have directionally independent reflection coefficients as can be seen in Fig. 3.3(b), however the the system with differing gains is never totally transparent as it features no nulls in its reflection coefficients. The restricted tunability resulting from the narrower stability ranges seen in a two-cell system with matching gains as compared to a one-cell system can me mitigated in two-cell systems with differing gains. From Eq. 3.4, the range of stability is $0 \leq (\widetilde{G}_1 + \widetilde{G}_2) < \pi$, and hence

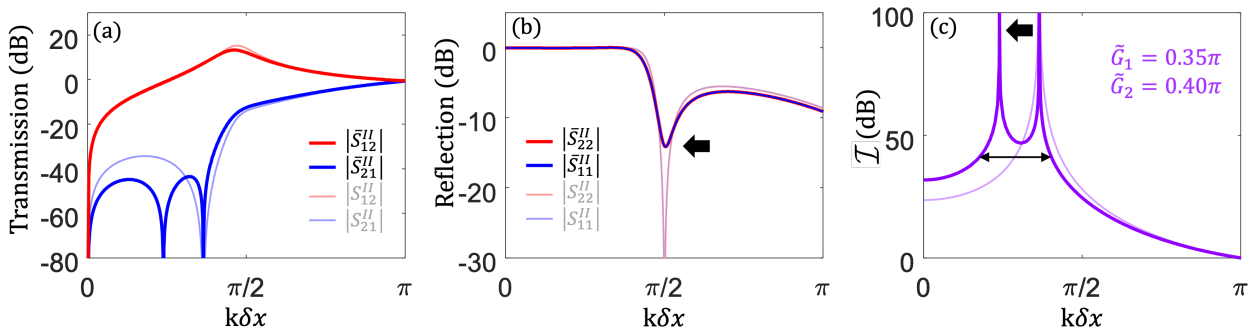

Figure 3.3: Scattering parameters of a two-cell ideal NAM system with gains $\widetilde{G}_1 = 0.4\pi$ and $\widetilde{G}_2 = 0.35\pi$ (thicker, darker lines) compared with a two-cell system with identical gains $\widetilde{G} = 0.4\pi$ (thinner, lighter lines). (a) Directional transmission coefficients show that differing gains can yield an additional null in transmission to the right with minimal effects on the transmission to the left as compared with identical gains. (b) While both systems feature directionally independent reflection coefficients, differing gains result in a loss of the total transparency seen in the system with matching gains. (c) The additional null in (a) yields a second peak in isolation for a two-cell system with differing gains that extends the overall isolation bandwidth.

stability conditions apply to the total sum of the dimensionless gains, rather than on each gain individually. Therefore, rather than a stability range for each gain, the system featured an unbounded stability region for $\widetilde{G}_1$ and $\widetilde{G}_2$. This region is indicated by the shaded area in Fig. 3.4(a). Though stable over the entire region, the expression for S_{21} in Eq. 3.3 requires $\widetilde{G}_1 > 1$ and $\widetilde{G}_2 > 1$ to achieve the two nulls in transmission that yield separate isolation peaks. So, although the region of stability is unbounded, the design space of interest is restricted to the shaded triangular region in Fig. 3.4(b).

Considering the behavior of the ideal system with gains $\widetilde{G}_1 = 0.4\pi$ and $\widetilde{G}_2 = 0.35\pi$, plotted again in Fig. 3.5 as lighter, thinner lines, the stability range shown in Fig. 3.4(b) indicates the reduction in $\widetilde{G}_1$ allows for an increase in $\widetilde{G}_2$. Fig. 3.5 shows the behavior for an ideal two-cell system with gains $\widetilde{G}_2 = 0.5\pi$ (an otherwise unstable gain in a two-cell system with matching gains) and $\widetilde{G}_1 = 0.35\pi$, plotted as thicker, darker lines. Note that the isolation level shown in Fig. 3.5 (c) features a peak up to $k\delta x = \pi/2$ which would not be possible in a two-cell system with matching gains. The advantages of a two-cell system with $\widetilde{G}_1 \neq \widetilde{G}_2$ will be demonstrated with experimental results discussed later in this chapter.

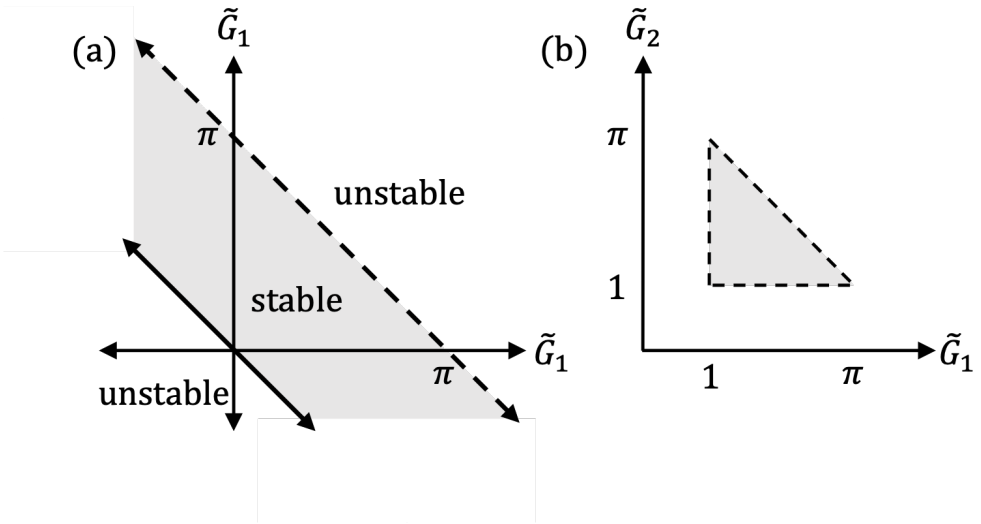

Figure 3.4: Stability characteristics of a two-cell ideal NAM system with differing gains (i.e., $G_1 \neq G_2$). (a) The stability region (shaded) for a two-cell system with differing gains $(0 \leq (\widetilde{G}_1 + \widetilde{G}_2) < \pi)$(b) Design space of interest where combinations of gains yield multiple isolation peaks.

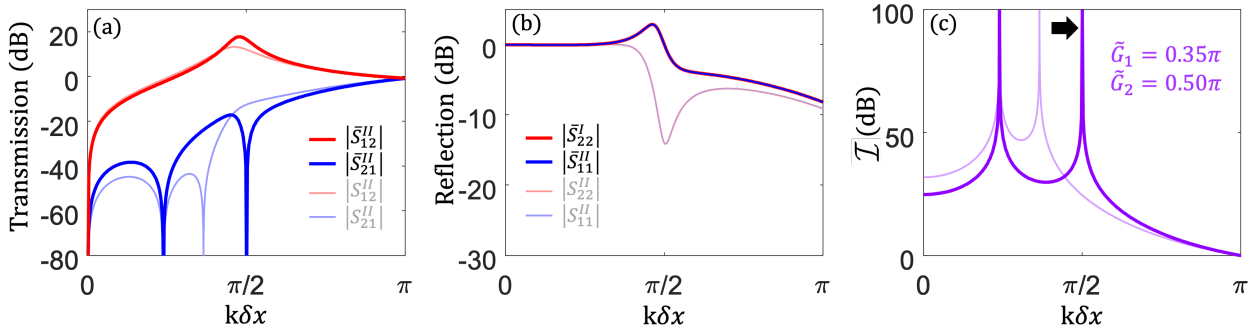

Figure 3.5: Scattering parameters of a two-cell ideal NAM system with gains $\widetilde{G}_1 = 0.4\pi$ and $\widetilde{G}_2 = 0.35\pi$ (thinner, lighter lines) compared with a two-cell system with $\widetilde{G}_1 = 0.4\pi$ and $\widetilde{G}_2 = 0.5\pi$ (thicker, darker lines). (a) Directional transmission coefficients show that increasing $\widetilde{G}_2$ shifts one null in transmission further to the right with minimal effects on the transmission to the left. (b) Again, differing gains result in a loss of the total transparency seen in the system with matching gains. (c) Isolation of a two-cell system with gains $\widetilde{G}_1 = 0.35\pi$ and $\widetilde{G}_2 = 0.5\pi$ features a peak up to $k\delta x = \pi/2$, extending the bandwidth of the isolation for two-cell ideal system with gains $\widetilde{G}_1 = 0.4\pi$ and $\widetilde{G}_2 = 0.35\pi$, which would not be possible in a two-cell system with matching gains.

3.2.3 Relative Cell Spacing in a Two-Cell Ideal System

In the previous sections, we saw that for ideal unit cells, varying the gains of each individual cell had significant implications in terms of both system performance and stability.

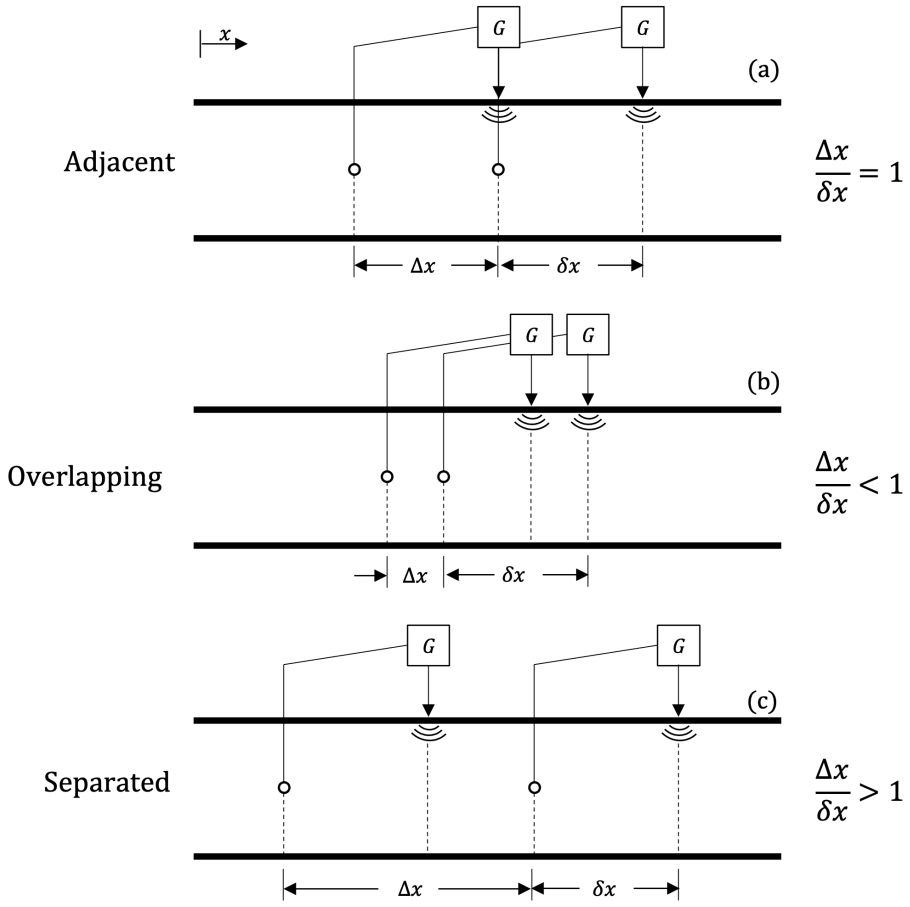

Figure 3.6: Unit cell spacing in a two-cell ideal NAM system. (a) Adjacent unit cells have a ratio $\Delta x/\delta x = 1$ (b) Overlapping unit cells have a ratio $\Delta x/\delta x < 1$ (c) Separated unit cells have a ratio $\Delta x/\delta x > 1$.

Before moving onto the study of a more realistic 1D model with speaker dynamics, we examine another important degree of freedom for the two-cell system, which is the relative spacing between unit cells. As shown in Fig. 3.6, unit cell spacing can be characterized in terms of the value of the ratio $\Delta x/\delta x$, where Δx represents the separation between the first and second probes or the first and second sources, with $\Delta x/\delta x = 1$ for adjacent cells (Fig. 3.6(a)), $\Delta x/\delta x < 1$ for overlapping cells (Fig. 3.6(b)), and $\Delta x/\delta x > 1$ for separated cells. Unfortunately, closed form solutions for the scattering parameters of systems where $\Delta x/\delta x \neq 1$ do not simplify into expressions that offer the same level of insight as did the expressions for $\Delta x/\delta x = 1$, even for the ideal systems without speaker dynamics, and hence the effects of relative cell spacing had to be investigated using analytical model solutions.

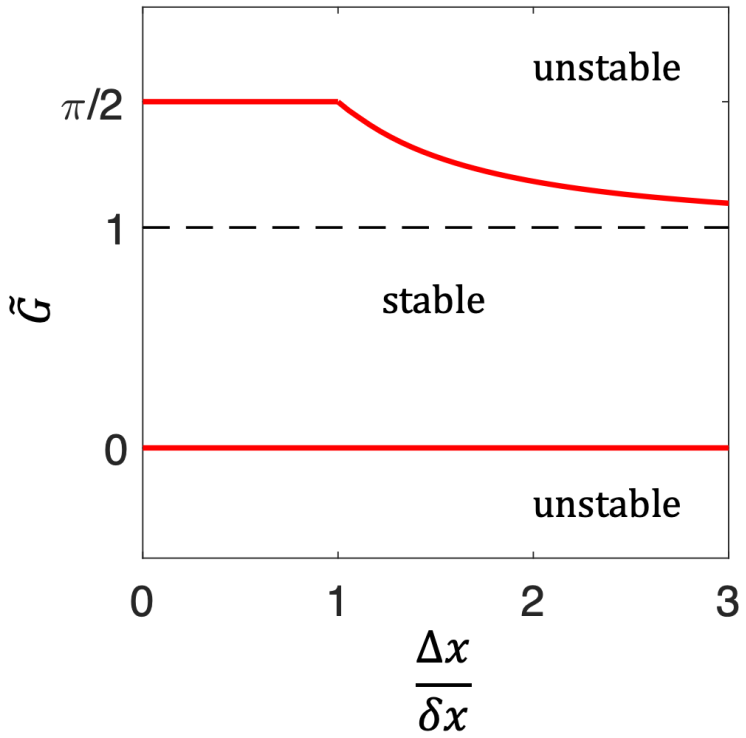

Figure 3.7: Effects of Unit cell spacing on system stability. The upper and lower bounds of G are shown in red. For $0 < \Delta x/\delta x \leq 1$, the maximum stable gain is invariant with changing $\Delta x/\delta x$, equal to $G = \pi/2$. For $\Delta x/\delta x > 1$, the maximum stable gain tapers, yielding narrower stability ranges for G. The dashed line represents the lower bound of the operating range of the system (within which large isolation peaks are possible).

One particularly interesting finding that arose from varying cell spacing in the ideal system model was the effect $\Delta x/\delta x$ had on system stability. For a pair of unit cells with equal gains, G, stability was evaluated using the Nyquist stability criterion (see Section 2.3.2.2). The upper and lower bounds of G are shown in red in Fig. 3.7. For $0 < \Delta x/\delta x \leq 1$, the maximum stable gain is invariant with changing $\Delta x/\delta x$, equal to $G = \pi/2$. For $\Delta x/\delta x > 1$, the maximum stable gain tapers, yielding narrower stability ranges for G. The dashed line in Fig. 3.7 represents the lower bound of the operating range (within which large isolation peaks are possible). Like the stability range, the operating range is also constant for $0 < \Delta x/\delta x \leq 1$ and becomes narrower with increasing $\Delta x/\delta x$ for $\Delta x/\delta x > 1$.

We showed in this section a number of interesting features for an ideal two-cell system,

discussing the effects of changes to the gain and separation distances on system performance and stability. For the single unit cell, we saw that ideal system behavior qualitatively matched real experimental cells, but that it was necessary to expand the ideal model to account for speaker dynamics and fluid-structure interactions. These features are included for a two-cell NAM system in the next section.

3.3 The Two-Cell Systems with Speaker Dynamics

As was shown for the single NAM unit cell, introducing loudspeaker dynamics into the system model reveals that both performance and stability depend on the complicated relationships of the electrical and mechanical properties of the loudspeaker, not only with each other, but with all other system parameters. This complexity is further exacerbated by adding in a second unit cell with a second loudspeaker with its own characteristics. We found that the unit-to-unit variation of the loudspeakers we were using was significant and had to be taken into account in our modeling efforts. Hence, to study the two-cell system with real loudspeakers, we developed a guided user interface (GUI) in MATLAB® to solve the analytical model based on user inputs. The front panel of the GUI, shown in Fig. 3.8, allowed the user to select all relevant system parameters, including the electromechanical characteristics of each speaker, the gain and corner frequencies of each controller, as well as δx and Δx. The system response was also displayed on the front panel, including the reflection and transmission coefficients, the isolation factor (I), and the Nyquist plot of the open-loop transfer function of the system, used to determine system stability. The GUI shown in Fig. 3.8 served as a powerful tool in developing an intuition about important system parameters and for answering questions normally addressed by large-scale sensitivity studies in real time. For example, as in the ideal model, the GUI indicated that changing $\Delta x/\delta x$ in the region where cells overlap had no effect on stability, while stability margins for separated cells (i.e.,$\Delta x/\delta x < 1$), as indicated by the proximity of the Nyquist curve to the point $(-1, 0j)$ (red dot), decreased with increasing $\Delta x/\delta x$ beyond 1. Most importantly, the

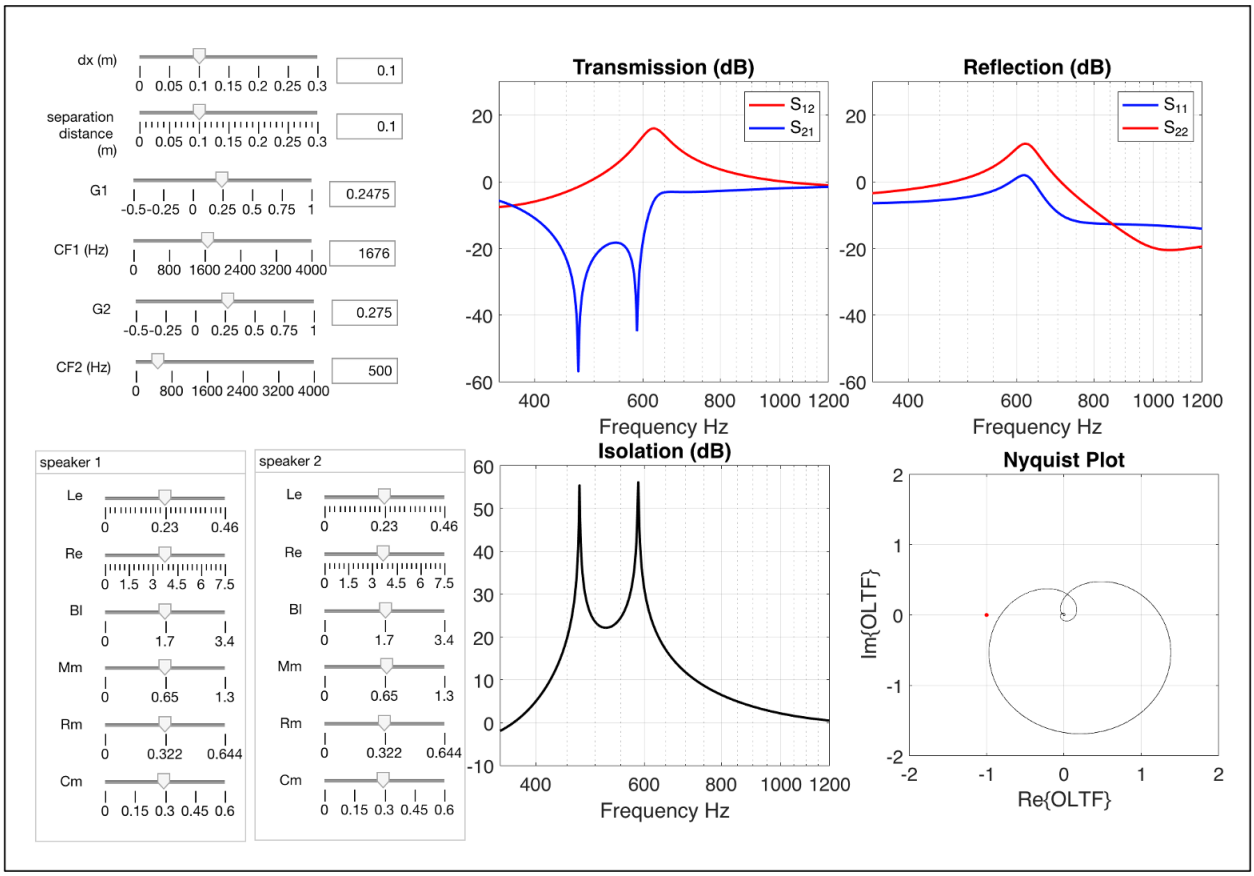

Figure 3.8: The front panel of the guided user interface (GUI) developed to solve the analytical model for a two-cell system with speaker dynamics. The GUI allowed a user to select all relevant system parameters, including the electromechanical characteristics of each speaker, the gain and corner frequencies of each controller, as well as δx and Δx. The system response was also displayed on the front panel, including the reflection and transmission coefficients, the isolation factor, and the Nyquist plot of the open-loop transfer function of the system.

GUI allowed for quickly finding various sets of parameters that resulted in a stable two-cell system with multiple isolation peaks. However, with so many degrees of freedom, we turned to optimization techniques to assist in finding the best system design.

3.3.1 Optimization for Experimental Unit Cell Separation

To determine the optimal design for an experimental two-cell system, we used the nonlinear programming solver, `fmincon`, from the optimization toolbox in MATLAB®, which finds the minimum of a user defined objective function, Z, using optimization methods to vary parameters within a user defined model. An initial verification test is shown in Fig. 3.9.

Model parameters were initially set such that the system scattering characteristics followed the thinner lines. Because we were interested in maximizing the level of nonreciprocity of the system, we were in search of isolation curves with high magnitudes and bandwidths, and hence, we chose the area under the isolation curve over the frequency shown, $\int \mathcal{I}$ as our variable to optimize, yielding the objective function

$$Z = \frac{1}{\int \mathcal{I}}. \tag{3.5}$$

Allowing the solver to only vary the gain of each cell resulted in a solution shown in the thicker lines in Fig. 3.9. Clearly the solver was successful in determining the appropriate gains for each unit cell that maximized nonreciprocity. Although the solution shown yielded a stable system, it was quickly found that this was not always the case, and it was necessary to determine a way to take stability into account. One requirement of Z is that it must be smooth and differentiable, and hence a binary component indicating whether or not the system was stable was not admissible as part of an objective function. However, we noticed that, in general, the peak level in S_{12} was well correlated with the stability margin of the system. An example of this can be seen in Fig. 3.9. Hence, we modified the objective function to include the peak level in S_{12} as

$$Z = \frac{1}{\int \mathcal{I}} + \max |S_{12}|. \tag{3.6}$$

Providing the same initial parameter quantities as before, shown again as thinner lines in Fig. 3.10, allowing the solver to again only vary unit cell gains to minimize Eq. 3.6 yielded the behavior shown in Fig. 3.10 as thicker lines. In this case, the isolation performance was significantly degraded. It is clear that $\max |S_{12}|$ had a greater contribution to Z than did the area under the isolation curve.

The competing objectives in Eq. 3.6 could be managed by introducing the constants ξ_1

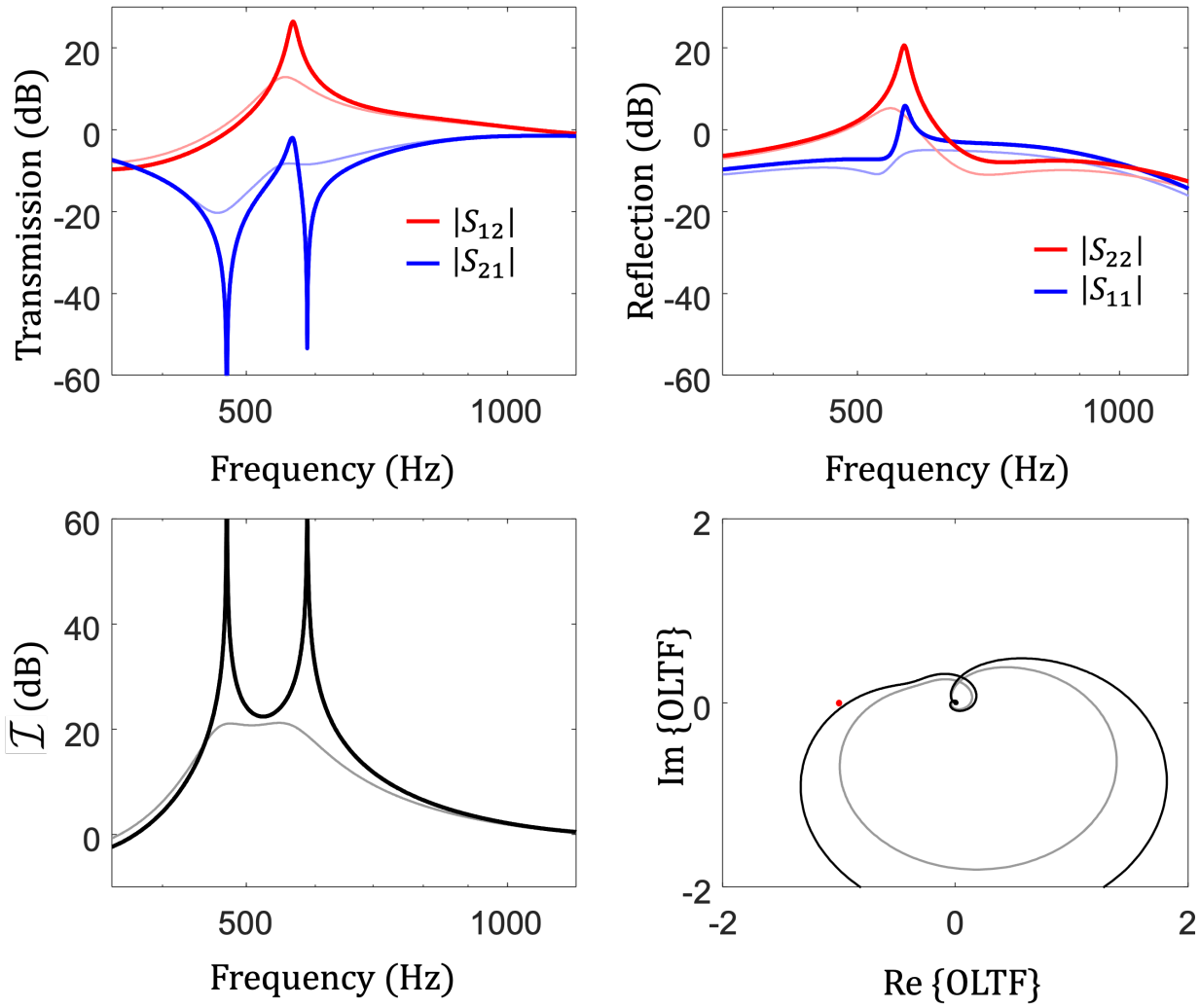

Figure 3.9: Using the nonlinear programming solver, `fmincon`, from the optimization toolbox in MATLAB®, parameters for the two cell model that yielded the results shown as thinner lines, were adjusted by the solver, which was permitted to adjust only the proportional gains of each unit cell. In this case, the solver found parameters that yielded the results shown as thicker lines, which featured large isolation peaks and bandwidths.

and ξ_2 to scale each term in the objective function, i.e.,

$$Z = \xi_1 \frac{1}{\int \mathcal{I}} + \xi_2 \max |S_{12}|, \tag{3.7}$$

which allowed for adjusting the relative influence of each term in the objective function. While it was possible to find solutions with better isolation performance by adjusting these scaling factors, ξ_1 and ξ_2 represent two additional degrees of freedom that must be defined

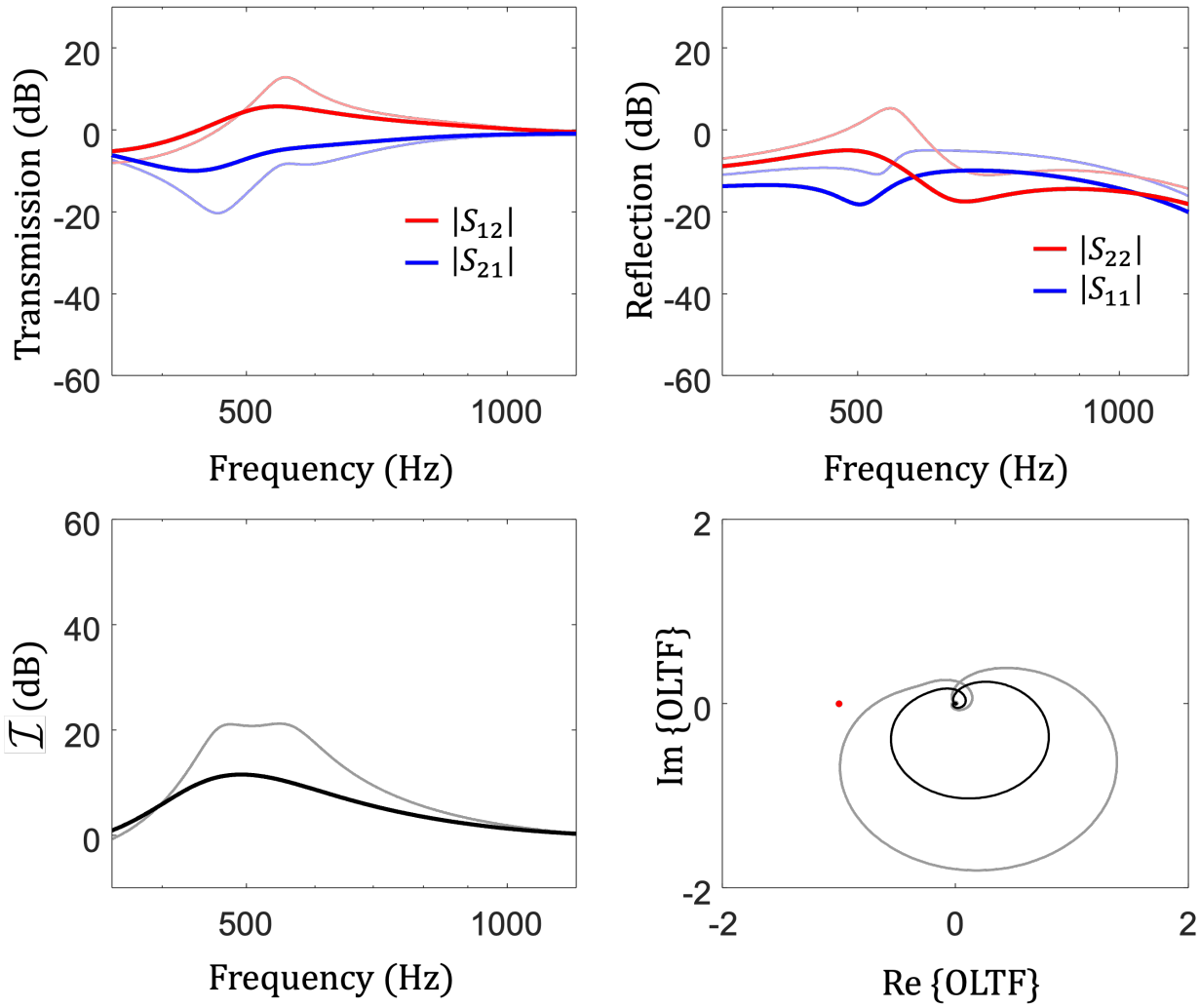

Figure 3.10: Providing the same initial parameter quantities as in Fig. 3.9, shown again here as thinner lines, and allowing the solver to again only vary unit cell gains to minimize Eq. 3.6 yielded the behavior shown in as thicker lines. In this case, the isolation performance was significantly degraded. It is clear that $\max|S_{12}|$ had a greater contribution to Z than did the area under the isolation curve.

for the solver. Furthermore, we found that solver solutions were sensitive not only to initial gain values, but also the ranges of values within which the solver could search for gains. Hence, there was limited confidence in results obtained when the solver was allowed to vary additional controller parameters and cell spacing.

Despite these limitations, one important finding in optimization efforts was that when allowed to adjust δx and Δx, the solver consistently selected values resulting in $\Delta x/\delta x \approx 1$.

Placing the two experimental unit cells presented in Chapter II back to back yielded a separation distance of $\Delta x/\delta x \approx 1.6$, but the proximity of the second microphone to the first speaker led to the concern of near-field loudspeaker effects that have so far been neglected in our models. Hence, because optimization efforts invariably suggested $\Delta x/\delta x \approx 1$ yielded the preferred separation distance between unit cells, the degree to which near-field effects could be neglected in our models is investigated in the next section.

3.3.2 Loudspeaker Near-Field Effects

Since optimization efforts indicated that $\Delta x/\delta x \approx 1$ was the ideal cell separation distance, and since we had the ability to run experiments with two of the experimental unit cells we already had available to us (where $\Delta x/\delta x \approx 1.6$), it became important to determine the extent to which near-field effects from the speaker in the first cell would impact the signal measured by the MEMS microphone in the second cell. Fig. 3.11 shows a full-wave simulation in COMSOL Multiphysics® of the sound pressure level near the speaker for a single unit cell. It is clear that pressure distributions near the loudspeaker were nonuniform and ostensibly would significantly influence measurements collected by a microphone in close proximity. However, as can be seen in Fig. 3.12, near-field effects were minimal. As shown in Fig. 3.12(a), for a two-cell system with $\Delta x/\delta x = 1$, transmission and reflection coefficients predicted by our 1D model with speaker dynamics (solid lines) very precisely match full-wave simulations (x's), with the exception of the transmission from left to right (blue), and consequently the isolation level (black). However, the difference was only a few dB. As shown in Fig. 3.12(b), extending the cell separation distance slightly ($\Delta x/\delta x = 1.6$) resolved the mismatch between 1D model predictions and full-wave simulations. Hence, we expected negligible influence of near-field effects using the experimental setup shown in Fig. 3.13.

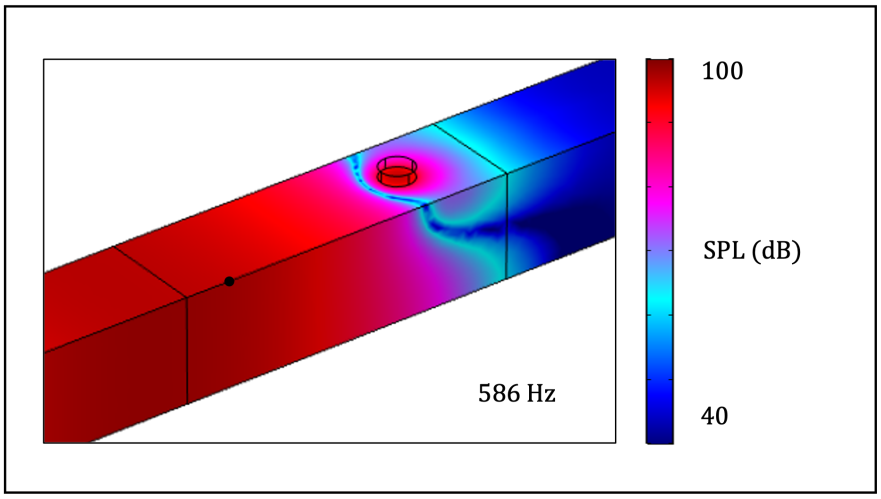

Figure 3.11: Near Field Effects. Full-wave simulation in COMSOL Multiphysics® of the sound pressure level near the speaker for a single unit cell. It's clear that pressure distributions near the loudspeaker were nonuniform and ostensibly would significantly influence measurements collected by a microphone in close proximity.

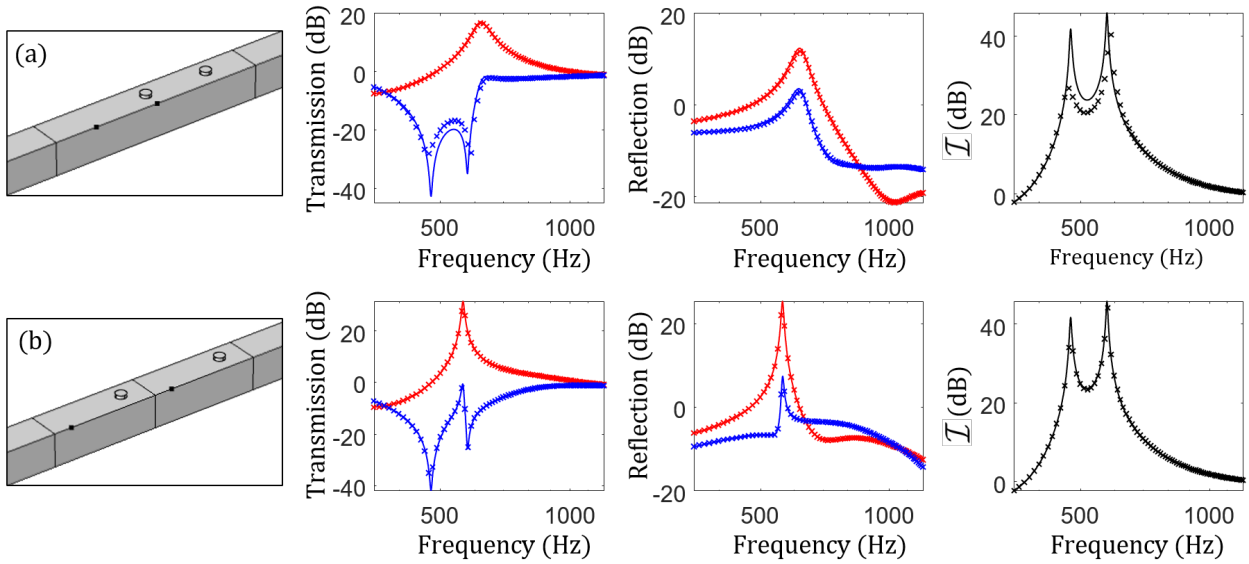

Figure 3.12: Near Field Effects as a function of distance. (a) For a two-cell system with $\Delta x/\delta x = 1$, transmission and reflection coefficients predicted by our 1D model with speaker dynamics (solid lines) very precisely match full-wave simulations (x's), with the exception of the transmission from left to right (blue), and consequently the isolation level (black). However, the difference was only a few dB. (b) Extending the cell separation distance slightly ($\Delta x/\delta x = 1.6$) resolved the mismatch between 1D model predictions and full-wave simulations.

3.4 Experiments with a Real Two-Cell System

3.4.1 Experimental Setup

As stated in the previous section, experiments were conducted in a two-cell system with a separation distance $\Delta x/\delta x = 1.6$. This setup is shown in Fig. 3.13.

3.4.2 Experimental Results

The advantages of adding an additional unit cell to the NAM system predicted by both the ideal and expanded system models also appeared in experimental results. For these experiments, one cell in the system was tuned such that the isolation was centered near 850 Hz, resulting in a peak isolation of 46 dB and a 10 dB bandwidth of a half octave. The other cell in the system was tuned such that the isolation was centered just under 800 Hz, resulting in a peak isolation of 34 dB and a 10 dB bandwidth of 0.4 octaves. Running the system with both cells active resulted in an isolation performance that exceeded each cell on its own in terms of both peak value and bandwidth. For both cells together, we saw a peak in isolation of 50 dB, and a 10 dB bandwidth of 0.8 octaves. These results are shown in Fig. 3.14, with performances for each unit cell shown as lighter lines, and the performance of both cells together as darker lines.

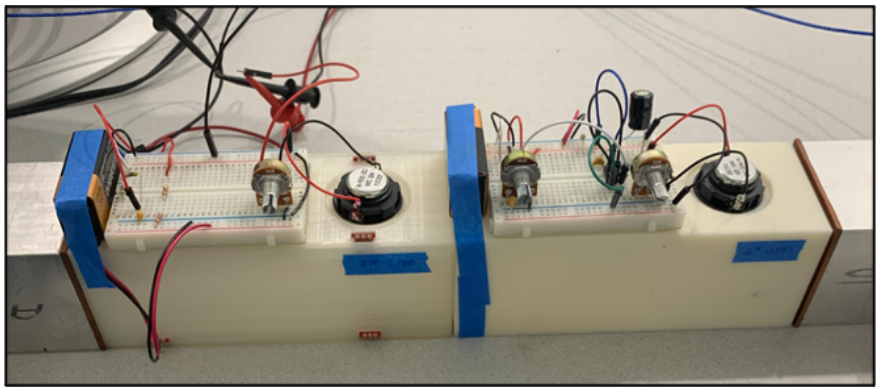

Figure 3.13: Experimental unit cells placed back-to-back resulted in a separation distance $\Delta x/\delta x = 1.6$. This setup allowed us to verify two-cell system performance with existing components, requiring no additional fabrication.

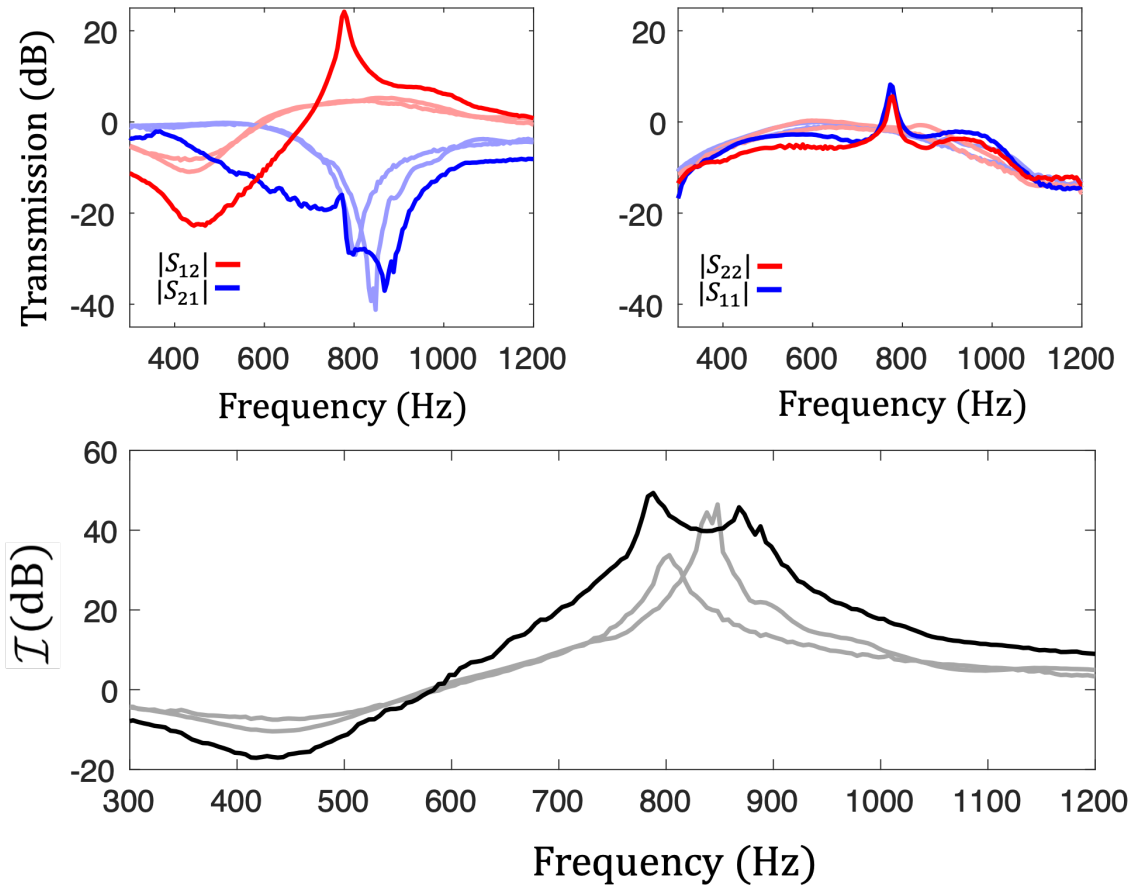

Figure 3.14: Experimental results for a two-cell NAM system. One cell in the system was tuned such that the isolation was centered near 850 Hz, resulting in a peak isolation of 46 dB and a 10 dB bandwidth of a half octave. The other cell in the system was tuned such that the isolation was centered just under 800 Hz,resulting in a peak isolation of 34 dB and a 10 dB bandwidth of 0.4 octaves. Running the system with both cells active resulted in an isolation performance that exceeded each cell on its own in terms of both peak value and bandwidth. For both cells together, we saw a peak in isolation of 50 dB, and a 10 dB bandwidth of 0.8 octaves. Here, performances for each unit cell are shown as lighter lines, and the performance of both cells together are shown as darker lines

As predicted by both the ideal model and models including speaker dynamics, the performance of two experimental cells together significantly outperforms each cell individually. Isolation levels for the two-cell system featured peak magnitudes that exceeded the peak magnitudes for single-cell systems and were far more broadband. Unlike for the single experimental unit cell, we don't compare experimental data directly to model predictions,

which requires the lengthy system characterization efforts described in Chapter II. However, these impressive results show that our models are capable of predicting the behavior of a real two-cell system, and show great promise for extending systems to include larger arrays of unit cells.

3.5 Conclusion

We have demonstrated experimentally the advantages of multiple airborne NAM unit cells. As predicted by both our ideal and enhanced models, isolation levels for a two-cell system exceeded levels for each of its constituent unit cells individually, both in magnitude and bandwidth. We presented a guided user interface that allowed for real-time feedback of the effects of parameter changes on both performance and stability. We showed that while efforts to find optimal system parameters posed some limitations, optimization efforts were effective in determining appropriate unit cell spacing. In the next chapter, we show how the concept of action at a distance used in creating nonreciprocal acoustic systems can be used to break reciprocity in elastodynamic systems.

CHAPTER IV

Nonlocality in Dispersive Systems

4.1 Introduction

A commonly studied structure in metamaterial research is an elastic beam outfitted with piezoelectric patches with circuitry used to modify the local material properties of the beam [69, 70]. Elastic systems coupled with piezoelectric materials have been used to validate a variety of conceptual strategies, which include reducing vibrations [71–73], enhancing flexural wave sensing [74], structural health monitoring [75, 76], and energy harvesting [77–79]. Such system have also been proven capable of breaking reciprocity by way of mechanisms that include the spatio-temporal modulation of material properties [80, 81], the introduction of nonlinearities [82], and Willis coupling [53].

Using a similar system, we show how the concept of action at a distance used in creating nonreciprocal acoustic systems can be used to break reciprocity in elastodynamic systems, but rather than using large arrays of piezoelectric patches, we have considered a system with just two sets of patches (see Fig. 4.1), with one set of patches used as a sensor to transmit a signal through a controller with a transfer function G to a separate set of patches used as an actuator. As in the acoustic NAM systems, we have shown that such a nonlocal coupling can successfully break reciprocity.

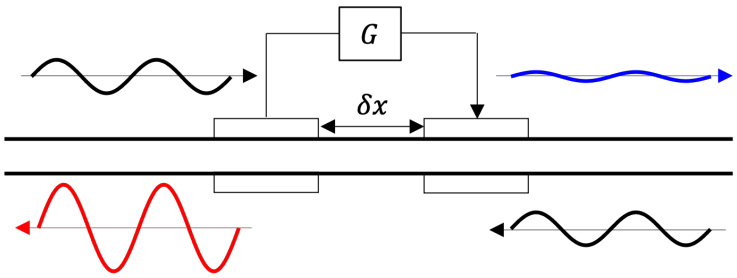

Figure 4.1: Schematic of the nonlocal piezoelectric system in a one-dimensional elastic domain. The right pair of piezoelectric patches are driven by a controller that applies a transfer function G to voltage outputs from the left pair of piezoelectric patches, which are used to sense disturbances upstream a distance δx from the actuating patches. Flexural waves entering the system (black) are either attenuated (blue) or amplified (red) depending on their direction of incidence, indicative of a break in reciprocity.

4.2 System Model

4.2.1 Modified Bernoulli-Euler Beam Theory

The concept of action at a distance to impose a nonlocal coupling in an elastic system is demonstrated using the system diagrammed in Fig. 4.1. The system consists of a slender elastic beam with two pairs of piezoelectric patches, with each pair consisting of a patch adhered to the upper and lower surfaces of the beam. The left pair of patches were used as sensors to convert motion in the beam to a voltage that was sent to a controller that applied a transfer function G to the signal. The signal was then used to drive the second pair of patches which were used as actuators to impose desired deflections of the beam. To model this system, we used a modified Bernoulli-Euler (BE) beam theory that included the piezoelectric properties of the patches attached to the beam [83, 84]. We considered a beam composed of five segments, with each segment alternating between plain segments consisting of elastic material only and layered segments that accounted for the piezoelectric material on the top and bottom of the beam. For each of the plain beam segments, we use the standard BE theory to model the time-harmonic transverse displacements, W, governed by

$$\frac{d^4W(x)}{dx^4} + \beta^4 W(x) = 0, \tag{4.1}$$

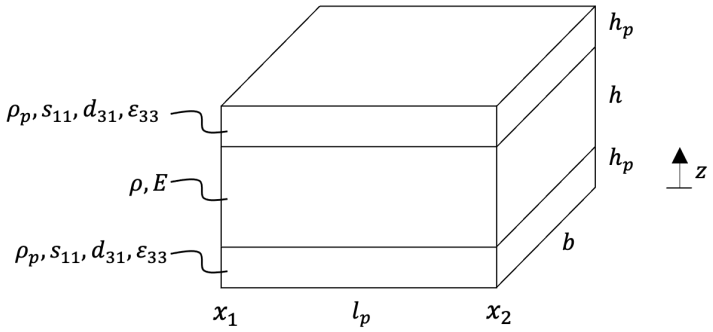

Figure 4.2: Layered segment of beam with length, l_p, and base, b. The top and bottom layers consist of the same piezoelectric material with density, elastic compliance, piezoelectric coefficient, permittivity, and height ρ_p, s_{11}, d_{31}, ε_{33}, and h_p, respectively. The middle layer consists of elastic material with density, stiffness, and height ρ, E, and h, respectively.

with

$$\beta^4 = \frac{\rho A}{EI}\omega^2, \tag{4.2}$$

where ρ, E, A, I, are the density, stiffness, cross-sectional area, and moment of inertia, respectively, and ω is the angular frequency. A layered segment of beam is shown in more detail in Fig. 4.2. Assuming that the piezoelectric material forming the top and bottom layers are identical,the governing equation is

$$\frac{d^4W(x)}{dx^4} + \overline{\beta}^4 W(x) = 0. \tag{4.3}$$

Here, $\overline{\beta}$, can be expressed as

$$\overline{\beta}^4 = \frac{\overline{\rho A}}{\overline{EI}}\omega^2, \tag{4.4}$$

with

$$\overline{EI} = \frac{b\left(\frac{h^2 h_p}{4} + \frac{h h_p^2}{2} + \frac{h_p^3}{3}\right)}{s_{11}}\left(1 + \frac{d_{31}^2}{s_{11}\varepsilon_{33}}\right) + \frac{b\left(\frac{h^2 h_p}{2} + h h_p^2 + \frac{h_p^3}{2}\right)}{s_{11}}\left(1 + \frac{d_{31}^2}{2 s_{11}\varepsilon_{33}}\right), \tag{4.5}$$

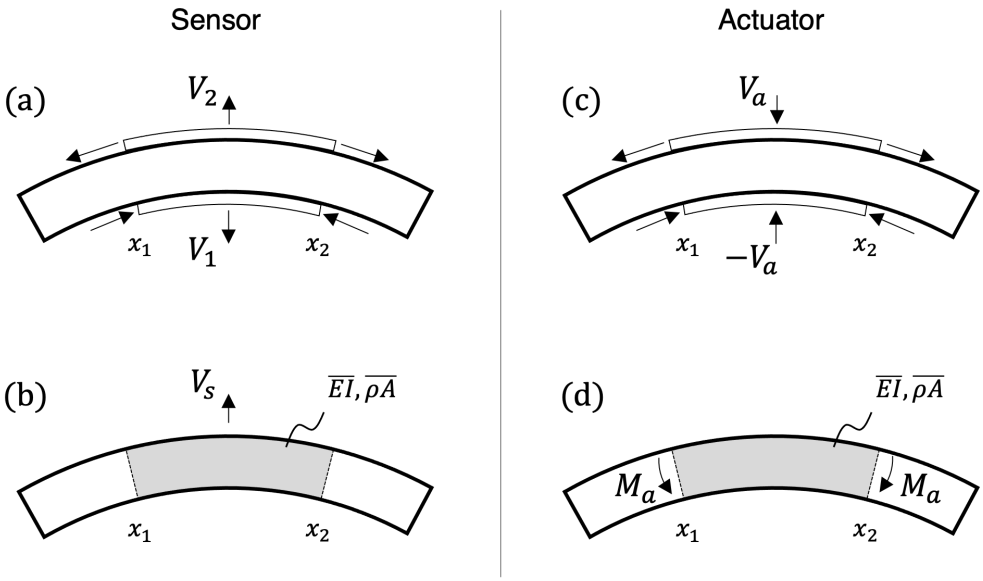

Figure 4.3: Layered segments of beams can be used as sensors or actuators. (a) Bending in the beam causes one patch to bend and contract and the other patch to bend and elongate, resulting in voltages V_1 and V_2, respectively, across the patch electrodes. (b) Using the modified BE theory, the patch segments are replaced with a homogeneous segment of beam with effective properties $\overline{EI}$ and $\overline{\rho A}$ and a total sensed voltage $V_s = V_2 - V_1$. (c) Layered segments can also be used to drive the system by applying a positive actuating voltage V_a across the upper patch, causing it to expand axially, and a negative voltage $-V_a$ across the lower patch, causing it to contract axially. If the upper and lower patches are identical, the axial displacements of each patch will negate one another and result in a pure bending force which can be accounted for in the modified BE theory as point moments, M_a, about the neutral axis of the layered segment, as shown in (d).

$$\overline{\rho A} = b(h\rho + 2h_p\rho_p), \tag{4.6}$$

where the density, elastic compliance, piezoelectric coefficient, permittivity, base, and height of the piezoelectric material are ρ_p, s_{11}, d_{31}, ε_{33}, b, and h_p, respectively, and ρ and h are the density and height, respectively, for the elastic material. Full derivations for $\overline{EI}$ and $\overline{\rho A}$ for more general systems can be found in Krommer [83] and Littrell and Grosh [84].

4.2.2 Piezoelectric Layers as Sensors and Actuators

The layered segments of beam will be used either as a sensor or an actuator [43,53,85–88]. In the sensing case, when layered segments are bent as shown in Fig. 4.3(a), the lower patch

bends and contracts axially, inducing a voltage V_1 across the patch electrodes. The upper patch bends and elongates axially, inducing a voltage V_2. As shown in Fig. 4.3(b), these effects are accounted for in the modified BE theory by replacing the layered segment with a homogeneous segment of material with effective properties $\overline{EI}$ and $\overline{\rho A}$, where the bending of the segment results in a total output voltage V_s, equal to

$$V_s = V_2 - V_1 = \left(\frac{d_{31} h_p (h + h_p)}{s_{11} l_p \left(\varepsilon_{33} - \frac{d_{31}^2}{s_{11}} \right)} \right) \left(\frac{dW(x_2)}{dx} - \frac{dW(x_1)}{dx} \right). \tag{4.7}$$

Although V_1 and V_2 will be a function of both the flexural and longitudinal motion of the piezoelectric materials, due to the symmetry of the system, the longitudinal components of V_1 and V_2 will be out of phase and cancel when summed, and V_s will be a function of the flexural motion through the beam only.

To use a layered segment to drive the system, a prescribed actuating voltage V_a can be applied such that it is positive across the upper patch and negative across the lower patch as shown in Fig. 4.3(c). Driving the patches out of phase in this way will cause one patch to expand axially while the other contracts, yielding longitudinal forces equidistant from the neutral axis of the beam that are equal and opposite. These forces can be accounted for in the modified BE theory with point moments, M_a, about the neutral axis of the beam, where M_a can be expressed as

$$\pm M_a = \mp \overline{EI} \frac{d^2 W(x_i)}{dx^2} \pm \frac{d_{31} h_p (h + h_p)}{s_{11}} V_a, \tag{4.8}$$

with $i = 1, 2$, where $i = 1$ and $i = 2$ indicate the upper and lower signs in $\pm$ and $\mp$, respectively. This is illustrated in Fig. 4.3(d).

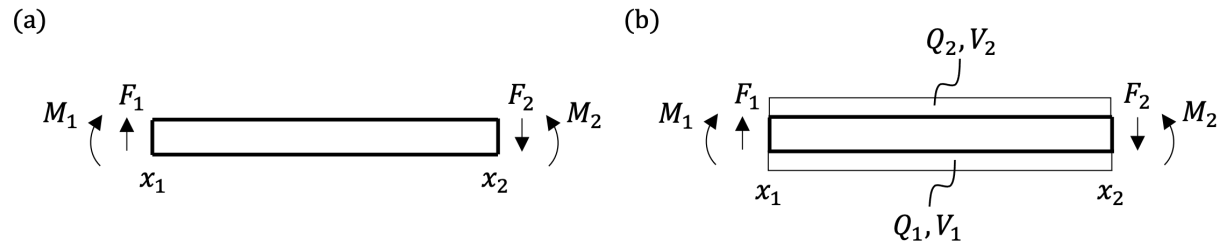

Figure 4.4: Plain (a) and layered (b) segments of beam extending from x_1 to x_2. The forces and moments at either end of each segment can be formulated in terms of the displacements and slopes at their respective ends using the general solutions for the displacements in each segment. For layered segments, expressions for the charges and voltages in the top and bottom layers are also determined.

4.2.3 Model Solution Approach

To model the behavior of the system shown in Fig. 4.1, we adapted techniques from finite element methods (FEM), expanding upon an approach known as the *direct stiffness method* [89], but rather than using arbitrary displacement functions (also called shape functions) for individual elements, we formulate local stiffness matrices in terms of the exact solutions to Eq. 4.1 and Eq. 4.3 [90–93]. For the plain beam segments, shown in Fig. 4.4(a), the solutions $W(x)$ to Eq. 4.1 have the form

$$W(x) = A_1 e^{-j\beta x} + A_2 e^{j\beta x} + A_3 e^{-\beta x} + A_4 e^{\beta x}, \tag{4.9}$$

which can be interpreted physically as travelling waves that propagate in either direction through the segment of beam and evanescent waves that grow and decay in either direction, all with a wavenumber β and arbitrary coefficients A_i, $i = 1, 2, 3, 4$. The displacements and

slopes, D and T, and forces and moments, F and M can be expressed in terms of W as

$$\begin{aligned} D_i &= W(x_i), \\ T_i &= \frac{dW(x_i)}{dx}, \\ F_i &= \pm EI\frac{d^3W(x_i)}{dx^3}, \\ M_i &= \mp EI\frac{d^2W(x_i)}{dx^2}, \end{aligned} \tag{4.10}$$

for $i = 1, 2$, where $i = 1$ and $i = 2$ indicate the upper and lower signs in $\pm$ and $\mp$, respectively. Using Eq. 4.9 and Eq. 4.10, forces and moments at either end can be expressed in terms of displacements and slopes as

$$\begin{bmatrix} F_1 \\ M_1 \\ F_2 \\ M_2 \end{bmatrix} = \begin{bmatrix} P_{11} & P_{12} & P_{13} & P_{14} \\ P_{21} & P_{22} & P_{23} & P_{24} \\ P_{31} & P_{32} & P_{33} & P_{34} \\ P_{41} & P_{42} & P_{43} & P_{44} \end{bmatrix} . \begin{bmatrix} D_1 \\ T_1 \\ D_2 \\ T_2 \end{bmatrix} . \tag{4.11}$$

The matrix elements $P_{i,j}$ were not expressed explicitly, but rather computed in MATLAB®. For the layered beam segments, shown in Fig. 4.4(b), the solutions $\overline{W}(x)$ to Eq. 4.3 have the form

$$\overline{W}(x) = \overline{A}_1 e^{-j\overline{\beta}x} + \overline{A}_2 e^{j\overline{\beta}x} + \overline{A}_3 e^{-\overline{\beta}x} + \overline{A}_4 e^{\overline{\beta}x}, \tag{4.12}$$

where $\overline{\beta}$ is the wavenumber and $\overline{A}_i$, $i = 1, 2, 3, 4$, are the arbitrary magnitudes for waves in the layered segment. In addition to displacements, slopes, forces, and moments, the charges

and voltages, Q and V, in the layered segment can be expressed in terms of $\overline{W}$ as

$$\begin{aligned} D_i &= \overline{W}(x_i), \\ T_i &= \frac{d\overline{W}(x_i)}{dx}, \\ F_i &= \pm\overline{EI}\frac{d^3\overline{W}(x_i)}{dx^3}, \\ M_i &= \mp\overline{EI}\frac{d^2\overline{W}(x_i)}{dx^2} + \alpha(V_1 + V_2), \\ Q_i &= C_p V_i + \alpha(T_1 - T_2), \end{aligned} \tag{4.13}$$

for $i = 1, 2$, where

$$\alpha = \frac{d_{31} b (h + h_p)}{2 s_{11}} \tag{4.14}$$

and the patch capacitance, C_p, is

$$C_p = \left(\varepsilon_{33} + \frac{d_{31}^2}{s_{11}}\right)\frac{b l_p}{h_p}. \tag{4.15}$$

Again, $i = 1$ and $i = 2$ indicate the upper and lower signs in $\pm$ and $\mp$, respectively. Using an approach similar to the approach used to formulate Eq. 4.11, using Eq. 4.12 and Eq. 4.13, forces and moments at either end of the layered segment and charges for the upper and lower piezoelectric layers can be expressed in terms of displacements, slopes, and voltages as

$$\begin{bmatrix} F_1 \\ M_1 \\ Q_1 \\ Q_2 \\ F_2 \\ M_2 \end{bmatrix} = \begin{bmatrix} L_{11} & L_{12} & 0 & 0 & L_{15} & L_{16} \\ L_{21} & L_{22} & \alpha & \alpha & L_{25} & L_{26} \\ 0 & \alpha & C_p & 0 & 0 & -\alpha \\ 0 & \alpha & 0 & C_p & 0 & -\alpha \\ L_{51} & L_{52} & 0 & 0 & L_{55} & L_{56} \\ L_{61} & L_{62} & 0 & 0 & L_{65} & L_{65} \end{bmatrix} \cdot \begin{bmatrix} D_1 \\ T_1 \\ V_1 \\ V_2 \\ D_2 \\ T_2 \end{bmatrix}. \tag{4.16}$$

Again, the matrix elements $L_{i,j}$ were not expressed explicitly, but rather computed in MATLAB®. To our knowledge, we are the first to include properties of the piezoelectric material in the direct stiffness matrix for a layered segment. Formulating the problem in this way allows for a straightforward means of assembling matrices for systems composed of any number of beam segments, either plain or layered, since continuity conditions must be satisfied where segments meet. For example, joining the two segments shown in Fig. 4.4 requires that D_2, T_2, F_2, and M_2 for the plain segment are equivalent to D_1, T_1, F_1, and M_1 for the layered segment, resulting in a matrix of equations that can be formed by combining Eq. 4.11 and Eq. 4.16, yielding

$$\begin{bmatrix} F_1 \\ M_1 \\ F_2 \\ M_2 \\ Q_1 \\ Q_2 \\ F_3 \\ M_3 \end{bmatrix} = \begin{bmatrix} P_{11} & P_{12} & P_{13} & P_{14} & 0 & 0 & 0 & 0 \\ P_{21} & P_{22} & P_{23} & P_{24} & 0 & 0 & 0 & 0 \\ P_{31} & P_{32} & (P_{33}+L_{11}) & (P_{34}+L_{12}) & 0 & 0 & L_{15} & L_{16} \\ P_{41} & P_{42} & (P_{43}+L_{21}) & (P_{44}+L_{22}) & 0 & 0 & L_{25} & L_{26} \\ 0 & 0 & 0 & \alpha & C_p & 0 & 0 & -\alpha \\ 0 & 0 & 0 & \alpha & 0 & C_p & 0 & -\alpha \\ 0 & 0 & L_{51} & L_{52} & 0 & 0 & L_{55} & L_{56} \\ 0 & 0 & L_{61} & L_{62} & 0 & 0 & L_{65} & L_{65} \end{bmatrix} \cdot \begin{bmatrix} D_1 \\ T_1 \\ D_2 \\ T_2 \\ V_1 \\ V_2 \\ D_3 \\ T_3 \end{bmatrix}. \quad (4.17)$$

Following this same approach, the matrix of equations for a system with five segments takes the form shown in Fig. 4.5, where superscripts in parentheses indicate the segment associated with each term, and expressions for α and C_p are shown in Eq. 4.14 and Eq. 4.15, respectively. To model the action at a distance that gives rise to highly nonreciprocal behavior, we impose the condition that

$$(V_3 + V_4) = G(V_1 + V_2), \quad (4.18)$$

$$
\begin{bmatrix} F_1 \\ M_1 \\ F_2 \\ M_2 \\ Q_1 \\ Q_2 \\ F_3 \\ M_3 \\ F_4 \\ M_4 \\ Q_3 \\ Q_4 \\ F_5 \\ M_5 \\ F_6 \\ M_6 \end{bmatrix}
=
\begin{bmatrix}
P_{11}^{(1)} & P_{12}^{(1)} & P_{13}^{(1)} & P_{14}^{(1)} & 0 & 0 & 0 & 0 & 0 & 0 & 0 & 0 & 0 & 0 & 0 & 0 \\
P_{21}^{(1)} & P_{22}^{(1)} & P_{23}^{(1)} & P_{24}^{(1)} & 0 & 0 & 0 & 0 & 0 & 0 & 0 & 0 & 0 & 0 & 0 & 0 \\
P_{31}^{(1)} & P_{32}^{(1)} & P_{33}^{(1)} + L_{11}^{(2)} & P_{34}^{(1)} + L_{12}^{(2)} & 0 & 0 & L_{15}^{(2)} & L_{16}^{(2)} & 0 & 0 & 0 & 0 & 0 & 0 & 0 & 0 \\
P_{41}^{(1)} & P_{42}^{(1)} & P_{43}^{(1)} + L_{21}^{(2)} & P_{44}^{(1)} + L_{22}^{(2)} & \alpha & \alpha & L_{25}^{(2)} & L_{26}^{(2)} & 0 & 0 & 0 & 0 & 0 & 0 & 0 & 0 \\
0 & 0 & 0 & \alpha & C_p & 0 & 0 & -\alpha & 0 & 0 & 0 & 0 & 0 & 0 & 0 & 0 \\
0 & 0 & 0 & \alpha & 0 & C_p & 0 & -\alpha & 0 & 0 & 0 & 0 & 0 & 0 & 0 & 0 \\
0 & 0 & L_{51}^{(2)} & L_{52}^{(2)} & 0 & 0 & L_{55}^{(2)} + P_{11}^{(3)} & L_{56}^{(2)} + P_{12}^{(3)} & P_{13}^{(3)} & P_{14}^{(3)} & 0 & 0 & 0 & 0 & 0 & 0 \\
0 & 0 & L_{61}^{(2)} & L_{62}^{(2)} & 0 & 0 & L_{65}^{(2)} + P_{21}^{(3)} & L_{66}^{(2)} + P_{22}^{(3)} & P_{23}^{(3)} & P_{24}^{(3)} & 0 & 0 & 0 & 0 & 0 & 0 \\
0 & 0 & 0 & 0 & 0 & 0 & P_{31}^{(3)} & P_{32}^{(3)} & P_{33}^{(3)} + L_{11}^{(4)} & P_{34}^{(3)} + L_{12}^{(4)} & 0 & 0 & L_{15}^{(4)} & L_{16}^{(4)} & 0 & 0 \\
0 & 0 & 0 & 0 & 0 & 0 & P_{41}^{(3)} & P_{42}^{(3)} & P_{43}^{(3)} + L_{21}^{(4)} & P_{44}^{(3)} + L_{22}^{(4)} & \alpha & \alpha & L_{25}^{(4)} & L_{26}^{(4)} & 0 & 0 \\
0 & 0 & 0 & \alpha & C_p & 0 & 0 & 0 & 0 & \alpha & C_p & 0 & 0 & -\alpha & 0 & 0 \\
0 & 0 & 0 & \alpha & 0 & C_p & 0 & 0 & 0 & \alpha & 0 & C_p & 0 & -\alpha & 0 & 0 \\
0 & 0 & 0 & 0 & 0 & 0 & L_{55}^{(4)} + P_{11}^{(5)} & L_{56}^{(4)} + P_{12}^{(5)} & L_{51}^{(4)} & L_{52}^{(4)} & 0 & 0 & P_{13}^{(5)} & P_{14}^{(5)} & 0 & 0 \\
0 & 0 & 0 & 0 & 0 & 0 & L_{65}^{(4)} + P_{21}^{(5)} & L_{66}^{(4)} + P_{22}^{(5)} & L_{61}^{(4)} & L_{62}^{(4)} & 0 & 0 & P_{23}^{(5)} & P_{24}^{(5)} & 0 & 0 \\
0 & 0 & 0 & 0 & 0 & 0 & P_{31}^{(5)} & P_{32}^{(5)} & 0 & 0 & 0 & 0 & P_{33}^{(5)} & P_{34}^{(5)} & 0 & 0 \\
0 & 0 & 0 & 0 & 0 & 0 & P_{41}^{(5)} & P_{42}^{(5)} & 0 & 0 & 0 & 0 & P_{43}^{(5)} & P_{44}^{(5)} & 0 & 0
\end{bmatrix}
\begin{bmatrix} D_1 \\ T_1 \\ D_2 \\ T_2 \\ V_1 \\ V_2 \\ D_3 \\ T_3 \\ D_4 \\ T_4 \\ V_3 \\ V_4 \\ D_5 \\ T_5 \\ D_6 \\ T_6 \end{bmatrix}
$$

Figure 4.5: Matrix of equations for a beam with five segments. $P_{i,j}^{(k)}$ and $L_{i,j}^{(k)}$ are the elements of the matrices in Eq. 4.11 and Eq. 4.16, respectively, for the k^{th} beam segment. Expressions for α and C_p are shown in Eq. 4.14 and Eq. 4.15, respectively.

requiring modification to the matrix in Fig. 4.5, which can be seen in red in the ninth and tenth rows of the matrices in Fig. 4.6 and Fig. 4.7. We also sought to impose non-reflecting boundary conditions at either end of the beam, since the extent to which reciprocity is broken is often quantified in 1D systems by computing the ratio of waves transmitted through the system in either direction, and hence radiation boundary conditions are typically imposed so that disturbances downstream from a system of interest only depend on waves transmitted through the system and not on reflected waves from boundary conditions that arise in finite-dimensional systems. To impose radiation boundary conditions [94–97], two additional semi-infinite segments of beam can be added at either end of the five segment beam. For the additional segment on the right end of the beam, the displacement field, $W_{+\infty}(x)$ can be written as

$$W_{+\infty}(x) = A_{+\infty}e^{-j\beta x} + B_{+\infty}e^{-\beta x}, \tag{4.19}$$

where the first term represents a wave traveling to the right with arbitrary coefficient $A_{+\infty}$ and the second term represents an evanescent wave with arbitrary coefficient $B_{+\infty}$ that decays to zero as $x \to +\infty$. Note that compared with Eq. 4.9, the term with a positive complex exponent, representing a wave traveling to a left, is omitted since the boundary is reflectionless. Also omitted is the term with the positive real exponent since the term would not converge as $x \to +\infty$. The same logic can be applied to formulate the displacement field, $W_{-\infty}(x)$ of the semi-infinite plain beam segment added to the left end of the system, expressed as

$$W_{-\infty}(x) = A_{-\infty}e^{j\beta x} + B_{-\infty}e^{\beta x} \tag{4.20}$$

where the first term represents a wave traveling to the left with arbitrary coefficient $A_{-\infty}$ and the second term represents an evanescent wave with arbitrary coefficient $B_{-\infty}$ that decays to zero as $x \to -\infty$. Substituting Eq. 4.19 and Eq. 4.20 into Eq. 4.10, forces and moments

can be expressed in terms of displacements and slopes at either end of the system as

$$\begin{bmatrix} F_1 \\ M_1 \end{bmatrix} = EI \begin{bmatrix} -\beta^3(1-j) & -\beta^2 \\ -\beta^2 & \beta(1+j) \end{bmatrix} . \begin{bmatrix} D_1 \\ T_1 \end{bmatrix}, \tag{4.21}$$

$$\begin{bmatrix} F_6 \\ M_6 \end{bmatrix} = EI \begin{bmatrix} -\beta^3(1-j) & \beta^2 \\ \beta^2 & \beta(1+j) \end{bmatrix} . \begin{bmatrix} D_6 \\ T_6 \end{bmatrix}. \tag{4.22}$$

The modifications to the matrix in Fig. 4.5 using Eq. 4.21 and Eq. 4.22 can be seen in red in the upper left and lower right four elements of the matrices in Fig. 4.6 and Fig. 4.7, where

$$\begin{bmatrix} \widetilde{P}_{11}^{(1)} & \widetilde{P}_{12}^{(1)} \\ \widetilde{P}_{21}^{(1)} & \widetilde{P}_{22}^{(1)} \end{bmatrix} = EI \begin{bmatrix} -\beta^3(1-j) & -\beta^2 \\ -\beta^2 & \beta(1+j) \end{bmatrix} + \begin{bmatrix} P_{11}^{(1)} & P_{12}^{(1)} \\ P_{21}^{(1)} & P_{22}^{(1)} \end{bmatrix}, \tag{4.23}$$

$$\begin{bmatrix} \widetilde{P}_{33}^{(5)} & \widetilde{P}_{34}^{(5)} \\ \widetilde{P}_{43}^{(5)} & \widetilde{P}_{44}^{(5)} \end{bmatrix} = EI \begin{bmatrix} -\beta^3(1-j) & \beta^2 \\ \beta^2 & \beta(1+j) \end{bmatrix} + \begin{bmatrix} P_{33}^{(5)} & P_{34}^{(5)} \\ P_{43}^{(5)} & P_{44}^{(5)} \end{bmatrix}. \tag{4.24}$$

We seek to drive the system with incident travelling flexural waves in either the positive-x or negative-x directions to determine transmission levels through the system, which will consist of the ratio of displacement magnitudes downstream from the system with respect to the incident magnitude. To impose this condition, an incident wave traveling to the right with a known magnitude A_+ can be added to Eq. 4.20, yielding

$$W_{-\infty}(x) = A_{-\infty}e^{j\beta x} + B_{-\infty}e^{\beta x} + A_+e^{-j\beta x}. \tag{4.25}$$

Substituting Eq. 4.25 into Eq. 4.10, the forcing effects of the incident wave can be accounted for in terms of an effective force and moment at the left end of the beam, expressed as

$$\begin{bmatrix} \widetilde{F}_1 \\ \widetilde{M}_1 \end{bmatrix} = EI \begin{bmatrix} -\beta^3(1-j) & -\beta^2 \\ -\beta^2 & \beta(1+j) \end{bmatrix} . \begin{bmatrix} A_+e^{-j\beta x_1} \\ -j\beta A_+e^{-j\beta x_1} \end{bmatrix} + EI \begin{bmatrix} j\beta^3 A_+e^{-j\beta x_1} \\ \beta^2 A_+e^{-j\beta x_1} \end{bmatrix} \tag{4.26}$$

$$
\begin{bmatrix} \widetilde{F}_1 \\ \widetilde{M}_1 \\ 0 \\ 0 \\ 0 \\ 0 \\ 0 \\ 0 \\ 0 \\ 0 \\ 0 \\ 0 \\ 0 \\ 0 \\ 0 \\ 0 \end{bmatrix}
=
\begin{bmatrix}
\widetilde{P}^{(1)}_{11} & \widetilde{P}^{(1)}_{12} & P^{(1)}_{13} & P^{(1)}_{14} & 0 & 0 & 0 & 0 & 0 & 0 & 0 & 0 & 0 & 0 & 0 & 0 \\
\widetilde{P}^{(1)}_{21} & \widetilde{P}^{(1)}_{22} & P^{(1)}_{23} & P^{(1)}_{24} & 0 & 0 & 0 & 0 & 0 & 0 & 0 & 0 & 0 & 0 & 0 & 0 \\
P^{(1)}_{31} & P^{(1)}_{32} & P^{(1)}_{33}+L^{(2)}_{11} & P^{(1)}_{34}+L^{(2)}_{12} & 0 & 0 & L^{(2)}_{15} & L^{(2)}_{16} & 0 & 0 & 0 & 0 & 0 & 0 & 0 & 0 \\
P^{(1)}_{41} & P^{(1)}_{42} & P^{(1)}_{43}+L^{(2)}_{21} & P^{(1)}_{44}+L^{(2)}_{22} & \alpha & \alpha & L^{(2)}_{25} & L^{(2)}_{26} & 0 & 0 & 0 & 0 & 0 & 0 & 0 & 0 \\
0 & 0 & 0 & \alpha & C_p & 0 & 0 & -\alpha & 0 & 0 & 0 & 0 & 0 & 0 & 0 & 0 \\
0 & 0 & 0 & \alpha & 0 & C_p & 0 & -\alpha & 0 & 0 & 0 & 0 & 0 & 0 & 0 & 0 \\
0 & 0 & L^{(2)}_{51} & L^{(2)}_{52} & 0 & 0 & L^{(2)}_{55}+P^{(3)}_{11} & L^{(2)}_{56}+P^{(3)}_{12} & P^{(3)}_{13} & P^{(3)}_{14} & 0 & 0 & 0 & 0 & 0 & 0 \\
0 & 0 & L^{(2)}_{61} & L^{(2)}_{62} & 0 & 0 & L^{(2)}_{65}+P^{(3)}_{21} & L^{(2)}_{66}+P^{(3)}_{22} & P^{(3)}_{23} & P^{(3)}_{24} & 0 & 0 & 0 & 0 & 0 & 0 \\
0 & 0 & 0 & 0 & 0 & 0 & P^{(3)}_{31} & P^{(3)}_{32} & P^{(3)}_{33}+L^{(4)}_{11} & P^{(3)}_{34}+L^{(4)}_{12} & 0 & 0 & L^{(4)}_{15} & L^{(4)}_{16} & 0 & 0 \\
0 & 0 & 0 & 0 & 0 & 0 & P^{(3)}_{41} & P^{(3)}_{42} & P^{(3)}_{43}+L^{(4)}_{21} & P^{(3)}_{44}+L^{(4)}_{22} & \alpha & \alpha & L^{(4)}_{25} & L^{(4)}_{26} & 0 & 0 \\
0 & 0 & 0 & 0 & G & -G & 0 & 0 & 0 & 0 & 0 & 1 & 0 & 0 & 0 & 0 \\
0 & 0 & 0 & 0 & G & -G & 0 & 0 & 0 & 0 & 0 & 0 & -1 & 0 & 0 & 0 \\
0 & 0 & 0 & 0 & 0 & 0 & 0 & 0 & L^{(4)}_{51} & L^{(4)}_{52} & 0 & 0 & L^{(4)}_{55}+P^{(5)}_{11} & L^{(4)}_{56}+P^{(5)}_{12} & P^{(5)}_{13} & P^{(5)}_{14} \\
0 & 0 & 0 & 0 & 0 & 0 & 0 & 0 & L^{(4)}_{61} & L^{(4)}_{62} & 0 & 0 & L^{(4)}_{65}+P^{(5)}_{21} & L^{(4)}_{66}+P^{(5)}_{22} & P^{(5)}_{23} & P^{(5)}_{24} \\
0 & 0 & 0 & 0 & 0 & 0 & 0 & 0 & 0 & 0 & 0 & 0 & P^{(5)}_{31} & P^{(5)}_{32} & \widetilde{P}^{(5)}_{33} & \widetilde{P}^{(5)}_{34} \\
0 & 0 & 0 & 0 & 0 & 0 & 0 & 0 & 0 & 0 & 0 & 0 & P^{(5)}_{41} & P^{(5)}_{42} & \widetilde{P}^{(5)}_{43} & \widetilde{P}^{(5)}_{44}
\end{bmatrix}
\cdot
\begin{bmatrix} D_1 \\ T_1 \\ D_2 \\ T_2 \\ V_1 \\ V_2 \\ D_3 \\ T_3 \\ D_4 \\ T_4 \\ V_3 \\ V_4 \\ D_5 \\ T_5 \\ D_6 \\ T_6 \end{bmatrix}
$$

Figure 4.6: Modifications to the matrix of equations shown in Fig. 4.5, including action at a distance as defined in Eq. 4.18, shown in red in the ninth and tenth rows, radiation boundary conditions as defined in Eq. 4.23 and Eq. 4.24, seen in red in the upper-left four and bottom-right four elements, and the effects of a left-traveling incident flexural wave of known magnitude A_+ as defined in Eq. 4.26, shown as $\widetilde{F}_1$ and $\widetilde{M}_1$ in red.

$$
\begin{bmatrix}
\widetilde{P}_{11}^{(1)} & \widetilde{P}_{12}^{(1)} & P_{13}^{(1)} & P_{14}^{(1)} & 0 & 0 & 0 & 0 & 0 & 0 & 0 & 0 \\
\widetilde{P}_{21}^{(1)} & \widetilde{P}_{22}^{(1)} & P_{23}^{(1)} & P_{24}^{(1)} & 0 & 0 & 0 & 0 & 0 & 0 & 0 & 0 \\
P_{31}^{(1)} & P_{32}^{(1)} & P_{33}^{(1)} + L_{11}^{(2)} & P_{34}^{(1)} + L_{12}^{(2)} & 0 & 0 & L_{15}^{(2)} & L_{16}^{(2)} & 0 & 0 & 0 & 0 \\
P_{41}^{(1)} & P_{42}^{(1)} & P_{43}^{(1)} + L_{21}^{(2)} & P_{44}^{(1)} + L_{22}^{(2)} & \alpha & 0 & L_{25}^{(2)} & L_{26}^{(2)} & 0 & 0 & 0 & 0 \\
0 & 0 & 0 & \alpha & C_p & 0 & 0 & -\alpha & 0 & 0 & 0 & 0 \\
0 & 0 & 0 & \alpha & 0 & C_p & 0 & -\alpha & 0 & 0 & 0 & 0 \\
0 & 0 & L_{51}^{(2)} & L_{52}^{(2)} & 0 & 0 & L_{55}^{(2)} + P_{11}^{(3)} & L_{56}^{(2)} + P_{12}^{(3)} & P_{13}^{(3)} & P_{14}^{(3)} & 0 & 0 \\
0 & 0 & L_{61}^{(2)} & L_{62}^{(2)} & 0 & 0 & L_{65}^{(2)} + P_{21}^{(3)} & L_{66}^{(2)} + P_{22}^{(3)} & P_{23}^{(3)} & P_{24}^{(3)} & 0 & 0 \\
0 & 0 & 0 & 0 & 0 & 0 & P_{31}^{(3)} & P_{32}^{(3)} & P_{33}^{(3)} + L_{11}^{(4)} & P_{34}^{(3)} + L_{12}^{(4)} & 0 & 0 \\
0 & 0 & 0 & 0 & 0 & 0 & P_{41}^{(3)} & P_{42}^{(3)} & P_{43}^{(3)} + L_{21}^{(4)} & P_{44}^{(3)} + L_{22}^{(4)} & \alpha & 0 \\
0 & 0 & 0 & 0 & G & -G & 0 & 0 & 0 & 0 & 0 & 1 \\
0 & 0 & 0 & 0 & G & -G & 0 & 0 & 0 & 0 & 0 & 0 \\
0 & 0 & 0 & 0 & 0 & 0 & 0 & 0 & L_{51}^{(4)} & L_{52}^{(4)} & 0 & 0 \\
0 & 0 & 0 & 0 & 0 & 0 & 0 & 0 & L_{61}^{(4)} & L_{62}^{(4)} & 0 & 0 \\
0 & 0 & 0 & 0 & 0 & 0 & 0 & 0 & 0 & 0 & 0 & 0 \\
0 & 0 & 0 & 0 & 0 & 0 & 0 & 0 & 0 & 0 & 0 & 0
\end{bmatrix}
\cdot
\begin{bmatrix}
D_1 \\ T_1 \\ D_2 \\ T_2 \\ V_1 \\ V_2 \\ D_3 \\ T_3 \\ D_4 \\ T_4 \\ V_3 \\ V_4 \\ D_5 \\ T_5 \\ D_6 \\ T_6
\end{bmatrix}
=
\begin{bmatrix}
0 \\ 0 \\ 0 \\ 0 \\ 0 \\ 0 \\ 0 \\ 0 \\ 0 \\ 0 \\ 0 \\ 0 \\ 0 \\ 0 \\ \widetilde{F}_6 \\ \widetilde{M}_6
\end{bmatrix}
$$

Figure 4.7: Modifications to the matrix of equations shown in Fig. 4.5, including action at a distance as defined in Eq. 4.18, shown in red in the ninth and tenth rows, radiation boundary conditions as defined in Eq. 4.23 and Eq. 4.24, seen in red in the upper-left four and bottom-right four elements, and the effects of a right-traveling incident flexural wave of known magnitude A_- as defined in Eq. 4.27, shown as $\widetilde{F}_6$ and $\widetilde{M}_6$ in red.

The forcing terms $\widetilde{F}_1$ and $\widetilde{M}_1$ can be seen in Fig. 4.6. Similarly, for left-traveling incident waves with a known magnitude A_-, $\widetilde{F}_6$ and $\widetilde{M}_6$ can be expressed as

$$\begin{bmatrix} \widetilde{F}_6 \\ \widetilde{M}_6 \end{bmatrix} = EI \begin{bmatrix} -\beta^3(1-j) & \beta^2 \\ \beta^2 & \beta(1+j) \end{bmatrix} . \begin{bmatrix} A_- e^{j\beta x_6} \\ j\beta A_- e^{j\beta x_6} \end{bmatrix} + EI \begin{bmatrix} j\beta^3 A_- e^{-j\beta x_6} \\ \beta^2 A_- e^{-j\beta x_6} \end{bmatrix} \tag{4.27}$$

as shown in Fig. 4.7. Formulating the problem as shown in Fig. 4.6 and Fig. 4.7 allows for determining the transmission through the system in either direction. We define the transmission of right-traveling incident waves as

$$T_{(+)} = \frac{A_{+\infty}}{A_+}, \tag{4.28}$$

and the transmission of left-traveling incident waves as

$$T_{(-)} = \frac{A_{-\infty}}{A_-}. \tag{4.29}$$

We quantify the level of nonreciprocity by defining the isolation, $\mathcal{I}$, as the ratio of the magnitudes $|T_{(-)}|$ and $|T_{(+)}|$ in the decibel scale as

$$\mathcal{I} = 20 \log_{10} \left(\left| \frac{T_{(-)}}{T_{(+)}} \right| \right). \tag{4.30}$$

4.2.4 Controller Design

So far, the transfer function of the controller shown in Fig. 4.1 has been represented by the singular quantity G. To use our modelling approach to predict experimental data, we anticipated needing a controller that could accommodate the characteristics of the real PZT-4 patches we intended to function as the piezoelectric layers in the model. Due to the high capacitance values of the PZT-4 patches, we needed to first send the signals from the sensing patches through a buffer circuit before being conditioned further. We also planned to use a high voltage amplifier specifically designed for piezoelectric materials to drive the actuating

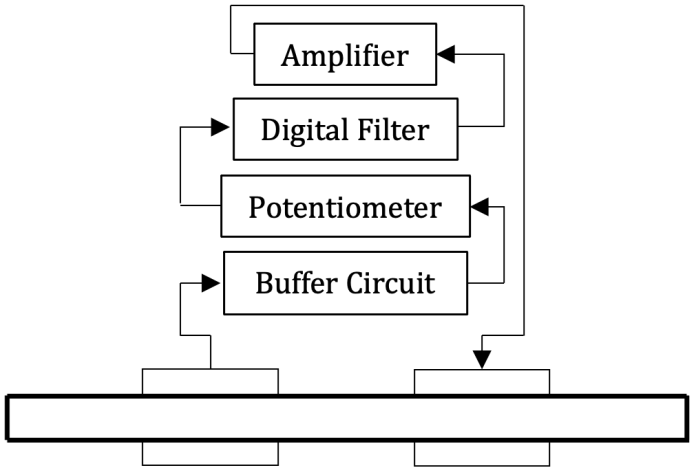

Figure 4.8: Controller diagram. The signal from the left set of patches was first sent through a buffer circuit designed for the high capacitance of the piezoelectric patches. The signal from the buffer circuit was sent through a potentiometer used to set a proportional gain. Next, the signal was passed through a digital low-pass filter implemented on a microcontroller which allowed us to filter out displacement behavior at frequencies beyond our band of interest. By modifying the corner frequency of this filter, we were able to produce the shifts in isolation peaks predicted by the model. Finally, the signal was sent through a high voltage amplifier before being sent to the right set of patches.

patches. A digital low-pass filter allowed us to filter out displacement behavior at frequencies beyond our band of interest. Finally, a potentiometer was included to fine tune desired proportional gains. A diagram of the controller is shown in Fig. 4.8. The potentiometer and amplifier were modeled as having flat frequency responses with proportional gains H_p and H_a, respectively. The buffer circuit and digital filter contributed both gain and phase shifts of the signal through the controller with transfer functions of $H_b(\omega)$ and $H_f(\omega)$, respectively, which are plotted in Fig. 4.9. The low-pass filter was of the elliptic type with a corner frequency f_{lp}. Altogether, the total controller gain, G, can be expressed as

$$G = H_b(\omega)H_pH_f(\omega)H_a. \tag{4.31}$$

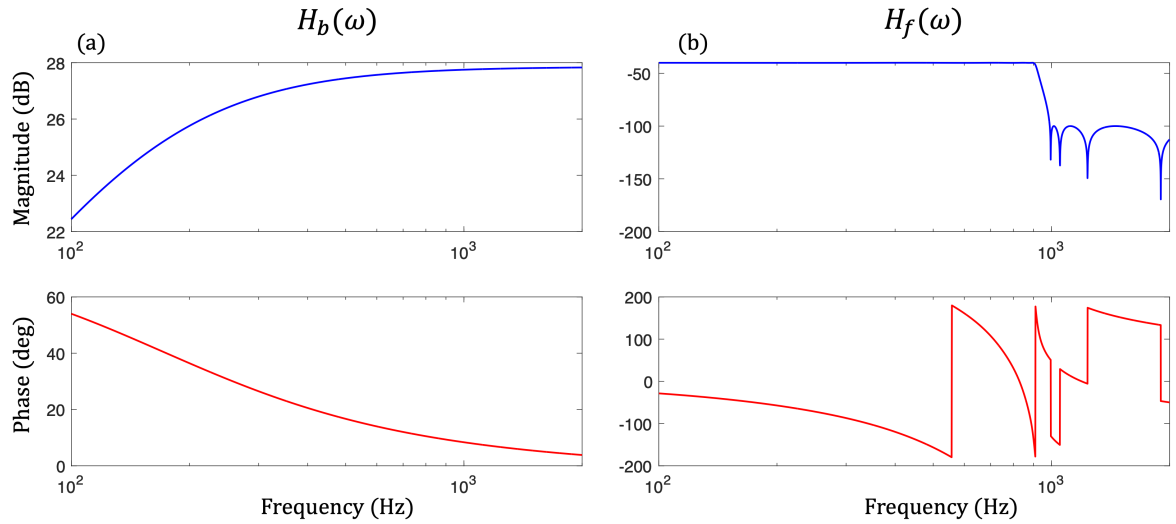

Figure 4.9: Frequency dependent components of controller transfer functions. (a) Magnitude and phase components of $H_b(\omega)$, the transfer function of the buffer circuit in the controller. (b) Magnitude and phase components of $H_f(\omega)$, the transfer function of the elliptic low-pass filter with corner frequency $f_{lp} = 900$ Hz used in the controller.

4.2.5 Model Predictions

We ran experiments using a beam with an elastic layer composed of 6061 aluminum and for piezoelectric layers composed of PZT-4. Nominal values for these materials are listed in Table 4.1. Using these nominal values in the model, the directional transmission coefficients $T_{(+)}$ and $T_{(-)}$ and the resulting isolation factors $\mathcal{I}$ were predicted for the controller parameter values shown in Table 4.2. Plotted in Fig. 4.10(a) are $T_{(+)}$ and $T_{(-)}$ for a low-pass filter with corner frequency, $f_{lp} = 900$ Hz. It can be seen in Fig. 4.10(a) that $T_{(+)}$ and $T_{(-)}$ differ significantly over a frequency range from 500 Hz to 1100 Hz, most apparent between 800 Hz and 900 Hz, where there is a large null in transmission from left to right. This null drives the large peak of nearly 35 dB in isolation as seen in the middle curve ($\mathcal{I}_2$) in Fig. 4.10(b). By adjusting f_{lp} higher or lower, the frequency where this large peak in isolation occurs can be increased or decreased, respectively, with slight adjustments in the total proportional gain imposed by the controller. These peak shifts are illustrated by the two additional curves in Fig. 4.10(b), where f_{lp} is either increased to 1000 Hz ($\mathcal{I}_3$) or decreased to 800 Hz ($\mathcal{I}_1$). These compelling model predictions prompted efforts to replicate model behavior experimentally,

	6061 Aluminum	PZT-4
ρ (kg m^{-3})	2700	7900
$1/E = s_{11}$ (Pa^{-1})	$1/68.9\times10^{-9}$	11.6×10^{-12}
b (mm)	20	20
h (mm)	3	0.7
l (mm)	–	26
d_{31} (CN^{-1})	–	-140×10^{-12}
ϵ_{33} (Fm^{-1})	–	12.4×10^{-9}

Table 4.1: Nominal values for the characteristics of 6061 aluminum and PZT-4 patches.

	$\mathcal{I}_1$	$\mathcal{I}_2$	$\mathcal{I}_3$
f_{lp} (Hz)	800	900	1000
H_p	0.422	0.399	0.380

Table 4.2: Controller values required to generate the large isolation peaks shown in Fig. 4.10.

efforts which are detailed in the following section.

4.3 Experimental Methods

4.3.1 Experimental Setup

The physical setup used to verify model predictions experimentally is shown in Fig. 4.11. As shown in Fig. 4.11(a), we used a piece of 6061 aluminum that was 3 mm thick, 20 mm wide, and approximately a meter long. Insulating layers of Kapton film were epoxied to the beam at locations where we desired patches. Strips of copper were then epoxied on top of the Kapton to provide a connection to the negative electrode of the piezoelectric patches. Then, using a conductive epoxy, we secured patches composed of PZT-4 that were 0.7 mm thick, 16 mm wide, and 26 mm long. Smaller strips of copper (not shown) were secured to

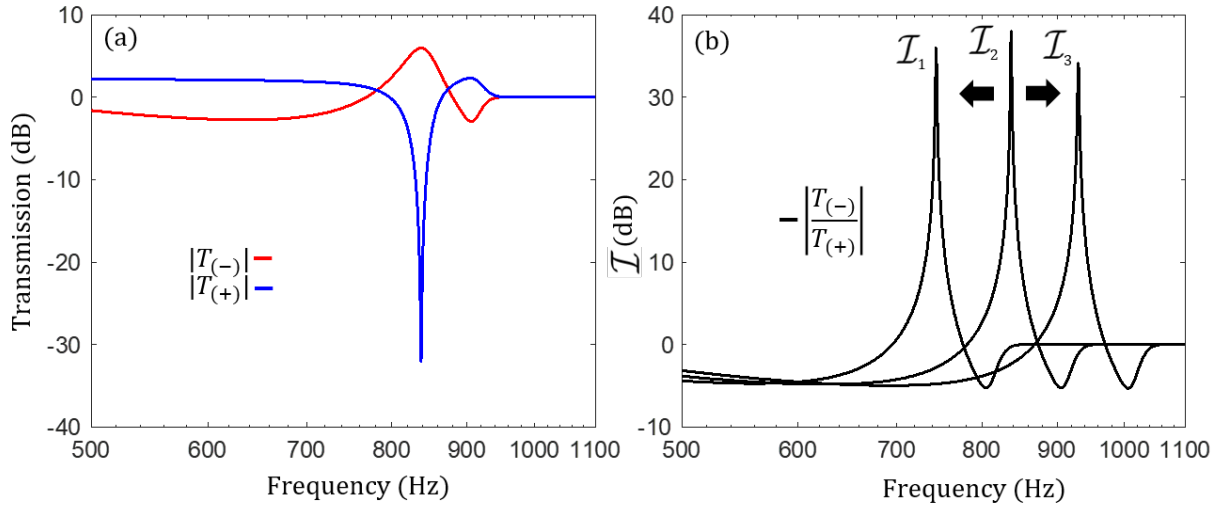

Figure 4.10: Transmission behavior of the nonlocal piezoelectric system. (a) Directional transmission coefficients across the system shown in Fig. 4.1 for a controller with low-pass filter corner frequency $f_{lp} = 900$ Hz (b) Isolation for low-pass filter corner frequencies 800 Hz ($\mathcal{I}_1$), 900 Hz ($\mathcal{I}_2$), and 1000 Hz ($\mathcal{I}_3$) demonstrate the tunable nature of the nonlocal elastodynamic system.

the upper surface of the patch to provide a connection to its positive electrode.

As shown in Fig. 4.11(b), the system was driven with a shaker at one end of the beam and secured with a clamp at the opposite end. Pieces of foam were inserted between the end connections and the beam to provide some dissipation to help stabilize the system (Fig. 4.11(c) and (d)). Beam displacements were computed using measurements from a laser doppler velocimeter (LDV) secured above the beam.

4.3.2 Physical Controller Components

The controller modeled in the previous section was implemented using the components shown in Fig. 4.12. The buffer circuit used to condition the signal from the left set of patches was implemented on the printed circuit board shown in Fig. 4.12 (a). The proportional gain H_p was controlled using the ten-turn potentiometer shown in Fig. 4.12 (b). The low-pass filtering was applied using a Teensy 3.6 Development Board, shown in Fig. 4.12 (c). The right set of patches were driven with a TREK Model 2220 high voltage amplifier imposing

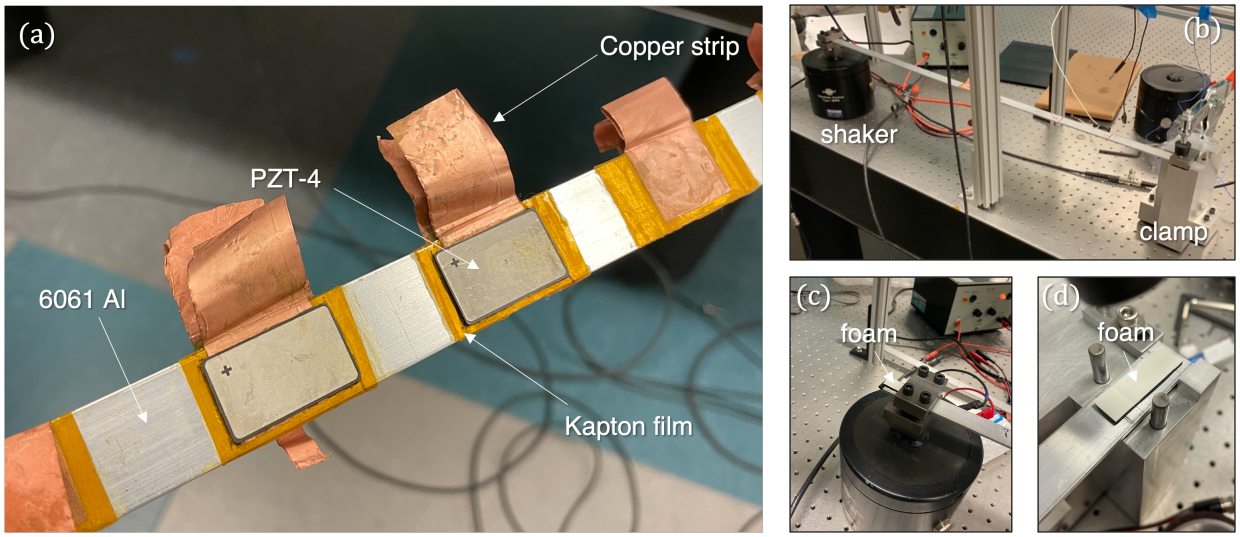

Figure 4.11: Experimental setup for the elastodynamic beam with piezoelectric patches. (a) Experiments were conducted using a piece of 6061 aluminum 3 mm thick, 20 mm wide, and approximately a meter long. Insulating layers of Kapton film were epoxied to the beam at locations where we desired patches. Strips of copper were then epoxied on top of the Kapton to provide a connection to the negative electrode of the piezoelectric patches. Then, using a conductive epoxy, we secured patches composed of PZT-4 that were 0.7 mm thick, 16 mm wide, and 26 mm long. Smaller strips of copper (not shown) were secured to the upper surface of the patch to provide a connection to its positive electrode. (b) The system was driven with a shaker at one end of the beam and secured with a clamp at the opposite end. (c) and (d) Pieces of foam were inserted between the end connections and the beam to provide some dissipation to help stabilize the system

the gain H_a, shown in Fig. 4.12 (d).

4.3.3 Model Parameter Adjustments

As experiments were conducted, it was found that to match experimental data to model predictions, some adjustments to model parameters were required. Parameter adjustments included the beam and patch geometries, measured with calipers, beam density and stiffness, determined using weight measurements and cantilevered resonant frequencies, respectively, of three additional plain aluminum beams, which provided reasonable ranges within which beam parameters could be adjusted, as well as the piezoelectric properties of the patches. Patches were characterized using capacitance measurements to adjust the permittivity, ε_{33},

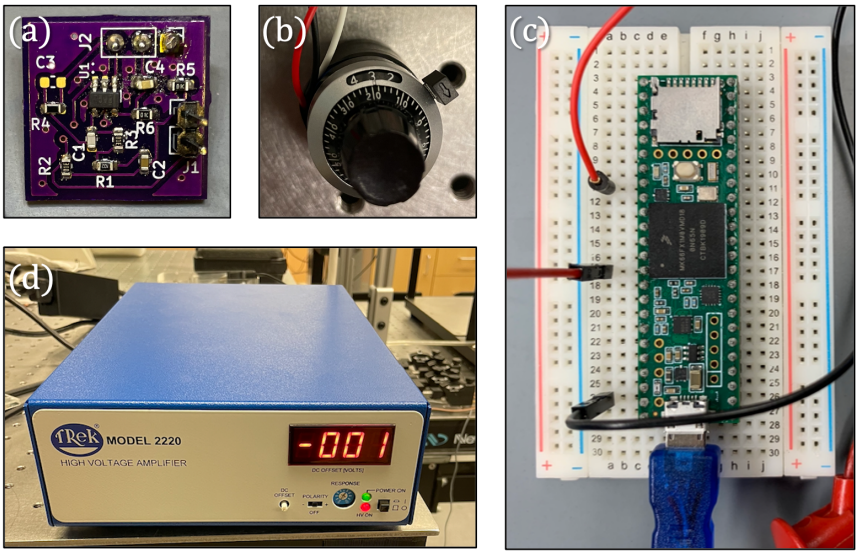

Figure 4.12: Experimental controller components. (a) Printed circuit board with the buffer circuit used to condition the signal from the sensing piezoelectric patches. (b) Ten-turn potentiometer with a dial indicator used to set H_p. (c) Microcontroller used to implement the digital low-pass filtering. (d) High voltage amplifier designed specifically for driving piezoelectric patches.

	6061 Aluminum	Patch 1	Patch 2	Patch 3	Patch 4
ρ (kg m^{-3})	2620	7900	7900	7900	7900
$1/E = s_{11}$ (Pa^{-1})	$1/65\times10^{-9}$	11.6×10^{-12}	11.6×10^{-12}	11.6×10^{-12}	11.6×10^{-12}
b (mm)	19.8	16.1	16.1	16.1	16.1
h (mm)	2.9	0.67	0.67	0.67	0.67
l (mm)	–	26.1	26.1	26.1	26.1
d_{31} (CN^{-1})	–	-140×10^{-12}	-140×10^{-12}	-140×10^{-12}	-140×10^{-12}
ϵ_{33} (Fm^{-1})	–	11.7×10^{-9}	12.0×10^{-9}	11.5×10^{-9}	11.4×10^{-9}

Table 4.3: Beam parameter values adjusted to improve model predictions of experimental data.

calculated by rearranging Eq. 4.15 to form

$$\varepsilon_{33} = \left(\frac{C_p h_p}{b l_p} - \frac{d_{31}^2}{s_{11}} \right). \tag{4.32}$$

The adjusted parameter values are shown in Table 4.3. It was also necessary to account

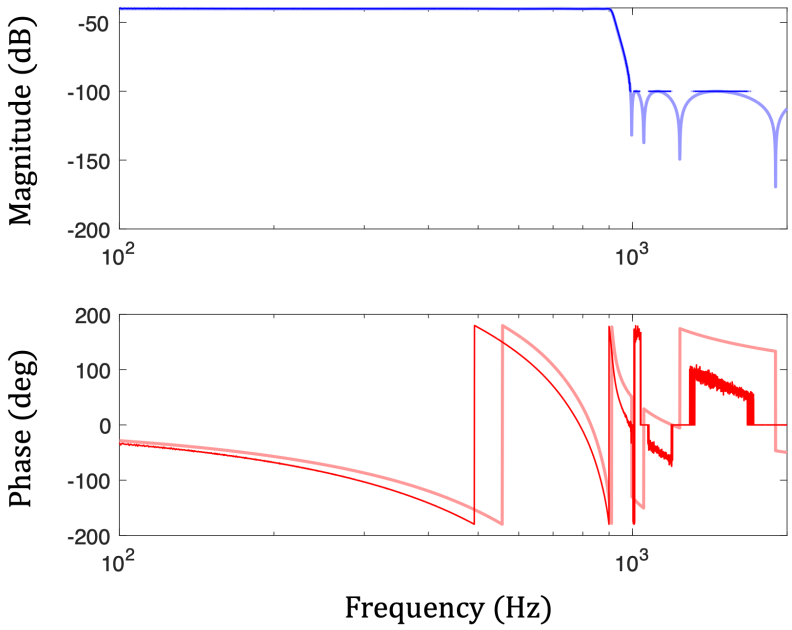

Figure 4.13: Comparison of the predicted and measured transfer functions of the digital low-pass filter with corner frequency $f_{lp} = 900$ Hz used in the controller. The predicted transfer function, depicted as lighter, thicker curves, matched the measured transfer function, depicted as darker, thinner curves, very well in terms of magnitude, but differed significantly in terms of phase.

for the difference in the predicted and measured transfer functions of the digital low-pass filters used in the controller, which is shown in Fig. 4.13 for a filter with corner frequency $f_{lp} = 900$ Hz. Comparing the predicted values (lighter, thicker curves) to the measured values (darker, thinner curves) indicated that while there was an excellent agreement in magnitude, the phase differed significantly. The source of this deviation remains unknown, but the difference was accounted for in the model by using the measured filter transfer functions. Using the measured transfer functions of the digital filters and the parameters in Table 4.3 in the model, the predicted values for H_p needed to be adjusted to maintain the high isolation peaks we desired. Those adjusted values are shown in Table 4.3.

	$\mathcal{I}_1$	$\mathcal{I}_2$	$\mathcal{I}_3$
f_{lp} (Hz)	800	900	1000
H_p	0.433	0.403	0.362

Table 4.4: Adjusted controller values required to generate the large isolation peaks shown in Fig. 4.10

4.3.4 Measurement Procedure

In collecting data during these experiments, we discovered that if we measured the displacement W_1 at a location x_m along the beam downstream from the right-most segment with patches (Fig. 4.14(a)), and, rather than moving the clamp and shaker to the opposite ends, we switched the leads on the patches and measured the displacement W_2 at the same location x_m (Fig. 4.14(b)), the ratio of the two displacements was equivalent to the ratio of transmission coefficients in either direction, i.e.,

$$\frac{W_2}{W_1} = \frac{T_{(-)}}{T_{(+)}}, \tag{4.33}$$

which again is what we have defined as the isolation level, $\mathcal{I}$. We found that for Eq. 4.33 to hold, a number of conditions must be met. Firstly, for the frequency band of interest, x_m should be at least 10 cm away from the patch segments and from the clamped boundary so that evanescent waves have decayed sufficiently to have a negligible contribution to the displacement fields. This requirement was determined using our analytical model as shown in Fig. 4.15. For radiation boundary conditions and incident wave forcing, transmission coefficients and isolation levels were compared with displacements and their ratios computed downstream from the patch segments at a distance of 1 cm (Fig. 4.15(a)and(b)) and 10 cm (Fig. 4.15(c)and(d)). It's clear from the plots that at 1 cm downstream from the patch segment, there is still a significant evanescent wave contribution to the displacement fields, yielding a poor match between transmissions and isolation levels with displacements and

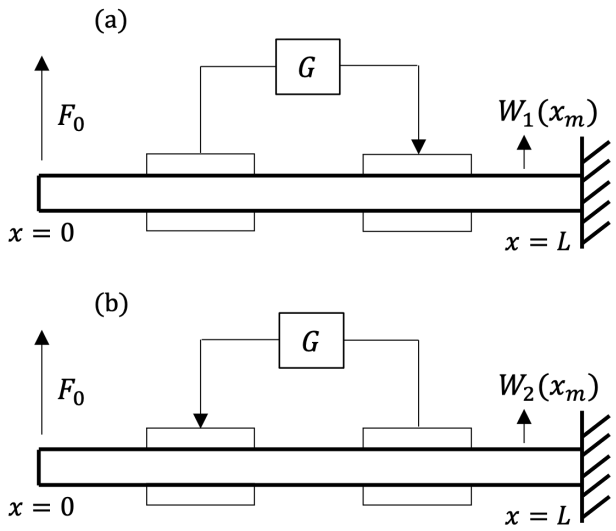

Figure 4.14: Experimental measurement diagram. (a) Displacement W_1 is measured at a location x_m downstream from the patch segment (b) Displacement W_2 is measured at a location x_m downstream from the patch segment with the controller direction switched.

their ratios. However, at 10 cm, evanescent waves have sufficiently decayed to have negligible influence on the displacement fields. Hence, experimentally, our patches were adhered to the midpoint of an aluminum beam nearly a meter long (see Fig. 4.11(b)), allowing us to collect LDV measurement that were at least 10 cm away from the patches and boundaries.

Another requirement for Eq. 4.33 to hold is that while forcing and boundary conditions need to be identical for both displacement measurements, it appears that the form those conditions take is inconsequential. This is demonstrated analytically in Fig. 4.16 for various combinations of the classic Bernouli-Euler beam forcing (prescribed force, prescribed moment, prescribed displacement, and prescribed slope) and boundary conditions (free, fixed, hinged, and sliding). It's clear from the plots that Eq. 4.33 holds for any combination of these forcing and boundary condition, and we hypothesized that Eq. 4.33 would also hold for the nonstandard boundary conditions present in our experimental setup, i.e., clamps with dissipating foam (Fig 4.11 (c) and (d)). It is also worth noting that the deviations of displacement ratios from the isolation levels, indicated by the arrows in Fig. 4.16, occur at frequencies where nulls exist in each displacement, and thus the displacement ratio at those frequencies is a ratio of two values very near zero. Hence, these deviations are numerical

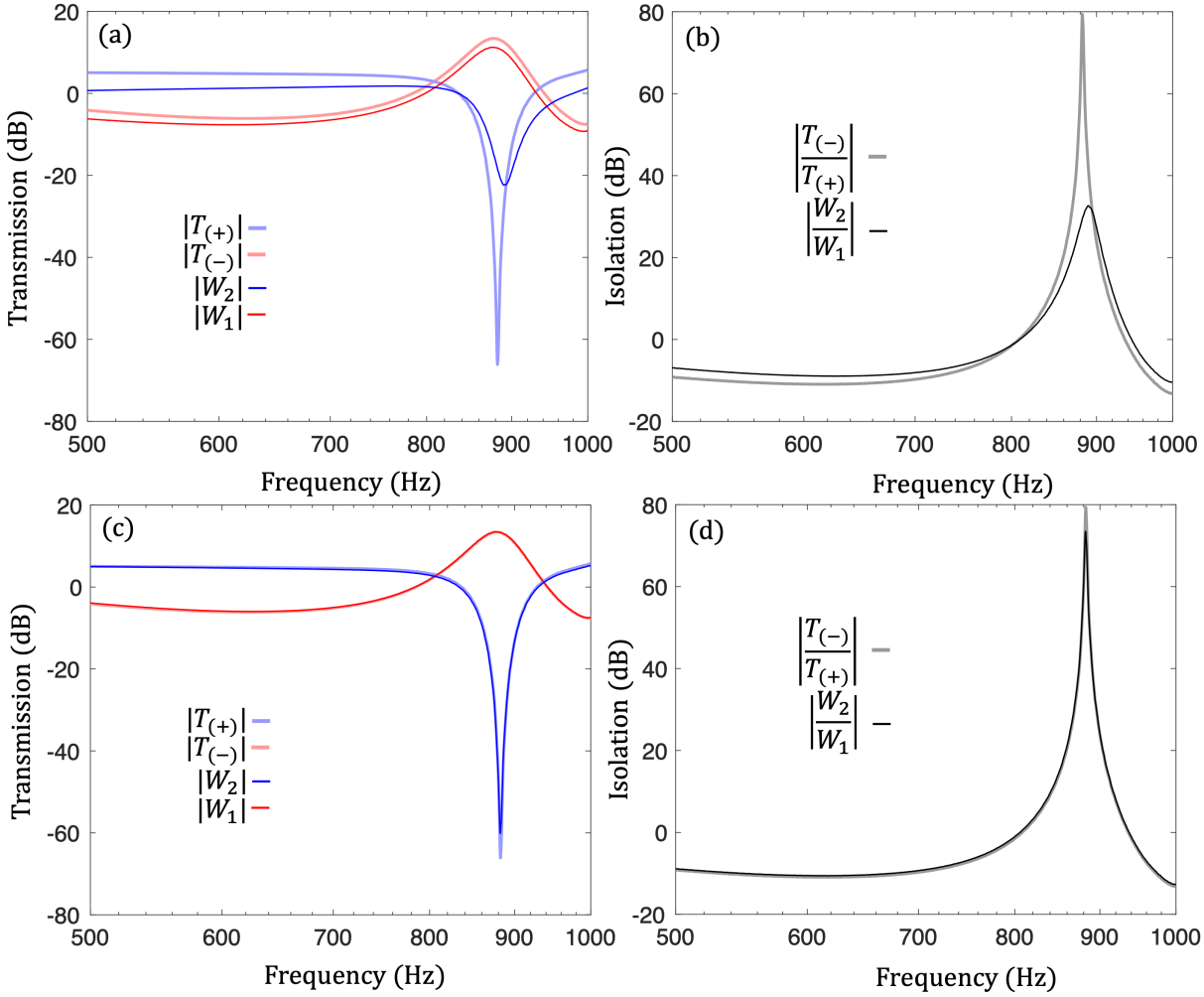

Figure 4.15: Analytical comparisons of displacements to transmission coefficients and displacement ratios to isolation levels for a beam with incident wave forcing and radiation boundary conditions. (a) Comparisons of displacements computed a distance of 1 cm downstream from the patch segment with transmission coefficients show a poor match due to evanescent wave contributions to the displacement fields. (b) Hence, there is also a poor match between displacement ratios and isolation levels. (c) Comparisons of displacements computed a distance of 10 cm downstream from the patch segment with transmission coefficients show an excellent match as evanescent wave contributions to the displacement fields are negligible at this distance. (d) Hence, there is also an excellent match between displacement ratios and isolation levels.

artifacts, and can be mitigated by avoiding displacement spectra that include nulls, whether computed analytically or measured experimentally.

Hence, though this measurement approach doesn't allow for comparing experimental

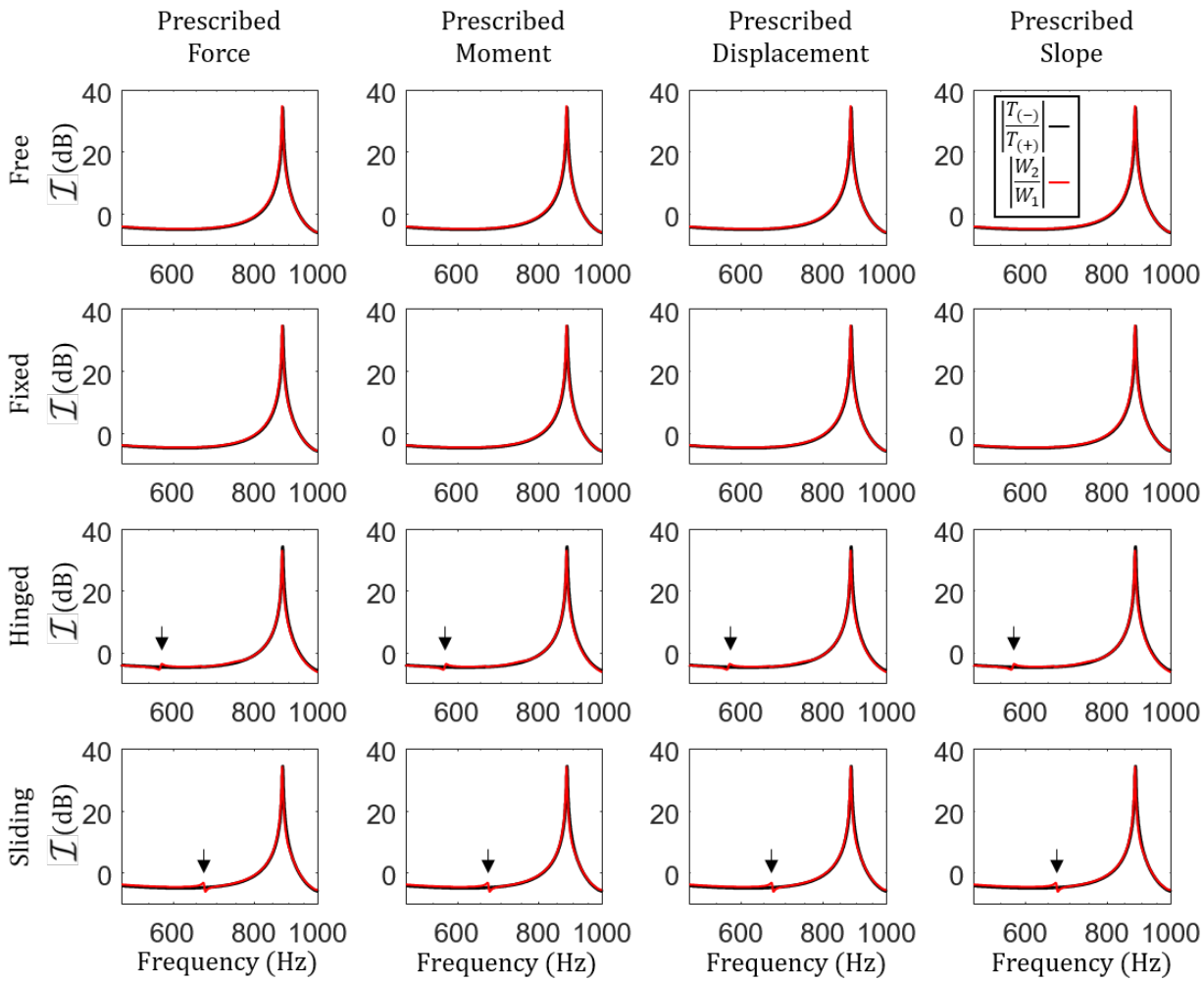

Figure 4.16: Isolation level comparisons with the ratio of displacements W_1 and W_2 for all combinations of the classic BE beam forcing and boundary conditions. The plots show an excellent agreement between isolation levels and displacement ratios for all combinations. The deviations indicated by the arrows represent numerical artifacts from the analytical model and can be mitigated by avoiding displacement spectra with nulls.

data directly with individual transmission coefficients, we do have the ability to efficiently compare data with isolation levels predicted by our model. Those results are presented in the following section.

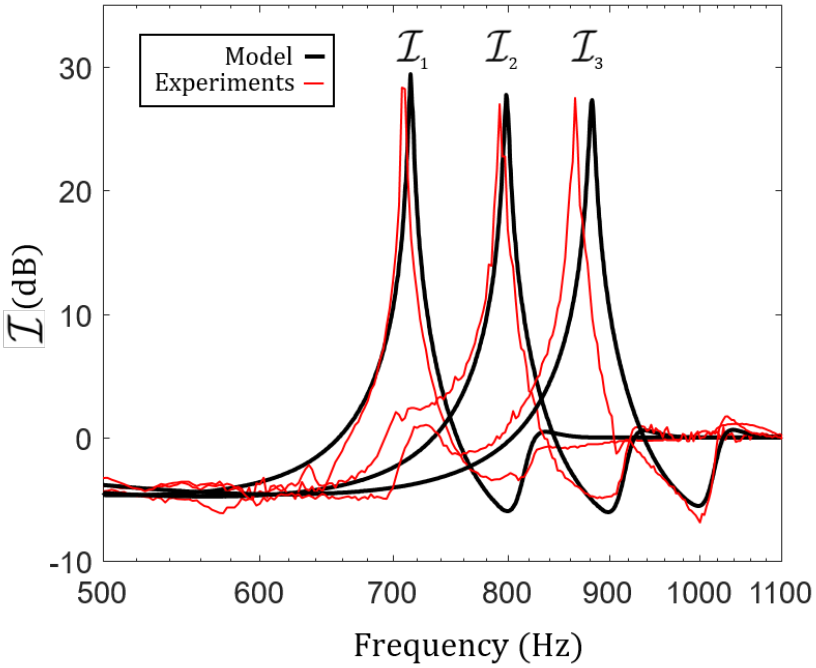

Figure 4.17: Experimental results show an excellent match between the isolation levels $\mathcal{I}_1$, $\mathcal{I}_2$, $\mathcal{I}_3$ determined experimentally (red) with model predictions (black). The results indicate that a highly nonreciprocal, subwavelength, and tunable dispersive system can be realized physically, and that its behavior can be accurately predicted with our analytical model.

4.4 Results

Experimental results are shown in Fig. 4.17, and reveal an excellent match with model predictions, which were determined using the adjusted model and controller parameters listed in Table 4.3 and Table 4.4. The isolation levels $\mathcal{I}_1$, $\mathcal{I}_2$, $\mathcal{I}_3$ determined experimentally are shown in green, blue, and red, respectively. In each case, experimental measurements closely followed its respective predicted isolation level, including peak levels and frequencies, as well as the overall curve shape in general. These results show that a real dispersive system that is highly nonreciprocal, subwavelength, and tunable can be realized.

There were slight differences in the predicted values of H_p compared with the values set on the real potentiometer, denoted as $\overline{H}_p$. Values for H_p and $\overline{H}_p$ are listed in Table 4.5. Despite their differences, predicted values were close enough to be of great practical use in conducting experiments. The peaks in isolation are highly sensitive to changes in H_p, with

	$\mathcal{I}_1$	$\mathcal{I}_2$	$\mathcal{I}_3$
f_{lp} (Hz)	800	900	1000
H_p	0.433	0.403	0.362
$\overline{H}_p$	0.422	0.320	0.319

Table 4.5: Experimentally determined potentiometer gains $\overline{H}_p$ compared with potentiometer gains predicted by the analytical model H_p

slight variations in H_p resulting in peaks substantially lower in magnitude. Because H_p and $\overline{H}_p$ were close in value, only slight adjustments to the potentiometer set to H_p were required to find $\overline{H}_p$. Due to system sensitivity, it's very unlikely $\overline{H}_p$ could have been found through trial and error alone.

4.5 Conclusion

We have successfully demonstrated experimentally a highly nonreciprocal, subwavelength, and tunable real dispersive system. We showed that the analytical model developed accurately predicted the behavior of the physical system. We discussed how the analytical model was of great practical use in selecting controller parameters required to generate large nonreciprocity. While the results are impressive on their own, because of the accuracy of the analytical model, future design of more elaborate systems can be studied in a computationally efficient way.

CHAPTER V

Conclusions, Contributions, and Future Work

5.1 Conclusions

In this work, we have demonstrated how the general concept of action at a distance affects the scattering behavior in wave-bearing systems, focusing primarily on its ability to break reciprocity. In Chapter II, We experimentally demonstrated large, tunable, broadband nonreciprocity for a subwavelength device using the NAM strategy. We showed that a simple one-dimensional coupled acoustic model can adequately predict the performance and stability of both full-wave simulations and experimental data.

In Chapter III, We demonstrated experimentally the advantages of multiple airborne NAM unit cells, which were predicted by both our ideal and enhanced models. Isolation levels for a two-cell system exceeded levels for each of its constituent unit cells individually, both in magnitude and bandwidth. We presented a guided user interface that allowed for real-time feedback of the effects of parameter changes on both performance and stability. We showed that while efforts to find optimal system parameters posed some limitations, optimization efforts were effective in determining appropriate unit cell spacing.

In Chapter IV, We demonstrated experimentally a highly nonreciprocal, subwavelength, and tunable real dispersive system. We showed that the analytical model developed accurately predicted the behavior of the physical system. We discussed how the analytical model was of great practical use in selecting controller parameters required to generate large non-

reciprocity, and will allow for the future design of more elaborate systems to be studied in a computationally efficient way.

5.2 Contributions

The following is a list of the contributions provided by this work to date. These contributions are the subjects of publications in New Journal of Physics [34] and Physical Review B [35], and conference presentations at the Acoustical Society of America [98, 99].

- We have developed a theoretical framework for generating linear broadband nonreciprocity by introducing nonlocal effects into an acoustic system. This framework provides practical insights in guiding the development of nonlocal systems as well as a physical insights regarding system behavior [34].

- We have demonstrated how this theoretical framework could be used in designing stable, nonlocal active metamaterials (NAM systems). These NAM systems provide a means of physically realizing the attractive features of nonlocal acoustic systems, namely their ability to significantly break reciprocity [34].

- We have designed and fabricated a constitutive unit cell of a NAM system, generating peaks in $\mathcal{I}$ of over 40 dB with $\mathcal{I}$ magnitudes above 10 dB across a third of an octave, demonstrating experimentally its ability to outperform current metamaterials which seek to break reciprocity. These results showed that the simplifying approximations in the models used for designing experimental systems were valid and suggest that current modelling strategies can be relied upon in future NAM system design work [35].

- We have shown experimentally how multiple NAM cells greatly enhances the performance of a single cell [98].

- We have demonstrated how spatial nonlocality can be used to break reciprocity in an elastodynamic system [99], with experimental values of $\mathcal{I}$ of nearly 30 dB generated

by a tunable, subwavelength system.

- Most generally, we have uncovered a vast design space in the field of metamaterials that represents a significant contribution to the metamaterial community.

5.3 Future Work

The work presented in Chapter III showed the significant advantages of adding just a second unit cell to the NAM system. One direction for future work is to consider systems with larger arrays of unit cells as shown in Fig. 5.1, for both acoustic (Fig. 5.1(a)) and elastic (Fig. 5.1(b)) systems. The outstanding matches between the system models and experimental data presented in this work suggest that larger arrays can be studied and designed analytically.

Another direction for future work is illustrated in Fig. 5.2. It occurred to us during this work that unit cells could be cascaded as shown in Fig. 5.2(a), and analyzed as an array of ideal NAM unit cells cascaded in the y-direction as shown in Fig. 5.2(b). Such a system

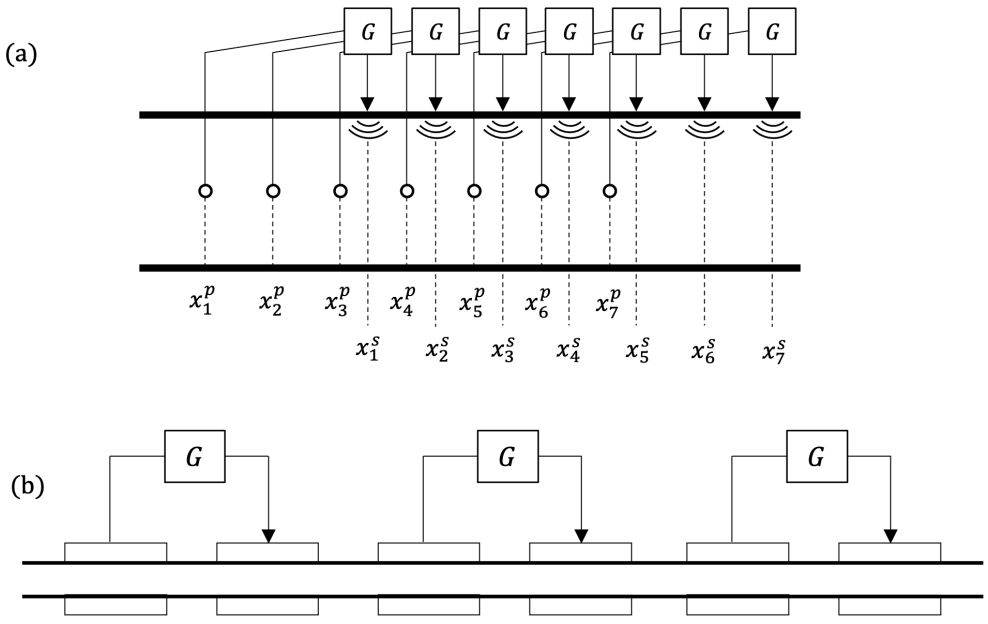

Figure 5.1: Schematics of larger arrays of both acoustic (a) and elastic (b) unit cells represent one promising direction for future work.

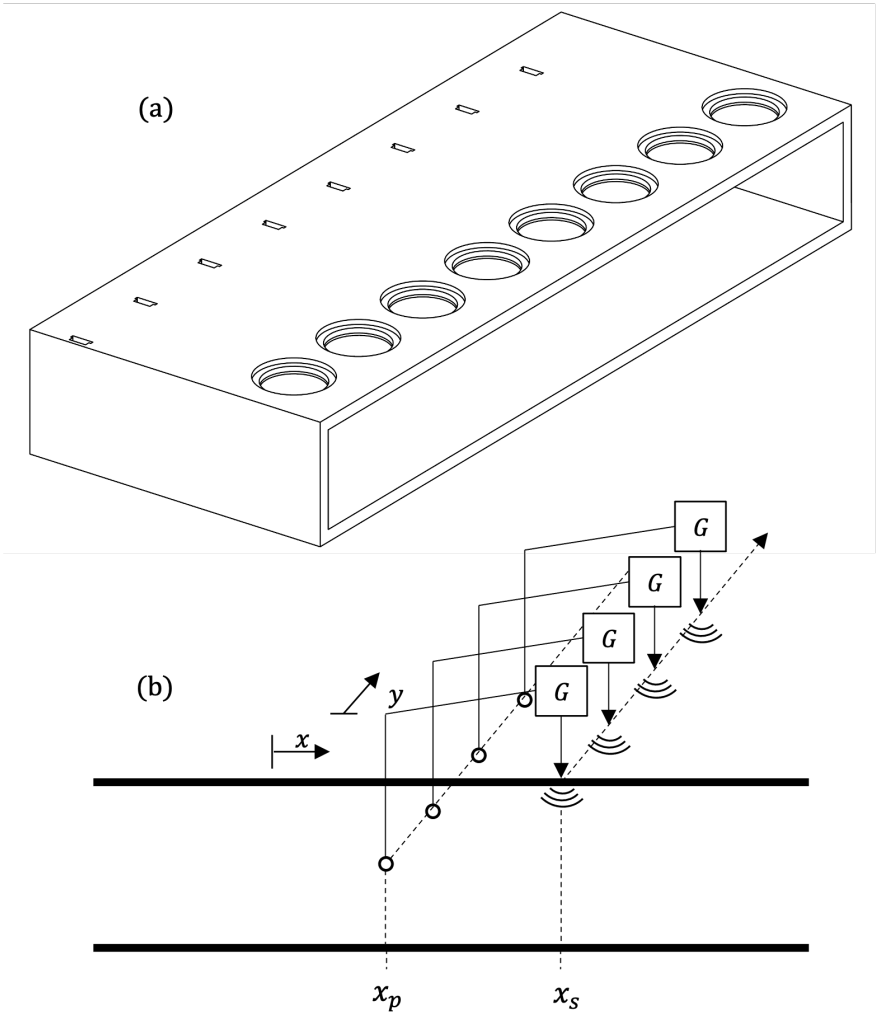

Figure 5.2: Two-dimensional NAM system. (a) NAM unit cells placed side-by-side could allow for the study of nonlocality in two-dimensional (2D) waveguides. (b) The system could be analyzed as an array of ideal NAM unit cells cascaded in the y-direction.

would provide a means for studying action at a distance in higher dimensions. Finally, all of this work was accomplished with a fairly simple controller consisting of a proportional gain and low-pass filtering, so considering more sophisticated controller designs would be another direction for future work.

APPENDIX

APPENDIX A

A.1 Scattering Matrix Derivation

The scattering matrix for the ideal NAM unit cell is determined from solutions to Eq. 2.1, which can be determined in the following manner. First, due to the delta function on the right-hand side of Eq. 2.1, for $x \neq x_s$, the system is governed by the homogeneous Helmholtz equation (i.e. Eq. 1.1), which has solutions of the form,

$$P(x) = Ae^{-jkx} + Be^{jkx}, \tag{A.1}$$

where A and B are the complex coefficients to be determined by boundary conditions of plane waves traveling in the positive-x and negative-x directions, respectively. Hence, solutions to Eq. 2.1 can be expressed in terms of pressure upstream from the source ($x < x_s$) and downstream from the source ($x > x_s$) as

$$P_u(x) = A_u e^{-jkx} + B_u e^{jkx}, \tag{A.2}$$

$$P_d(x) = A_d e^{-jkx} + B_d e^{jkx}. \tag{A.3}$$

These pressure fields are illustrated in Fig. A.1 To match the solutions P_u and P_d at $x = x_s$,

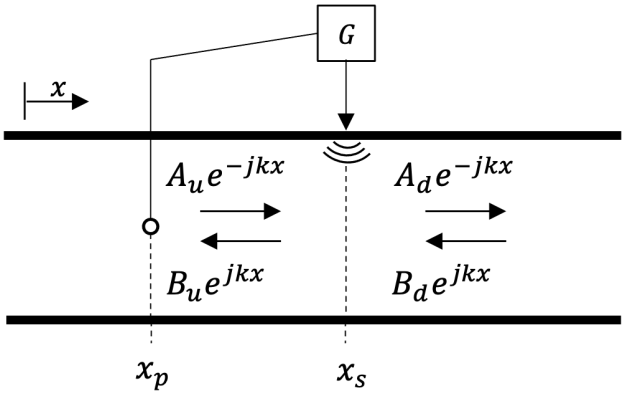

Figure A.1: One-dimensional acoustic domain showing pressure fields composed of positive-traveling and negative-traveling plane waves with complex magnitudes A_u,B_u,A_d, and B_d to be determined by applying boundary conditions and jump conditions.

two conditions are required. One condition is continuity of pressure, i.e., $P_u(x_s) = P_d(x_s)$. The second condition is established by integrating Eq. 2.1 across x_s,

$$\int_{x_s-\epsilon}^{x_s+\epsilon} \frac{d^2P(x)}{dx^2}dx + k^2 \int_{x_s-\epsilon}^{x_s+\epsilon} P(x)dx = GP(x_p) \int_{x_s-\epsilon}^{x_s+\epsilon} \delta(x - x_s)dx, \tag{A.4}$$

and taking the limit as $\epsilon \to 0$, giving

$$\frac{dP_d(x_s)}{dx} - \frac{dP_u(x_s)}{dx} = GP_u(x_p). \tag{A.5}$$

Finally, P_u and P_d can be solved for by applying Sommerfeld radiation conditions at the boundaries, which express pressure in the system as a transmitted and reflected wave in terms of some known incident wave in either direction.

A.2 Effective Material Properties

While the NAM unit cell response is most directly described by its scattering parameters, one can also describe the observed behavior in terms of effective material properties, as is often done in the analysis of metamaterials. Such analysis facilitates deeper understanding

and more effective design approaches when considering systems composed of arrays of unit cells. The NAM unit cell cannot be characterized by any of the traditional effective material properties evoked by metameterials, i.e., negative or near-zero mass density, negative or near-zero bulk modulus, or both negative or near-zero mass density and bulk modulus [27]. One must turn to more exotic material properties to fully characterize the NAM unit cell. Zhai, et al. in 2019 demonstrated that large nonreciprocity could be generated through manipulating properties of so called Willis materials [50]. In one-dimensional Willis materials, the pressure p and linear momentum μ can be expressed as

$$\begin{aligned} -p &= B\frac{du}{dx} + j\omega S u, \\ \mu &= D\frac{du}{dx} + j\omega\rho u, \end{aligned} \tag{A.6}$$

where u is the particle displacement, ρ and B are the material density and modulus, respectively, S and D are the Willis coupling terms, and ω is the forcing frequency [100]. Using the linearized Euler relationship between pressure and momentum, i.e., $-dp/dx = j\omega\mu$, Eq. A.6, can be used to derive the following wave equation:

$$\frac{d^2u}{dx^2} + j\omega\frac{S-D}{B}\frac{du}{dx} + \omega^2\rho u = 0. \tag{A.7}$$

Assuming particle displacement of the form $u = Ue^{-jkx}$, the right-going and left-going wavenumbers (k_+ and k_-, respectively) and impedances (Z_+ and Z_-, respectively) can be expressed as

$$\begin{aligned} k_{+/-} &= \omega\frac{S-D}{2B} \pm \omega\sqrt{\left(\frac{S-D}{2B}\right)^2 + \frac{\rho}{B}}, \\ Z_{+/-} &= -\frac{S+D}{2} \pm \sqrt{\left(\frac{S-D}{2}\right)^2 + \rho B}. \end{aligned} \tag{A.8}$$

Solving Eq. A.8 in terms of the Willis material parameters yields two sets of solutions, however when substituting the wavenumbers and impedances for those of air, only the following

solution recovers the correct density and bulk modulus of air:

$$\rho = -\frac{1}{\omega}\frac{k_- k_+ (Z_- - Z_+)}{k_- - k_+}, B = -\omega\frac{Z_+ - Z_-}{k_- - k_+}, S = \frac{k_+ Z_- - k_- Z_+}{k_- - k_+}, D = \frac{-k_- Z_- + k_+ Z_+}{k_- - k_+}. \tag{A.9}$$

Considering the general Willis material flanked on either side by domains of air, the scattering matrix in terms of the wavenumbers and impedances can be expressed as

$$\begin{aligned}
S_{11} &= \frac{(e^{jk_-\delta x} - e^{jk_+\delta x})(1 - z_-)(1 - z_+)}{e^{jk_-\delta x}(1 + z_-)(1 - z_+) - e^{jk_+\delta x}(1 - z_-)(1 + z_+)}, \\
S_{21} &= \frac{2(z_- - z_+)}{e^{jk_-\delta x}(1 + z_-)(1 - z_+) - e^{jk_+\delta x}(1 - z_-)(1 + z_+)}, \\
S_{12} &= \frac{2e^{j(k_- + k_+)\delta x}(z_- - z_+)}{e^{jk_-\delta x}(1 + z_-)(1 - z_+) - e^{jk_+\delta x}(1 - z_-)(1 + z_+)}, \\
S_{22} &= \frac{(e^{jk_-\delta x} - e^{jk_+\delta x})(1 + z_-)(1 + z_+)}{e^{jk_-\delta x}(1 + z_-)(1 - z_+) - e^{jk_+\delta x}(1 - z_-)(1 + z_+)},
\end{aligned} \tag{A.10}$$

where $z_{+/-} = Z_{+/-}/\rho_0 c_0$, and ρ_0 and c_0 are the density and speed of sound in air, respectively [101]. Inverting Eq. A.10, wavenumbers and relative impedances are found to be

$$k_{+/-} = \pm\left[\frac{2m\pi}{\delta x} - \frac{j}{\delta x}\ln\left(\frac{1 + S_{12}S_{21} - S_{11}S_{22} \pm \sqrt{-4S_{12}S_{21} + (1 + S_{12}S_{21} - S_{11}S_{22})^2}}{2S_{21}}\right)\right],$$

$$z_{+/-} = -\frac{S_{11} - S_{22} \pm \sqrt{-4S_{12}S_{21} + (1 + S_{12}S_{21} - S_{11}S_{22})^2}}{-1 + S_{11} + S_{12}S_{21} + S_{22} - S_{11}S_{22}}, \tag{A.11}$$

where $m \in \mathbb{Z}$. The appropriate signs and branch numbers were chosen such that at high frequencies, the wavenumbers and impedances were consistent with air since the NAM unit cell effects become negligible at high frequencies. Combining Eq. A.9 and Eq. A.11, the Willis parameters with respect to the properties of air (density ρ_0 and bulk modulus B_0) can be determined for the ideal NAM model. Plots of the dimensionless Willis parameters are shown in Fig. A.2. Although these effective material properties are plotted over the same range of frequencies over which transmission and reflection coefficients were plotted for the ideal NAM

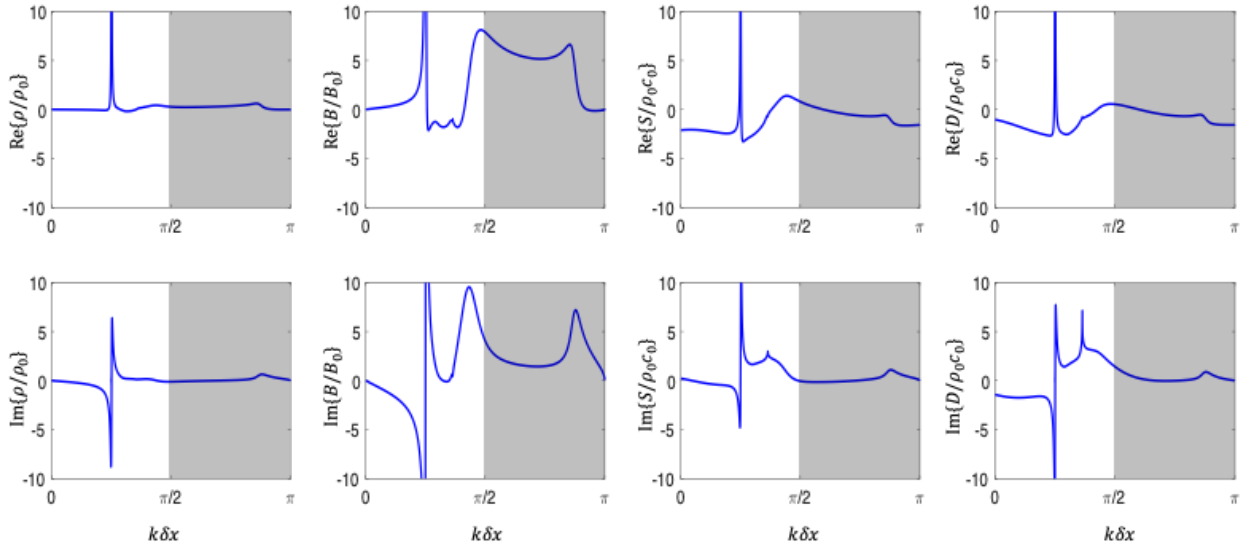

Figure A.2: Dimensionless effective Willis parameters. The real and imaginary parts of the effective Willis parameters for the NAM unit cell provide some insight into the unit cell behavior (e.g., nonreciprocity is illustrated by $S \neq D$). Plots for frequencies higher than $k\delta x = \pi/2$ are grayed out as such frequencies are generally considered too high to consider effective material properties.

unit cell in Chapter II, frequencies higher than $k\delta x = \pi/2$ would generally be deemed too high for effective material properties to be considered. At these frequencies, wavelengths of sound become comparable to the length of the NAM unit cell and violate the long wavelength assumption required for deriving effective material properties in metamaterials. There is no definitive limit for which wavelengths cease to be long enough with respect to unit cell lengths within the metamaterials community, however, unit cell lengths of $\lambda/10$ are usually considered acceptable while recent works have considered less conservative lengths of up to $\lambda/4$ [52]. Hence, in Fig. A.2, frequencies above $k\delta x = \pi/2$ (corresponding to a wavelength of $\lambda/4$) are grayed out. While these effective material properties lend some insight into the behavior of the NAM unit cell (e.g., nonreciprocity is illustrated by $S \neq D$), we determined the closed form expressions for the reflection and transmission coefficients more directly described the NAM unit cell behavior and were more illustrative of the impacts that design parameter changes had on that behavior. Therefore, effective material properties for the NAM unit cell were not considered in the main part of this dissertation, although they may

become beneficial in future design of arrays of unit cells in more complex NAM systems.

BIBLIOGRAPHY

BIBLIOGRAPHY

[1] P. A. Nelson and S. J. Elliott. *Active Control of Sound*. Academic Press, London, 1992.

[2] Z. Liu, X. Zhang, Y. Mao, Y. Y. Zhu, Z. Yang, C. T. Chan, and P. Sheng. Locally resonant sonic materials. *Science*, 289(5485):1734–1736, 2000.

[3] F. Morandi, M. Miniaci, A. Marzani, L. Barbaresi, and M. Garai. Standardised acoustic characterisation of sonic crystals noise barriers: Sound insulation and reflection properties. *Applied Acoustics*, 114:294–306, 2016.

[4] M. F. Limonov, M. V. Rybin, A. N. Poddubny, and Y. S. Kivshar. Fano resonances in photonics. *Nature Photonics*, 11(9):543–554, 2017.

[5] Z. Yang, J. Mei, M. Yang, N. H. Chan, and P. Sheng. Membrane-type acoustic metamaterial with negative dynamic mass. *Physical Review Letters*, 101(20):204301, 2008.

[6] S. Yao, X. Zhou, and G. Hu. Experimental study on negative effective mass in a 1d mass–spring system. *New Journal of Physics*, 10(4):043020, 2008.

[7] Y. Zhang, J. Wen, Y. Xiao, X. Wen, and J. Wang. Theoretical investigation of the sound attenuation of membrane-type acoustic metamaterials. *Physics Letters A*, 376(17):1489–1494, 2012.

[8] X. Jiang, B. Liang, R. Q. Li, X. Y. Zou, L. L. Yin, and J. C. Cheng. Ultra-broadband absorption by acoustic metamaterials. *Applied Physics Letters*, 105(24):243505, 2014.

[9] H. H. Huang and C. T. Sun. Wave attenuation mechanism in an acoustic metamaterial with negative effective mass density. *New Journal of Physics*, 11(1):013003, 2009.

[10] M. Badreddine Assouar, M. Senesi, M. Oudich, M. Ruzzene, and Z. Hou. Broadband plate-type acoustic metamaterial for low-frequency sound attenuation. *Applied Physics Letters*, 101(17):173505, 2012.

[11] C. J. Naify, C.-M. Chang, G. McKnight, and S. R. Nutt. Scaling of membrane-type locally resonant acoustic metamaterial arrays. *The Journal of the Acoustical Society of America*, 132(4):2784–2792, 2012.

[12] N. Fang, D. Xi, J. Xu, M. Ambati, W. Srituravanich, C. Sun, and X. Zhang. Ultrasonic metamaterials with negative modulus. *Nature Materials*, 5(6):452–456, 2006.

[13] V. M. García-Chocano, R. Graciá-Salgado, D. Torrent, F. Cervera, and J. Sánchez-Dehesa. Quasi-two-dimensional acoustic metamaterial with negative bulk modulus. *Physical Review B*, 85(18):184102, 2012.

[14] C. Ding, L. Hao, and X. Zhao. Two-dimensional acoustic metamaterial with negative modulus. *Journal of Applied Physics*, 108(7):074911, 2010.

[15] Z. G. Nicolaou and A. E. Motter. Mechanical metamaterials with negative compressibility transitions. *Nature Materials*, 11(7):608–613, 2012.

[16] Y. Ding, Z. Liu, C. Qiu, and J. Shi. Metamaterial with simultaneously negative bulk modulus and mass density. *Physical Review Letters*, 99(9):093904, 2007.

[17] Y. Cheng, J. Y. Xu, and X. J. Liu. One-dimensional structured ultrasonic metamaterials with simultaneously negative dynamic density and modulus. *Physical Review B*, 77(4):045134, 2008.

[18] L. Fok and X. Zhang. Negative acoustic index metamaterial. *Physical Review B*, 83(21):214304, 2011.

[19] F. Bongard, H. Lissek, and J. R. Mosig. Acoustic transmission line metamaterial with negative/zero/positive refractive index. *Physical Review B*, 82(9):094306, 2010.

[20] J. Christensen, Z. Liang, and M. Willatzen. Metadevices for the confinement of sound and broadband double-negativity behavior. *Physical Review B*, 88(10):100301, 2013.

[21] X. Zhou and G. Hu. Superlensing effect of an anisotropic metamaterial slab with near-zero dynamic mass. *Applied Physics Letters*, 98(26):263510, 2011.

[22] M. Yang, G. Ma, Z. Yang, and P. Sheng. Coupled membranes with doubly negative mass density and bulk modulus. *Physical Review Letters*, 110(13):134301, 2013.

[23] S. H. Lee, C. M. Park, Y. M. Seo, Z. G. Wang, and C. K. Kim. Composite acoustic medium with simultaneously negative density and modulus. *Physical Review Letters*, 104(5):054301, 2010.

[24] L. Zigoneanu, B. I. Popa, and S. A. Cummer. Three-dimensional broadband omnidirectional acoustic ground cloak. *Nature Materials*, 13(4):352–355, 2014.

[25] S. A. Cummer, J. Christensen, and A. Alù. Controlling sound with acoustic metamaterials. *Nature Reviews Materials*, 1(3):16001, 2016.

[26] B.-I. Popa and S. A. Cummer. Non-reciprocal and highly nonlinear active acoustic metamaterials. *Nature Communications*, 5(1):3398, 2014.

[27] F. Zangeneh-Nejad and R. Fleury. Active times for acoustic metamaterials. *Reviews in Physics*, 4:100031, 2019.

[28] M. Maldovan. Sound and heat revolutions in phononics. *Nature*, 503(7475):209–217, 2013.

[29] H. Nassar, B. Yousefzadeh, R. Fleury, M. Ruzzene, A. Alù, C. Daraio, A. N. Norris, G. Huang, and M. R. Haberman. Nonreciprocity in acoustic and elastic materials. *Nature Reviews Materials*, 5(9):667–685, 2020.

[30] C. Rasmussen, L. Quan, and A. Alù. Acoustic nonreciprocity. *Journal of Applied Physics*, 129(21):210903, 2021.

[31] L. Kinsler, A. Frey, A. Coppens, and J. Sanders. *Fundamentals of acoustics*. Wiley, New York, 4th ed. edition, 2000.

[32] Y. C. Fung. *Foundations of Solid Mechanics*. Prentice-Hall, New Jersey, 1966.

[33] L. M. Lyamshev. A question in connection with the principle of reciprocity in acoustics. *Soviet Physics Doklady*, 4:406, 1959.

[34] A. Sasmal, N. Geib, B.-I. Popa, and K. Grosh. Broadband nonreciprocal linear acoustics through a non-local active metamaterial. *New Journal of Physics*, 22(6):063010, 2020.

[35] N. Geib, A. Sasmal, Z. Wang, Y. Zhai, B. I. Popa, and K. Grosh. Tunable nonlocal purely active nonreciprocal acoustic media. *Physical Review B*, 103(16):165427, 2021.

[36] N. Boechler, G. Theocharis, and C. Daraio. Bifurcation-based acoustic switching and rectification. *Nature Materials*, 10(9):665–668, 2011.

[37] F. Zangeneh-Nejad and R. Fleury. Doppler-Based Acoustic Gyrator. *Applied Sciences*, 8(7):1083, 2018.

[38] R. Fleury, A. B. Khanikaev, and A. Alù. Floquet topological insulators for sound. *Nature Communications*, 7:11744, 2016.

[39] Y. G. Peng, Y. X. Shen, D. G. Zhao, and X. F. Zhu. Low-loss and broadband anomalous Floquet topological insulator for airborne sound. *Applied Physics Letters*, 110(17):173505, 2017.

[40] A. B. Khanikaev, R. Fleury, S. H. Mousavi, and A. Alù. Topologically robust sound propagation in an angular-momentum-biased graphene-like resonator lattice. *Nature Communications*, 6(1):8260, 2015.

[41] R. Fleury, D. L. Sounas, C. F. Sieck, M. R. Haberman, and A. Alù. Sound isolation and giant linear nonreciprocity in a compact acoustic circulator. *Science*, 343(6170):516–519, 2014.

[42] A. Rogov and E. Narimanov. Space-Time Metamaterials. *ACS Photonics*, 5(7):2868–2877, 2018.

[43] Y. Chen, X. Li, H. Nassar, G. Hu, and G. Huang. A programmable metasurface for real time control of broadband elastic rays. *Smart Materials and Structures*, 27(11):115011, 2018.

[44] B. M. Goldsberry, S. P. Wallen, and M. R. Haberman. Nonreciprocal vibrations of finite elastic structures with spatiotemporally modulated material properties. *Physical Review B*, 102(1):014312, 2020.

[45] B. M. Goldsberry, S. P. Wallen, and M. R. Haberman. Nonreciprocity and Mode Conversion in a Spatiotemporally Modulated Elastic Wave Circulator. *Physical Review Applied*, 17(3):034050, 2022.

[46] D. N. Vitek, E. Block, Y. Bellouard, D. E. Adams, S. Backus, D. Kleinfeld, C. Durfee, and J. A. Squier. Spatio-temporally focused femtosecond laser pulses for anisotropic writing in optically transparent materials. *Optics InfoBase Conference Papers*, 18(24):24673–24678, 2011.

[47] D. Torrent, O. Poncelet, and J. C. Batsale. Nonreciprocal Thermal Material by Spatiotemporal Modulation. *Physical Review Letters*, 120(12):125501, 2018.

[48] A. E. Cardin, S. R. Silva, S. R. Vardeny, W. J. Padilla, A. Saxena, A. J. Taylor, W. J. Kort-Kamp, H. T. Chen, D. A. Dalvit, and A. K. Azad. Surface-wave-assisted nonreciprocity in spatio-temporally modulated metasurfaces. *Nature Communications*, 11(1):1–9, 2020.

[49] L. Xu, J. Huang, and X. Ouyang. Tunable thermal wave nonreciprocity by spatiotemporal modulation. *Physical Review E*, 103(3):32128, 2021.

[50] Y. Zhai, H. S. Kwon, and B. I. Popa. Active Willis metamaterials for ultracompact nonreciprocal linear acoustic devices. *Physical Review B*, 99(22):220301, 2019.

[51] H. Nassar, X. C. Xu, A. N. Norris, and G. L. Huang. Modulated phononic crystals: Non-reciprocal wave propagation and Willis materials. *Journal of the Mechanics and Physics of Solids*, 101:10–29, 2017.

[52] L. Quan, D. L. Sounas, and A. Alù. Nonreciprocal Willis Coupling in Zero-Index Moving Media. *Physical Review Letters*, 123(6):64301, 2019.

[53] Y. Chen, X. Li, G. Hu, M. R. Haberman, and G. Huang. An active mechanical Willis meta-layer with asymmetric polarizabilities. *Nature Communications*, 11(1):1–8, 2020.

[54] M. Collet, P. David, and M. Berthillier. Active acoustical impedance using distributed electrodynamical transducers. *The Journal of the Acoustical Society of America*, 125(2):882–894, 2009.

[55] A. Sommerfeld. Die Greensche Funktion der Schwingungslgleichung. *Jahresbericht der Deutschen Mathematiker-Vereinigung*, 21:309–352, 1912.

[56] A. Somerfeld. *Partial differential equations in physics*. Academic Press, New York, 1949.

[57] M. Åbom. Measurement of the scattering-matrix of acoustical two-ports. *Mechanical Systems and Signal Processing*, 5(2):89–104, 1991.

[58] S. Gnanarajan. Solutions for Series of Exponential Equations in Terms of Lambert-W Function and Fundamental Constants. *Journal of Applied Mathematics and Physics*, 6(4):725–736, 2018.

[59] M. Hassani. Approximation of the Lambert W Function. *Mathematics Subject Classification*, pages 1–2, 1991.

[60] E. W. Weisstein. Lambert W-function. *https://mathworld.wolfram.com/LambertW-Function.html*.

[61] O. Olivieri, J. S. Bolton, and T. Yoo. Measurement of transmission loss of materials using a standing wave tube. *Institute of Noise Control Engineering of the USA - 35th International Congress and Exposition on Noise Control Engineering, INTER-NOISE 2006*, 8:5285–5292, 2006.

[62] Z. Tao and A. F. Seybert. A review of current techniques for measuring muffler transmission loss. *SAE Technical Papers*, 2003.

[63] A. R. Barnard and M. D. Rao. Measurement of Sound Transmission Loss Using a Modified Four Microphone Impedance Tube. *Nosise-Con*, 2004.

[64] R. H. Small. Closed-Box Loudspeaker Systems-Part 1: Analysis. *Journal of The Audio Engineering Society*, 20:798–808, 1972.

[65] N. Thiele. Loudspeakers in Vented Boxes: Part 1. *Journal of The Audio Engineering Society*, 19:382–392, 1971.

[66] S. Laurin and K. Reichard. Determining Manufacture Variation in Loudspeakers Through Measurement of Thiele/Small Parameters. *Journal of the Audio Engineering Society*, 2008.

[67] A. Falaize and T. Hélie. Passive modelling of the electrodynamic loudspeaker: From the Thiele-Small model to nonlinear port-Hamiltonian systems. *Acta Acustica*, 4(1), 2020.

[68] L. L. Beranek. *Acoustics*. McGraw-Hill, New York, 1954.

[69] A. Bergamini, T. Delpero, L. D. Simoni, L. D. Lillo, M. Ruzzene, and P. Ermanni. Phononic crystal with adaptive connectivity. *Advanced Materials*, 26(9):1343–1347, 2014.

[70] L. Airoldi and M. Ruzzene. Design of tunable acoustic metamaterials through periodic arrays of resonant shunted piezos. *New Journal of Physics*, 13(11):113010, 2011.

[71] B. S. Beck, K. A. Cunefare, M. Ruzzene, and M. Collet. Experimental analysis of a cantilever beam with a shunted piezoelectric periodic array. *Journal of Intelligent Material Systems and Structures*, 22(11):1177–1187, 2011.

[72] F. Dell'Isola, C. Maurini, and M. Porfiri. Passive damping of beam vibrations through distributed electric networks and piezoelectric transducers: Prototype design and experimental validation. *Smart Materials and Structures*, 13(2):299–308, 2004.

[73] T.-H. Cheng and I.-K. Oh. A current-flowing electromagnetic shunt damper for multi-mode vibration control of cantilever beams. *Smart Materials and Structures*, 18(9):095036, 2009.

[74] Y. Y. Chen, R. Zhu, M. V. Barnhart, and G. L. Huang. Enhanced flexural wave sensing by adaptive gradient-index metamaterials. *Scientific Reports*, 6(1):35048, 2016.

[75] M. I. Friswell and S. Adhikari. Structural health monitoring using shaped sensors. *Collection of Technical Papers - AIAA/ASME/ASCE/AHS/ASC Structures, Structural Dynamics and Materials Conference*, 2009.

[76] C. Zhang, H. Zhang, T. Yu, and X. Wang. Piezoelectric-based smart sensing system for I-beam structural health monitoring. *Health Monitoring of Structural and Biological Systems 2016*, 9805:603–611, 2016.

[77] Y. Amini, P. Fatehi, M. Heshmati, and H. Parandvar. Time domain and frequency domain analysis of functionally graded piezoelectric harvesters subjected to random vibration: Finite element modeling. *Composite Structures*, 136:384–393, 2016.

[78] Y. Amini, M. Heshmati, P. Fatehi, and S. E. Habibi. Piezoelectric energy harvesting from vibrations of a beam subjected to multi-moving loads. *Applied Mathematical Modelling*, 49:1–16, 2017.

[79] Z. Zhang, H. Xiang, and Z. Shi. Mechanism exploration of piezoelectric energy harvesting from vibration in beams subjected to moving harmonic loads. *Composite Structures*, 179:368–376, 2017.

[80] C. Sugino, M. Ruzzene, and A. Erturk. Nonreciprocal piezoelectric metamaterial framework and circuit strategies. *Physical Review B*, 102(1):014304, 2020.

[81] A. Mehrvarz, M. J. Khodaei, A. Darabi, A. Zareei, and N. Jalili. Experimental Demonstration of Broadband Reconfigurable Mechanical Nonreciprocity. pages 1–6, 2021.

[82] Y. Zheng, Z. Wu, X. Zhang, and K. W. Wang. A piezo-metastructure with bistable circuit shunts for adaptive nonreciprocal wave transmission. *Smart Materials and Structures*, 28(4):045005, 4 2019.

[83] M. Krommer. On the correction of the Bernoulli-Euler beam theory for smart piezoelectric beams. *Smart Materials and Structures*, 10(4):668–680, 2001.

[84] R. Littrell and K. Grosh. Modeling and characterization of cantilever-based MEMS piezoelectric sensors and actuators. *Journal of Microelectromechanical Systems*, 21(2):406–413, 2012.

[85] J. A. Gripp and D. A. Rade. Vibration and noise control using shunted piezoelectric transducers: A review. *Mechanical Systems and Signal Processing*, 112:359–383, 2018.

[86] Q. Wu and G. Huang. A micropolar metabeam with nonlocal feedback control circuits. *ASME International Mechanical Engineering Congress and Exposition, Proceedings (IMECE)*, 1:1–8, 2021.

[87] X. Li, Y. Chen, R. Zhu, and G. Huang. An active meta-layer for optimal flexural wave absorption and cloaking. *Mechanical Systems and Signal Processing*, 149:107324, 2021.

[88] U. Aridogan and I. Basdogan. A review of active vibration and noise suppression of plate-like structures with piezoelectric transducers. *Journal of Intelligent Material Systems and Structures*, 26(12):1455–1476, 2015.

[89] D. L. Logan. *A First Course in the Finite Element Method*. Nelson, Toronto, fourth edition, 2007.

[90] J. M. Davies. An Exact Finite Element for Beam on Elastic Foundation Problems. *Journal of Structural Mechanics*, 14(4):489–499, 1986.

[91] J. R. Banerjee and F. W. Williams. Exact Bernoulli–Euler dynamic stiffness matrix for a range of tapered beams. *International Journal for Numerical Methods in Engineering*, 21(12):2289–2302, 1985.

[92] M. Eisenberger. Exact static and dynamic stiffness matrices for general variable cross section members. *AIAA Journal*, 28(6):1105–1109, 1990.

[93] M. J. Bianco, C. Könke, A. Habtemariam, and V. Zabel. Exact finite element formulation in generalized beam theory. *International Journal of Advanced Structural Engineering*, 10(3):295–323, 2018.

[94] D. Givoli and J. B. Keller. Non-reflecting boundary conditions for elastic waves. *Wave Motion*, 12(3):261–279, 1990.

[95] R. Clayton and B. Engquist. Absorbing boundary conditions for acoustic and elastic wave equations. *Bulletin of the Seismological Society of America*, 67(6):1529–1540, 1977.

[96] B. Engquist and A. Majda. Radiation boundary conditions for acoustic and elastic wave calculations. *Communications on Pure and Applied Mathematics*, 32(3):313–357, 1979.

[97] J. B. Keller and D. Givoli. Exact non-reflecting boundary conditions. *Journal of Computational Physics*, 82(1):172–192, 1989.

[98] N. Geib, B.-I. Popa, and K. Grosh. Unit cell interactions of non-local active acoustic media. *The Journal of the Acoustical Society of America*, 149(4):A80–A80, 4 2021.

[99] N. Geib, B.-I. Popa, and K. Grosh. Breaking reciprocity through nonlocal coupling in elastodynamic systems. *The Journal of the Acoustical Society of America*, 150(4):A108–A108, 10 2021.

[100] M. B. Muhlestein, C. F. Sieck, P. S. Wilson, and M. R. Haberman. Experimental evidence of Willis coupling in a one-dimensional effective material element. *Nature Communications*, 8(1):15625, 2017.

[101] B.-I. Popa and S. A. Cummer. Nonreciprocal active metamaterials. *Phys. Rev. B*, 85(20):205101, 2012.